SCUOLA DI DOTTORATO
UNIVERSITÀ DEGLI STUDI DI MILANO-BICOCCA

Department of Physics “Giuseppe Occhialini”

PhD program in Physics and Astronomy Cycle XXXIV

Curriculum in Plasma Physics and Biophysics

Development and applications of super-resolution photo-thermal imaging

Surname: Marini Name: Mario

Registration number: 783136

Tutor: Prof. Maddalena Collini

Coordinator: Prof. Marta Calvi

ACADEMIC YEAR 2020/2021

Contents

List of symbols and abbreviations

x, y, z	spatial coordinates
t	time
θ	polar angle
ϕ	azimuthal angle
T	temperature
T_0, T_m	background temperature
$\overline{\Delta T}_{max}$	maximum pixel-averaged temperature increment
ΔT_{min}	minumum temperature threshold
k	thermal conductivity
D	thermal diffusivity
c	specific heat capacity
C	concentration
h_{cond}	conductive heat transfer coefficient
h_{conv}, h	convective heat transfer coefficient
h_{rad}	radiative heat transfer coefficient
Bi	Biot number
ε	emissivity
W	radiant emittance
W_λ	spectral radiant emittance
λ	wavelength
σ	Stefan-Boltzmann's constant
k_B	Boltzmann's constant
c_l	speed of light
$\hbar$	reduced Planck's constant
$\mathbb{G}$	Green's function
Φ	thermal camera output signal
C_{tc}	thermal camera calibration constant
l	thermal camera pixel size
d	sample-thermal camera distance
δx	scanning pixel size
Δ_x, Δ_y	scan parameters
N_x, N_y	image format
x_c, y_c	localized center coordinates
ℓ	biopsy thickness
L	sample thickness
A	sample area
τ	exponential rise time
τ_d	exponential decay time
τ_{on}	laser activation time
τ_{off}	laser deactivation time

ω	laser beam waist
n	index of refraction
$\mathcal{T}$	transmittance
$\mathcal{R}$	reflectance
$\mathcal{A}$	absorbance
E	molar extinction coefficient
α	linear absorption coefficient
σ	uncertainty
ζ	Gaussian standard deviation
E	electric field
I	intensity
P	laser power
P_{abs}	absorbed power
$\dot{Q}$	transferred power
S	volumetric source term
a	lens radius
f	lens focal length
M	magnification
Δ	spatial resolution
Δ_{eff}	effective spatial resolution
J_1	Bessel function of the first kind
NA	Numerical Aperture
CSF	Coherent Spread Function
PSF	Point Spread Function
Ar	Argon
He-Ne	Helium-Neon
VIS	Visible spectrum
NIR	Near InfraRed spectrum
PALM	Photo-Activated Localization Microscopy
STORM	STochastic Optical Reconstruction Microscopy
ROI	Region Of Interest
NP	NanoParticle
PBNP	Prussian Blue NanoParticle
H&E	Hematoxylin and Eosin staining
IMDM	Iscove's Modified Dulbecco's Medium
FBS	Fetal Bovine Serum
OCT	Optimal Cutting Temperature
SEM	Scanning Electron Microscopy
TEM	Transmission Electron Microscopy
AFM	Atomic Force Microscopy
FEM	Finite Element Method

Introduction and scope

The quantitative experimental investigation of heat transfer processes is a valuable tool for the characterization of the structural properties and the functional state of both biological tissues and inorganic materials. In the clinical and preclinical setting, for example, the modified blood perfusion and metabolic activity associated to the presence of inflammations, cancer masses or physiological dysfunctions can be accessed via the resulting alterations in the tissues thermo-physical properties. Externally induced temperature variations can provide direct access to the spatial distribution of bio-markers in biopsy specimens, and allow developing quantitative screening tools for the (early stage) detection of pathologies: prominent applications include the melanin-based identification of macular retinal degeneration and the discrimination of malignant pigmented skin lesions in the context of melanoma screening and diagnosis. Temperature-based imaging, when brought to the spatial resolution of (a few) cells and implemented in an intrinsically label-free approach, would be therefore a valuable diagnostic tool in medicine. In electronics and materials engineering, the high-sensitivity characterization of the sample thermal behavior is equally relevant: it allows monitoring the dissipation efficiency and ensuring the long-lasting performance of electronic devices and micro-electro-mechanical systems subject to intensive heat load, it enables the optimization of energy harvesting devices, and it lies at the basis of quality controls on the thermo-conduction properties of newly synthesized materials. All these applications demand for the development of quantitative methods capable of combining morphological temperature-based imaging of the sample structure with spatial resolution well below the millimeter range with the highly sensitive and non-invasive measurement of the sample thermal properties over extended ($< \mathrm{mm}^2$-cm^2) fields of view.

Straightforward access to temperature values, coupled to non-invasive imaging over wide (mesoscale) areas, is a key advantage of infrared thermography. As

I review in chapter 1, conventional non-contact thermal imaging provides temperature spatial maps based on the intensity of the thermal radiation emitted by the sample. Whether applied to the detection of externally induced temperature variations (active thermography) or employed to quantify spontaneous temperature changes associated to intrinsic heat generation in the sample (passive thermography), infrared imaging relies on microbolometer-based thermal cameras, that convert the intensity of the detected far infrared ($\sim$ 7-15 μm) radiation into absolute temperature measurements under the assumptions of grey body radiance and known sample emissivity (Stefan-Boltzmann's law). Recent advances in the design of increasingly sensitive image sensors have turned infrared thermal imaging into a mature technology, capable of space-resolved temperature mapping down to 20-40 mK sensitivity. Still, two major drawbacks limit the technique in fully capturing the sample functional state and/or compositional heterogeneity: (i) temperature images are hardly converted into quantitative maps of any thermal property, and (ii) diffraction at the low (typically < 0.05) numerical aperture of the collecting Germanium or Zinc-Selenide optics theoretically limits the spatial resolution at $\sim$ 0.1-0.5 mm. The nominal limit is further worsened to an effective value of $\sim$ 1 mm by both the typically extended camera pixel size on the sample plane and the thermal wave diffusion in the sample, so that a high-resolution thermal characterization of biological tissues and synthetic samples is typically prevented.

In this work, I tackle both the major limitations affecting state-of-the-art active infrared thermal imaging by the conceptualization and the experimental validation of a novel super-resolution image acquisition and processing method. I demonstrate photo-activated thermal imaging at the tunable $\sim$ 10-40 μm resolution required by forefront medical, electronic and nano-technological applications on variably extended (sub-millimeter to centimeter-sized) fields of view, and I combine sub-diffraction imaging with the non-invasive quantitative measurement of absolute thermal conductivity values over the three-order-of-magnitude 0.1-100 W/mK thermal conductivity range.

The fundamental principles of super-resolved thermography are presented in chapter 2. Similarly to what is performed in fluorescence-based PALM (Photo-Activated Localization Microscopy) and STORM (STochastic Optical Reconstruction Microscopy), the strategy combines the photo-thermal effect induced by the sample absorption of modulated raster-scanned laser light with the automated a-posteriori localization of the resulting laser-induced temperature variations. By the non-

linear surface Gaussian fit of the isolated temperature peaks appearing in the thermal-camera frames, light-absorbing and heat-releasing centers get localized and rendered in the final super-resolution image. Provided the excitation laser spot size can be tuned at will down to a $\sim \mu m$ diffraction-limited size, the achievable resolution is ultimately determined by the $\sim$ 10-50 μm peak localization accuracy achieved with typical detected temperature increments of few degrees.

The newly developed super-resolution image acquisition approach is validated by proof-of-principle experiments on both synthetic and biological samples. At first, I demonstrate the achievement of $< 60\,\mu m$ spatial resolution on custom ink samples. Results confirm 6- and 20-time resolution enhancements relatively to the diffraction-limited prediction and to the effective resolution of the thermal camera in conventional operation. Then, I exemplify the application of super-resolved thermography to biological samples with sparse distributions of visible-light absorbers. Upon experimental characterization of the sample emissivity and of its spatial heterogeneity, I reconstruct super-resolved maps of the spatial distribution of 30-nm Prussian-Blue nanocubes in explanted murine skin biopsies. This is a necessary step for the development of photo-thermal therapy protocols to be subsequently applied in-vivo to the tissue in pathological conditions.

Applied in chapter 2 to the detection of exogenous nanostructures, super-resolved thermography finds its best application in the identification and spatial mapping of endogenous photo-thermal chromophores in label-free configuration. This is exemplified in chapter 3, which is entirely devoted to the exploitation of photo-activated thermal imaging for the characterization of the distribution and the quantification of the absolute molar concentration of melanin pigments in murine melanoma biopsies.

The investigation is motivated by the prominent role played by melanin pigments in regulating the development and evolution of melanoma. Although the detailed structure of the final products of melanin biosynthesis is still unknown, it is widely recognized that the production of melanin can be highly deregulated in melanomas and may favor tumor progression due to immunosuppressive, genotoxic and mutagenic properties. While providing the necessary protection against ultraviolet radiation and reactive oxygen species in the skin, melanin has been pointed out to adversely affect the clinical outcome of metastatic melanomas and retains a still controversial role in regulating melanoma invasiveness. It also acts as a marker for melanocyte differentiation, serving as potential diagnostic tool. The melanin concentration and spatial distribution are therefore informative biomarkers,

and their inclusion in synoptic reports by pathologists is expected to complement and strengthen the robustness of standard histopathological analyses based on the visual inspection of excised biopsies.

Label-free photo-activated thermal imaging of melanin pigments is demonstrated here on B16 murine melanoma biopsies. At first, I demonstrate the specificity of infrared thermography in the identification of melanin by complementary hematoxylin-and-eosin staining of the same biopsies, and I confirm accurate morphological imaging of the tissue sections by the comparison of super-resolved thermal maps with the corresponding conventional transmitted-light images of the same samples. Then, based on finite-element numerical simulations and on the solution of the three-dimensional heat equation in the presence of laser light illumination, I provide a straightforward protocol to convert super-resolved thermal images into quantitative maps of the absolute melanin molar concentration. By enabling the label-free quantification of the melanin content with $5 \times 10^{-4}\,\mathrm{M}$ concentration sensitivity, the proposed approach complements the information extracted from excised melanoma biopsies by more traditional histopathological analyses based on immunohistochemistry and hematoxylin-and-eosin stainings.

Experiments on murine melanoma biopsies demonstrate that the amplitudes of laser-primed temperature variations provide the localization and the simultaneous quantification of the photo-thermal components in the sample. Along with the amplitude of individual temperature increments, the raw image sequence acquired in a super-resolution photo-thermal imaging experiment provides access to the full temperature rise-and-decay temporal kinetics associated to each laser illumination event. In chapter 4, I demonstrate that the temperature temporal evolution is directly related to, and allow quantifying, the sample thermal properties.

Starting from Fourier's heat transfer law, I surmise that the product of the amplitude and characteristic rise time of the temperature variations primed by focused laser light obeys a universal inverse proportionality on the sample thermal conductivity, irrespective of density and specific heat capacity. I demonstrate such a dependence over the three conductivity decades $0.1\text{-}100\,W/mK$ on both thermally thick and thermally thin homogeneous solid slabs by finite-element numerical simulations, and exploit to devise a data-analysis protocol aimed at the measurement of absolute thermal conductivity values.

The measurement procedure is initially validated by single-point experiments on reference samples. Then, by building on the super-resolution photo-thermal image acquisition scheme reported in chapter 2, I exemplify the feasibility of space-

resolved thermal-conductivity measurements to assess the conservation state of cultural heritage artifacts consisting in historical eighteenth-century tin organ pipe fragments. The product of the thermal conductivity times the sample thickness, imaged at $40\,\mu m$ sub-diffraction resolution over mm^2-sized areas, is pointed out as a relevant parameter for the non-destructive characterization of the sample conservation state, thereby suggesting the potential application of super-resolved thermography in the context of cultural heritage conservation and non-destructive material testing. Overall, by coupling temperature maps with the extraction of thermal properties at high spatial resolution, the proposed approach significantly expands the capability of state-of-the-art infrared imaging technology in fully capturing the structural heterogeneity and the functional state of the imaged materials.

Chapter 1

Theoretical background

The ability to control and quantitatively monitor heat transfer processes is beneficial in a wide variety of research areas, ranging from bio- and nano- technology to electronics and materials engineering. The assessment of thermo-physical properties enables the characterization of newly synthesized materials, it allows targeting photo-thermal biomedical applications of nanostructured devices, and allows preventing the fault of electronic and mechanical components subject to intensive heat load. Methods aimed at the direct non-invasive and high-resolution experimental measurement of the sample temperature and thermal properties are therefore constantly being developed.

In this chapter, I focus on infrared thermal imaging, which provides temperature spatial maps based on the intensity of the thermal grey-body radiation emitted by the sample. I review the fundamentals and key advantages of the technique, and discuss the spatial resolution of thermography setups. Particular interest is devoted to the extensive theoretical treatment of the three-dimensional heat equation: by modeling the temperature signal sensed by pixelated thermal cameras in the presence of laser light illumination, in this chapter I provide the theoretical basis for the super-resolution (temperature and thermal conductivity) imaging approach developed and validated throughout this thesis.

1.1 Fundamentals of infrared thermal imaging

Infrared (IR) thermal imaging, also called *thermography*, provides temperature images based on the intensity of the thermal radiation emitted by the sample

and detected by a microbolometer-based thermal camera [1]. It is a recent and rapidly evolving field of science. Although the laws of thermal radiation have been described in 1900 by Max Planck [2], the first portable infrared-detecting cameras only became available in the 1970s. Then over the last two decades, with enormous progresses in the microsystem technologies, we have achieved the possibility of producing affordable and reliable micro-bolometer infrared cameras to be widely used [1]. Nowadays, thermal cameras of this kind have been employed worldwide for the large scale monitoring of the human body temperature in the context of the Covid-19 pandemic (which is still ongoing during the preparation of this manuscript), demonstrating the high potential of thermography not only in basic research or industrial applications but even in the everyday life.

The main reason that makes thermography attractive for both amateurs and insiders can be found in the wide variety of phenomena that it allows to monitor. In fact, several physical processes from the bulk to the microscale (e.g friction, Joule effect, light matter interaction, ...) may lead to a thermal dissipation, and this can be successfully tracked and investigated by infrared thermal imaging. Before discussing the working principles of thermography, I recall here the basic mechanisms involved in heat propagation, the so called *heat transfer modes*.

1.1.1 Heat transfer modes

Temperature variations in any situation result from energy flow into a system or energy flow from a system to the surroundings: in the first case we obtain a net heating, whereas in the second case we obtain a net cooling of the object. In physics, three heat exchange mechanisms are usually distinguished: conduction, convection and radiation.

Conduction

Conduction refers to the heat flow in a solid or fluid which is at rest. From a microscopic point of view, the temperature of a body is a consequence of the average movement of the molecules (in the case of fluids) or the crystal lattice vibration (in the case of solids): high temperatures correspond to high average kinetic energy and vice versa. When two objects with different temperatures are in contact, the collisions at the molecular scale lead to an energy transport from high kinetic energies to low kinetic energies [1]. This process can be described by the

Fourier's law:

$$\dot{Q}_{cond} = -kA\nabla T \tag{1.1.1}$$

where $\dot{Q}$ is the transferred power (measured in W), ∇T is the temperature gradient, A is the surface area of the object, and k is its thermal conductivity (in $W/(mK)$). This apparently simple equation represents a fundamental result in physics, which can be generalized and applied to a wide variety of natural processes. We can indeed find expressions similar to the Fourier's law for other transport phenomena, namely Fick's law for mass transport, Ohm's law for charge transport, and Darcy's law for hydraulic flow.

Conduction of heat within an object, e.g. a one dimensional wall, is usually assumed to be proportional to the temperature difference $T_1 - T_2$ on the two sides of the object [3]. This can be easily shown by approximating equation 1.1.1 in the discrete case

$$\dot{Q}_{cond} = kA\frac{dT}{ds} \approx \frac{k}{L}A(T_1 - T_2) = h_{cond}A(T_1 - T_2) \tag{1.1.2}$$

The heat transfer coefficient for conduction, introduced here, is defined as $h_{cond} = k/L$, where L is the characteristic object size.

Convection

Convection refers to the heat flow between a solid and a fluid in motion and can be explained considering the combination of two different microscopic mechanisms. First, part of the convective heat transfer is due to the conduction of heat between the object surface and the fluid layer very close to the surface, that is, it is due to molecular motion and collision processes. This is actually a conduction process at the boundary between two materials with different thermal properties. Second, convective contribution is due to the bulk motion of the fluid, which sweeps away the heat that was transferred via conduction from the surface. For this reason the convective heat flux from the surface of an object with temperature T immersed in a fluid of temperature T_0 is usually assumed to follow a law similar to the one of conduction:

$$\dot{Q}_{conv} = h_{conv}A(T - T_0) \tag{1.1.3}$$

Typical values for free convective heat transfer coefficient h_{conv} of gases above solids range between 2 and 25 $W/(m^2K)$ [4, 5]. The values for forced convections can be higher by an order of magnitude [1].

It should now be clear that a body immersed in a surrounding medium experiences two kinds of thermal resistances: the first is due to conduction within the object, and the second one is due to convection at the interface. The balance between these two contributions determines the behaviour of the temperature inside the body. In order to quantify this concept, we can define the Biot number, which is a dimensionless quantity describing the ratio of the outer heat flow from the surface to the surrounding and the inner heat flow within the object:

$$Bi = \frac{h_{conv}}{h_{cond}} = \frac{h_{conv} \cdot L}{k} \tag{1.1.4}$$

For $Bi \ll 1$, the internal heat flow is much larger than the heat loss from the surface. Therefore, there will be a homogeneous temperature distribution within the solid. In this case the body is considered as *thermally thin*. Practically, for $Bi < 0.1$ the approximation of spatially uniform temperature distribution holds, with a maximum 2% deviation from the exact temperature values [6]. On the contrary, when $Bi \gg 1$ convection dominates over conduction: this results in a strong spatial variation of the internal temperature within the object, which behaves as a *thermally thick* sample.

Radiation

The emission of thermal radiation is at the basis of infrared thermography, and for this reason it will be extensively discussed in section 1.1.2. The radiating heat flux for an object of temperature T surrounded by a background with temperature T_0 is expressed by the product of the emissivity ε (material property) and the blackbody radiation due to the object temperature:

$$\dot{Q}_{rad} = \varepsilon \sigma A (T^4 - T_0^4) \tag{1.1.5}$$

where $\sigma = 5.67 \times 10^{-8}\, W/(m^2K^4)$ is known as Stefan-Boltzmann's constant. This expression exhibits a nonlinear dependence on temperature. However - since any quantitative analysis concerning heat transfer is much easier for linear temperature differences - it is customary to approximate the radiative contribution with a linear equation based on

$$\begin{aligned}(T^4 - T_0^4) &= [(T + T_0)(T^2 + T_0^2)](T - T_0) \\ &\approx 4T_0^3(T - T_0)\end{aligned} \tag{1.1.6}$$

This makes sense for small temperature differences ($T \approx T_0$). By defining $h_{rad} = \varepsilon\sigma 4T_0^3$ we can rewrite eq. 1.1.5 as:

$$\dot{Q}_{rad} = h_{rad} A (T - T_0) \tag{1.1.7}$$

Based on eqs. 1.1.2, 1.1.3 and 1.1.7, we can therefore conclude that the three processes of conduction, convection and radiation can be described with the same approximated law ($\dot{Q} = hA\Delta T$), known as Newton's law of cooling, which states that *the rate of heat loss of a body is directly proportional to the difference in the temperatures of the body and of its surroundings*. This statement is equivalent to claiming that *the temperature difference of a cooling body with respect to the surroundings decreases exponentially with time* [3]. In fact, for a heated object with initial temperature T_{in} in the small Biot number regime ($Bi \ll 1$, i.e. an average temperature is sufficient to characterize the cooling of the object), energy conservation states that

$$mc\frac{dT}{dt} = -\dot{Q}_{cond} - \dot{Q}_{conv} - \dot{Q}_{rad} \approx -h_{tot} A (T - T_0) \tag{1.1.8}$$

where $h_{tot} = h_{cond} + h_{conv} + h_{rad}$. The solution for $t_0 = 0$ is

$$T(t) = T_0 + (T_{in} - T_0) \cdot e^{-t/\tau} \tag{1.1.9}$$

with time constant $\tau = \dfrac{mc}{h_{tot} A}$.

1.1.2 Black body radiation

The theoretical approach at the basis of thermal imaging has been historically developed for a perfect emitter of thermal radiation. This is called *black body* and consists in an ideal surface that absorbs every incident radiation at any wavelength. As perfect absorbers and emitters, black bodies serve as reference standards in laboratories for the calibration of thermographic instruments. Experimentally, they can be realized as isothermal cavities heated to a uniform temperature.

Precise spectral measurements of thermal radiation of cavities existed by the end of the nineteenth century. However, it was not before 1900 that measured spectra could be satisfactorily explained based on the work of Max Planck. In modern language, the spectral radiant emittance of a black body at given temperature T in the wavelength interval $(\lambda, \lambda + d\lambda)$ can be written as:

$$W_{\lambda b} d\lambda = \frac{4\pi^2 \hbar c_l^2}{\lambda^5} \frac{1}{e^{2\pi\hbar c_l / \lambda k_B T} - 1} d\lambda \tag{1.1.10}$$

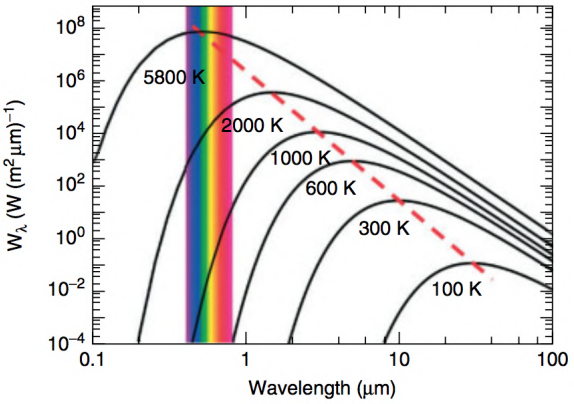

Figure 1.1: Black body spectral radiant emittance according to Planck's law, plotted for various absolute temperatures. The red dashed line gives the position of the maxima according to Wien's law. [1]

where c_l is the speed of light, $\hbar$ is the reduced Planck's constant and k_B is Boltzmann's constant.

Figure 1.1 depicts a series of black body spectra for various temperatures. It can be noticed that, for any fixed wavelength, radiance increases with temperature. Moreover, the spectral region of emission depends on temperature: low temperatures lead to longer wavelengths, high temperatures lead to shorter wavelength emission.

By differentiating Planck's formula with respect to λ, and finding the maximum, we obtain *Wien's displacement law*:

$$\lambda_{max} = \frac{2897.8\,\mu m \cdot K}{T} \tag{1.1.11}$$

depicted in figure 1.1 as a red dashed line.

By integrating Planck's formula we obtain the total radiant emittance (W) of a black body:

$$W_b(T) = \int_0^\infty W_{\lambda b}\,d\lambda = \sigma T^4 \tag{1.1.12}$$

where $\sigma = 5.67 \times 10^{-12}\,W m^{-2} K^{-4}$ is the aforementioned Stefan-Boltzmann's constant. Stefan-Boltzmann's law (eq. 1.1.12) has a great importance in thermal

imaging, since it states the possibility to trace back to a quantitative measurement of the temperature starting from the detected radiant emittance.

Black bodies are idealizations and no real object can emit this maximum thermal radiation at a given temperature. The real emission of thermal radiation from any object can however be easily computed by introducing an object-dependent quantity referred to as emissivity ε [7, 8]. The object emissivity is the ratio of the amount of radiation actually emitted from the surface to that emitted by a black body at the same temperature and wavelength:

$$\varepsilon_\lambda = \frac{W_\lambda}{W_{\lambda b}} \tag{1.1.13}$$

Three processes can occur preventing a real object from acting like a black body: a fraction of the incident radiation $\mathcal{A}$ may be absorbed, a fraction $\mathcal{R}$ may be reflected, and a fraction $\mathcal{T}$ may be transmitted. The sum of these three factors must always add up to the whole at any wavelength, so we have the relation

$$\mathcal{A}_\lambda + \mathcal{R}_\lambda + \mathcal{T}_\lambda = 1 \tag{1.1.14}$$

For opaque materials $\mathcal{T}_\lambda = 0$ and the relation simplifies to:

$$\mathcal{A}_\lambda + \mathcal{R}_\lambda = 1 \tag{1.1.15}$$

According to Kirchhoff's law, for any material the spectral emissivity and spectral absorptance of a body are equal at any specified temperature and wavelength:

$$\varepsilon_\lambda = \mathcal{A}_\lambda \tag{1.1.16}$$

From this we obtain, for an opaque material,

$$\varepsilon_\lambda + \mathcal{R}_\lambda = 1 \tag{1.1.17}$$

This last equations state that every gray-body emitter has an emissivity less than 1 and the black-body condition represents the maximum achievable. For a gray-body radiator, Stefan-Boltzmann's formula becomes:

$$W = \varepsilon \sigma T^4 \tag{1.1.18}$$

Equation 1.1.18 is at the basis of temperature measurements by infrared thermography setups.

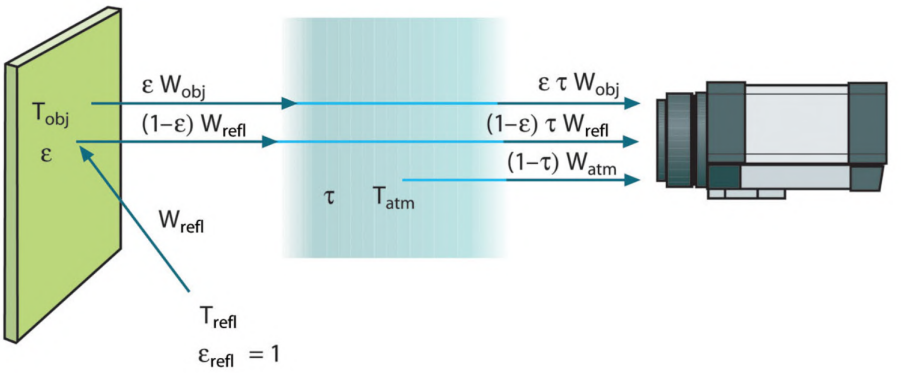

Figure 1.2: A schematic representation of the general thermographic measurement condition [9].

1.1.3 Thermal camera working principles

Thermal detectors work as two-step transducers [10]. First, the incident radiation is absorbed to change the temperature of a material. Second, the electrical output of the thermal sensor is produced by a change in some physical property of the material (e.g., temperature-dependent electrical resistance in a bolometer). At present, the bolometer principle is widely exploited by commercial IR cameras [1].

This section is devoted to the description of the procedure that thermal cameras exploit in order to quantify the signal of a radiating sample. When viewing an object, the thermal camera receives the radiation emitted by the object itself, but it also collects radiation from the surroundings that gets reflected by the object surface. Both these radiation contributions become attenuated to some extent by the atmosphere along the measurement path. A third radiation contribution comes from the atmosphere itself. This measurement condition is schematically illustrated in figure 1.2.

We assume that the received radiation power W from a blackbody source of temperature T_{source} on short distances generates a camera output signal Φ_{source} that is proportional to the power input (power linear camera). We can then write:

$$\Phi_{source} = C_{tc} \cdot W(T_{source}) = C \cdot W_{source} \tag{1.1.19}$$

where C_{tc} is a constant obtained by the camera manufacturer with a calibration procedure. When observing an opaque grey-body with emissivity ε at temperature T, the thermal camera senses a total radiation power [1, 9]

$$\Phi_{tot} = \varepsilon \mathcal{T}_{atm} \Phi_{obj}(T) + (1-\varepsilon)\mathcal{T}_{atm}\Phi_{amb}(T_{amb}) + (1-\mathcal{T}_{atm})\Phi_{atm}(T_{atm}) \quad (1.1.20)$$

where:

- $\varepsilon \mathcal{T}_{atm} \Phi_{obj}(T)$ is the radiant power contribution of the grey-body, with $\Phi_{obj}(T)$ corresponding to the radiant power detected by the thermal camera in the presence of a black body at the object temperature T. $\mathcal{T}_{atm}$ is the atmosphere transmittance and describes the attenuation of the emitted radiation in the atmosphere across the camera-sample distance d.
- $(1-\varepsilon)\mathcal{T}_{atm}\Phi_{amb}(T_{amb})$ accounts for the atmosphere-attenuated thermal radiation emitted by the surroundings at temperature T_{amb} and reflected by the grey-body with reflectance $(1-\varepsilon)$.
- $(1-\mathcal{T}_{atm})\Phi_{atm}(T_{atm})$ is the radiant power contribution of the atmosphere at temperature T_{amb}, with emissivity $(1-\mathcal{T}_{atm})$.

The radiant power $\Phi_{obj}(T)$ can be retrieved starting from the measured sensor signal Φ_{tot} [1, 9]:

$$\Phi_{obj}(T) = \frac{1}{\varepsilon \mathcal{T}_{atm}}\Phi_{tot} - \frac{1-\varepsilon}{\varepsilon}\Phi_{amb}(T_{amb}) - \frac{1-\mathcal{T}_{atm}}{\varepsilon \mathcal{T}_{atm}}\Phi_{atm}(T_{atm}) \quad (1.1.21)$$

In order for $\Phi_{obj}(T)$ to be evaluated via equation 1.1.21, the grey-body emissivity has to be provided to the thermo-camera acquisition software. The atmospheric transmittance $\mathcal{T}_{atm}$ is derived instead by the same software once the atmospheric temperature T_{atm}, the relative humidity and the camera-sample distance d are provided as input parameters. Together with T_{atm}, the ambient T_{amb} has to be provided to the camera software to enable computation of the two contributions $\Phi_{amb}(T_{amb})$ and $\Phi_{atm}(T_{atm})$. Then the calibration curve stored in the thermal-camera firmware provides the relation between the detected camera signal and the corresponding black-body temperature, and allows the final conversion of the experimental value $\Phi_{obj}(T)$ into the object temperature T via Stefan-Boltzmann's law.

It is worth remarking that focal plane arrays in commercial thermal cameras act as pixelated detectors. Therefore, experimentally measured temperature values are the result of the convolution of the temperature signal with the camera point-spread-function (as detailed in section 1.3), followed by a spatial average of the resulting temperature distribution over the pixel size. Such a spatial averaging procedure is obviously irrelevant for a spatially homogeneous temperature distribution within the camera pixel, but it turns particularly significant in the presence of temperature heterogeneities: it will be therefore extensively discussed throughout chapters 3 and 4, where the width of laser-primed temperature variations is typically much smaller than the camera pixel.

1.1.4 Active thermography

In most applications of IR imaging, the investigation is done passively, that is, the camera observes a scene and detects the thermal radiation emitted by the objects. This method is called *passive* since the existing temperature distribution is recorded without imposing an additional heat flow to the object, and the observed temperature patterns are due to existing temperature differences. A typical example is buildings inspection, where the temperature variation comes from the inside heating, while external walls are cooled by the surrounding air. The surface temperature differences measured by thermal imaging are caused by a spatial variation of the heat flow due to different thermal properties of the materials or constructions [1].

However, there are situations where natural temperature differences are absent or not sufficiently strong. In these cases *active* methods are needed. They are based on the heating (in principle, cooling is possible too) of the surfaces to be studied, in order to induce a non-stationary temperature distribution inside the sample. This heating can arise from different sources, such as absorption of radiation, current flow or ultrasound and can be either continuous, modulated or pulsed [1, 11]. Detection of heat transfer within the sample is performed by measuring the surface temperatures either in reflection or in transmission mode as a function of time.

The most important and widely established methods of active thermal imaging are pulse thermography and lock-in thermography, which have been constantly developed and improved since the late 1970s and which have made the fortune of thermal imaging for the industrial use. The aim of these methods is to detect, locate, and characterize buried material discontinuities in solids and for this reason they find application in the field of nondestructive testing and inspection of aircraft

components, solar panels or composite materials [12–15]. However, as I will show in this thesis, similar approaches of active thermography can be extended to the (label-free) absorption-based characterization of cultural heritage artifacts and biological specimens. In particular, I lay here the foundation of the transposition of active thermal imaging to super-resolution imaging.

It is worth remarking that, since active thermal imaging relies on transient external heating, the resulting temperature distributions follow the 3D heat equation in the presence of proper heat sources (i.e. the excitation laser beam in the case of temperature increments induced by laser light absorption). While Finite Element Methods (FEMs) represent the most promising tool for 3D heat transfer simulation [16], the analytical treatment of the heat equation can also be successfully exploited for the description and subsequent analysis of experimental data. In the next sections, I lay the foundations of (super-resolved) active thermal imaging by reporting the analytical treatment of the heat equation in the presence of focused laser-light illumination.

1.2 Heat equation under pulsed laser illumination

For the 3D heat transfer model we assume an opaque infinite solid slab of thickness L, isotropic thermal diffusivity D and thermal conductivity k, immersed in air. A volumetric heat source term $S = I\,(1-\mathcal{R})\,g\,(x,y)\,f\,(z)\,q(t)$ describes a low power ($\sim 10\,mW$) cw visible-to-infrared laser beam, that impinges on the sample at perpendicular incidence at $\mathbf{r} = (x,y,z) = (0,0,0)$. $I\,(1-\mathcal{R})$ is the laser-light intensity that is not reflected from the front surface at $z = 0$ ($\mathcal{R}$ is the sample reflectivity), $g(x,y)$ is the beam intensity distribution in the xy-plane, $q(t)$ describes the illumination time dependence and $f(z)$ provides the laser-light attenuation along the z-axis thickness. For a finite linear absorption coefficient α at the illumination wavelength, $f(z) = \alpha \cdot e^{-\alpha z}$ [17]. Henceforth, we assume temperature independent k and D, as justified by our typically small experimental temperature increments. The heat equation for the temperature $T(r,t)$ reads therefore

$$\frac{k}{D}\frac{\partial T(\mathbf{r},t)}{\partial t} - k\nabla^2 T\,(\mathbf{r},t) = S\,(\mathbf{r},t) \tag{1.2.1}$$

The temperature is continuous at the sample/air interfaces and boundary conditions are set by the balance of energy fluxes at $z = 0, L$:

$$\begin{cases} -k \left.\dfrac{\partial T(\mathbf{r},t)}{\partial z}\right|_{z=0} = -h\left[T(x,y,0,t) - T_m\right] - \varepsilon\sigma\left[T^4(x,y,0,t) - T_m^4\right] \\ -k \left.\dfrac{\partial T(\mathbf{r},t)}{\partial z}\right|_{z=L} = h\left[T(x,y,L,t) - T_m\right] + \varepsilon\sigma\left[T^4(x,y,L,t) - T_m^4\right] \end{cases} \tag{1.2.2}$$

Both convective and radiative losses are accounted for in the boundary conditions, where $T_m \sim 293$ K is the temperature of the surroundings, ε is the sample emissivity, σ is Stefan-Boltzmann's constant and h is the convective coefficient of surface heat transfer, which is assumed identical on the front and rear sample surfaces (we will hereafter refer to the convective loss coefficient as h instead of h_{conv} for the sake of brevity). For convenience, we introduce dimensionless variables

$$x^* = \frac{x}{\mathcal{L}}, \quad y^* = \frac{y}{\mathcal{L}}, \quad z^* = \frac{z}{\mathcal{L}} \tag{1.2.3}$$

where $\mathcal{L}$ is a characteristic length. Usually, the laser beam radius is taken as the characteristic length. For thin slabs, instead, the thickness L is usually chosen [17]. The normalized time and thickness are similarly defined as

$$t^* = \frac{D}{\mathcal{L}^2}t, \quad L^* = \frac{L}{\mathcal{L}} \tag{1.2.4}$$

We also introduce the dimensionless heat transfer and absorption coefficients as

$$h^* = \frac{h}{\mathcal{L}}, \quad \alpha^* = \alpha\mathcal{L} \tag{1.2.5}$$

The most general solution of the boundary-value problem (equations 1.2.1 and 1.2.2) obtained with the Green's function technique can be written as

$$\Delta T(\mathbf{x^*}, t^*) = \frac{\mathcal{L}^2}{k}\int_0^{t^*}\int_0^{L^*}\int_{-\infty}^{\infty}\int_{-\infty}^{\infty} \mathbb{G}(\mathbf{x^*}, t^*, \mathbf{x_1^*}, t_1^*) S(\mathbf{x_1^*}, t_1^*)\, d\mathbf{x_1^*}\, dt_1^* \tag{1.2.6}$$

where $\Delta T(\mathbf{x^*}, t^*) = T(\mathbf{x^*}, t^*) - T_m$, $S(\mathbf{x_1^*}, t_1^*)$ is an arbitrary source term and $\mathbb{G}$ is the Green's function, which can be obtained by the method of integral transformations [17]. In the specific case of finite absorption coefficient and negligible interference phenomena within the slab, the solution takes the form

$$\Delta T(x^*, y^*, z^*, t^*) = \frac{\mathcal{L}}{k} I\,(1-\mathcal{R})\int_0^{t^*} q(t^* - t_1^*)\mathcal{G}(x^*, y^*, t^*, t_1^*)\mathcal{F}(z^*, t_1^*)\, dt_1^* \tag{1.2.7}$$

Functions $\mathcal{G}$ and $\mathcal{F}$ describe the temperature field within the xy-plane and along the z-direction, respectively, and are given by

$$\mathcal{G}(x^*, y^*, t^*, t_1^*) = \frac{1}{4\pi t_1^*} \int_{-\infty}^{\infty} dx_1^* \int_{-\infty}^{\infty} dy_1^* g(x_1^*, y_1^*) \cdot \\ \cdot \exp\left(-\frac{(x_1^* - x^*)^2 + (y_1^* - y^*)^2}{4t_1^*}\right) \tag{1.2.8}$$

and

$$\mathcal{F}(z^*, t_1^*) = \alpha^* \sum_{n=-\infty}^{\infty} F_n(z^*, t_1^*) = \alpha^* \left[F_0(z^*, t_1^*) + 2\sum_{n=1}^{\infty} F_n(z^*, t_1^*)\right] \tag{1.2.9}$$

with

$$F_n(z^*, t_1^*) = A_n f_n(z^*, t_1^*)$$
$$f_n(z^*, t_1^*) = B_n Z_n(z^*) \exp(-\nu_n^2 t_1^*)$$
$$Z_n(z^*) = \left[\cos(\nu_n z^*) + \frac{h^*}{\nu_n} \sin(\nu_n z^*)\right]$$
$$B_n = \frac{\nu_n^2}{L^*(\nu_n^{*2} + h^{*2}) + 2h^*}$$

ν_n are roots of the equation

$$\tan(L^* \nu_n) = \frac{2\nu_n h^*}{\nu_n^2 - h^{*2}}$$

and the coefficients A_n are given by

$$A_n = \int_0^{L^*} Z_n(z_1^*) \exp(-\alpha^* z_1^*) dz_1^* = \\ = \frac{1}{\alpha^{*2} + \nu_n^2} \left\{ (\alpha^* + h^*) \left[1 - \cos(\nu_n L^*) \exp(-\alpha^* L^*)\right] + \right. \\ \left. + \frac{\nu_n^2 - \alpha^* h^*}{\nu_n} \sin(\nu_n L^*) \exp(-\alpha^* \mathcal{L}^*) \right\}$$

We are interested here in the explicit expression of equation 1.2.7 for Gaussian $g(x^*, y^*) = exp(-x^{*2} - y^{*2})$ and square-wave laser illumination ($q(t) = 1$ at times $t \leq \tau_{on}$ and $q(t) = 0$ at $t > \tau_{on}$, τ_{on} being the laser activation time). In this case,

$$\mathcal{G}(x^*, y^*, t^*, t_1^*) = \frac{1}{1 + 4t_1^*} \exp\left(-\frac{x^{*2} + y^{*2}}{1 + 4t_1^*}\right) \tag{1.2.10}$$

and

$$\Delta T(x^*, y^*, z^*, t^*) = \frac{\mathcal{L}}{k} I(1 - \mathcal{R}) \int_{t_0^*}^{t^*} \mathcal{G}(x^*, y^*, t^*, t_1^*) \mathcal{F}(z^*, t_1^*) dt_1^* \tag{1.2.11}$$

where $t_0^* = 0$ when $t^* < \tau_{on}^* \equiv D\tau_{on}/\mathcal{L}^2$ and $t_0^* = t^* - \tau_{on}^*$ when $t^* > \tau_{on}^*$. Under these conditions, no exact close-form analytical solution can be retrieved. However, approximated analytical solutions can be recovered under the assumptions of either thermally thin or infinitely thick sample and negligibile heat losses [17].

1.2.1 Approximation for thermally thin samples

Under the hypothesis of thermally thin sample (Biot number $hL/k \ll 1$) and negligible radiation losses, the temperature variation within the sample is small compared to the average temperature. The $\mathcal{F}$ function turns independent on the z-coordinate and can be approximated [17] as

$$\mathcal{F}(t_1^*) \approx \frac{1}{L^*} \exp\left(-\frac{2h^* t_1^*}{L^*}\right) \tag{1.2.12}$$

Substitution into equation 1.2.11 allows deriving the local temperature increment $\Delta T_{thin}(\mathbf{r}, t)$ that, expressed in terms of non-normalized variables and of the $1/e^2$ radius ω of the excitation laser beam, takes the form

$$\Delta T_{thin}(x, y, t) \approx \frac{I(1 - \mathcal{R}) D}{kL} \cdot \cdot \int_{t_0}^{t} \frac{\omega^2}{\omega^2 + 8Dt_1} exp\left(-\frac{2(x^2 + y^2)}{\omega^2 + 8Dt_1}\right) exp\left(-\frac{2Dht_1}{kL}\right) dt_1 \tag{1.2.13}$$

1.2.2 Approximation for thermally thick samples

Under the approximation of infinitely thick sample ($L \to +\infty$), surface absorption ($\alpha^* \to +\infty$), and negligible losses ($h^* = 0$), the $\mathcal{F}$ function can be expressed [17] as

$$\mathcal{F}(z^*, t_1^*) \approx \frac{1}{\sqrt{\pi t_1^*}} \exp\left(-\frac{z^{*2}}{4t_1^*}\right) \tag{1.2.14}$$

The substitution into equation 1.2.11 and the conversion to non-normalized variables provide the temperature increment as

$$\Delta T_{thick}(x, y, z, t) \approx \frac{I(1-\mathcal{R})D}{k} \cdot \int_{t_0}^{t} \frac{\omega^2}{\omega^2 + 8Dt_1} \exp\left(-\frac{2(x^2+y^2)}{\omega^2+8Dt_1}\right) \frac{1}{\sqrt{\pi D t_1}} \exp\left(-\frac{z^2}{4Dt_1}\right) dt_1 \tag{1.2.15}$$

In both equations 1.2.13 and 1.2.15, $t_0 = 0$ if $t < \tau_{on}$ and $t_0 = t - \tau_{on}$ if $t \geq \tau_{on}$.

Both the expressions for $\Delta T_{thin}(x, y, t)$ and $\Delta T_{thick}(x, y, z, t)$ prevent the analytical solution of the time integral. It is however straightforward to derive the complete space- and time-dependence of the temperature distribution by means of numerical integration. This strategy is exploited in the following for a first preliminary investigation of the amplitude and the width of laser-induced temperature increments for varying sample thickness and thermal properties.

1.2.3 Simulated temperature distributions

Temperature profiles have been numerically simulated according to equations 1.2.13 and 1.2.15. A laser activation time $\tau_{on} = 200\,ms$ and a fixed excitation beam waist $\omega = 30\,\mu m$ have been adopted (in analogy to the typical imaging conditions of the experiments reported in the next chapters), and the sample thermal conductivity has been adjusted in the 0.2-7 W/mK range to simulate the behaviour of exemplary materials (polycarbonate, glass and sodium chloride). Simulated temperature increments have been characterized in terms of the temporal evolution of the peak amplitudes $\Delta T_{thin}(0, 0, t)$ and $\Delta T_{thick}(0, 0, 0, t)$ (figure 1.3a,c), and of the spatial profiles $\Delta T_{thin}(x, 0, \tau_{on})$ and $\Delta T_{thick}(x, 0, 0, \tau_{on})$ at fixed $t = \tau_{on}$ (figure 1.3b,d). As expected, the peak amplitude of the temperature variation increases versus time during laser activation (reaching an equilibrium plateau provided τ_{on} is sufficiently

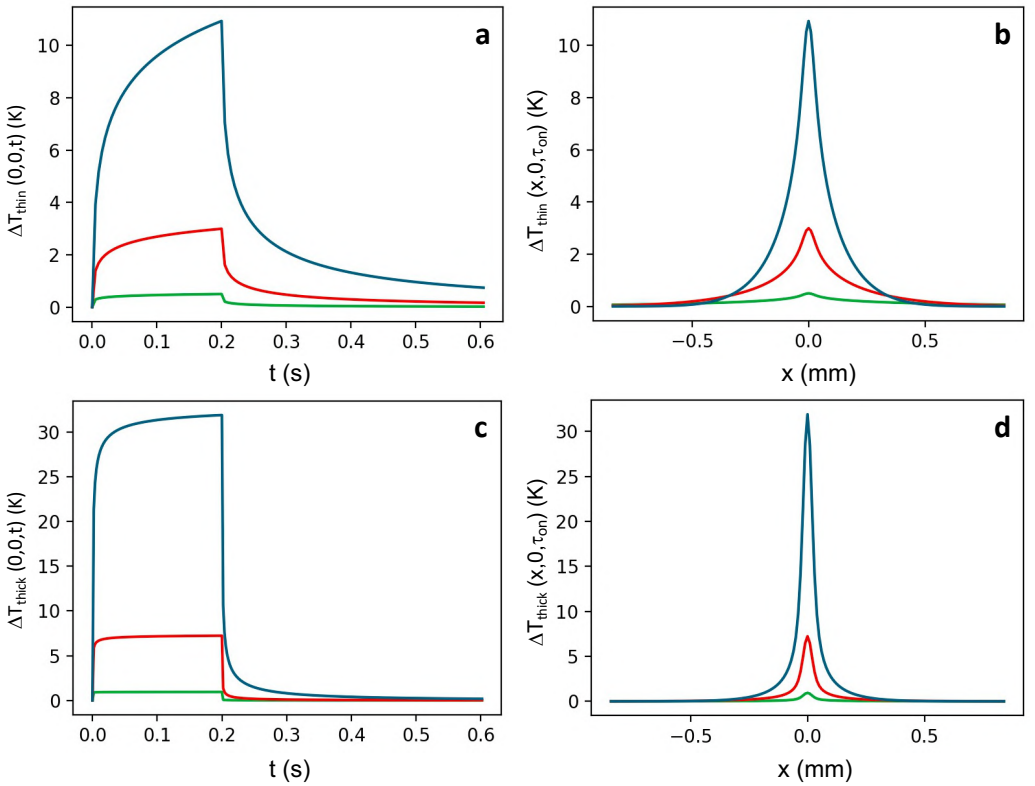

Figure 1.3: Theoretical temperature increments simulated in the thermally-thin (a,b) and thermally-thick (c,d) approximations, according to eq. 1.2.13 and 1.2.15. **(a)** Simulated temporal profile of the amplitude $\Delta T(x = 0, y = 0, t)$ of the temperature variation induced by a laser pulse with duration $\tau_{on} = 0.2\,s$ and absorbed power $P_{abs} = 0.5\,mW$ impinging on different materials at fixed $L = 100\,\mu m$: polycarbonate (blue, $D = 1.41 \times 10^{-7}\,m^2/s$, $k = 0.2\,W/mK$), glass (red, $D = 5.03 \times 10^{-7}\,m^2/s$, $k = 0.9\,W/mK$), NaCl (green, $D = 3.81 \times 10^{-6}\,m^2/s$, $k = 7\,W/mK$). **(b)** Simulated spatial profiles of the temperature increment at time $t = \tau_{on} = 0.2\,s$ for the same materials and sample thickness of panel (a). **(c)** Same as (a) for an infinitely thick sample. **(d)** Same as (b) for an infinitely thick sample. Excitation beam waist $\omega = 30\,\mu m$, $h = 10\,W/m^2K$ for all the panels.

long), and symmetrically decreases upon the source deactivation. At fixed time point, the spatial profile of the temperature increment appears as a skewed bell-shaped curve, and deviates from the Gaussian behavior that would otherwise be expected in the presence of free thermal diffusion in the absence of any heat source term.

It is worth anticipating here that the profiles reported in figure 1.3 describe the temperature variations effectively occurring on the sample plane, and do not coincide with the temperature signals detected by thermal imaging devices. This is due to the concurring effects of (i) the optical response function of the collecting lens of the thermal camera and (ii) the spatial average of thermal signals over the pixelated camera sensor. Both the effects are discussed in the following section.

1.3 Spatial resolution of infrared thermal imaging

Since thermography relies on the detection of infrared radiation through the lens of the thermal camera, the resolution of the imaging setup is limited by diffraction. Mathematically, the electric field diffraction through a lens can be expressed by a three-step propagation process [18–20]:

1. Free space propagation between the object plane $\Pi_0(\boldsymbol{\rho}_0)$ and the lens plane $\Pi_\xi(\boldsymbol{\rho}_\xi)$ (the adopted notational convention is shown in figure 1.4). In the paraxial approximation, this derivation is performed by applying the Fresnel diffraction integral

$$E_\xi(\boldsymbol{\xi}) = -i\frac{k_0}{s_0} e^{i2\pi k_0 s_0} e^{i\pi \frac{k_0}{s_0}\xi^2} \int E_0(\boldsymbol{\rho}_0) e^{-i2\pi \frac{k_0}{s_0}\boldsymbol{\rho}_0\cdot\boldsymbol{\xi}} e^{i\pi \frac{k_0}{s_0}\rho_0^2} d^2\boldsymbol{\rho}_0 \tag{1.3.1}$$

   where $s_0 = z_\xi - z_0$ and k_0 is the wavenumber $2\pi/\lambda$.

2. Passage through a lens of radius a, which acts as a quadratic phase shift on the light beam. More precisely, the field transmission of a thin lens is defined as

$$t(\boldsymbol{\xi}) = P(\boldsymbol{\xi}) e^{-i\pi \frac{k_0}{f}\xi^2} \tag{1.3.2}$$

   where f is the lens focal length and P is the pupil function

$$P(\boldsymbol{\xi}) = \begin{cases} 1 & \text{if} \quad \xi \leq a \\ 0 & \text{if} \quad \xi > a \end{cases} \tag{1.3.3}$$

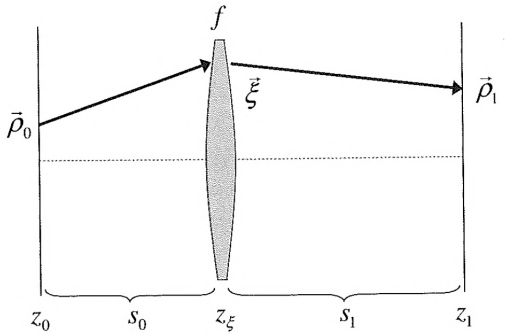

Figure 1.4: Geometry for optical propagation through a lens [20].

The field emanating from the lens is then

$$E'_\xi(\boldsymbol{\xi}) = t(\boldsymbol{\xi})E_\xi(\boldsymbol{\xi}) = \\ = -i\frac{k_0}{s_0}e^{i2\pi k_0 s_0}e^{i\pi k_0 \xi^2\left(\frac{1}{s_0}-\frac{1}{f}\right)}\int E_0(\boldsymbol{\rho_0})P(\boldsymbol{\xi})e^{-i2\pi\frac{k_0}{s_0}\boldsymbol{\rho_0}\cdot\boldsymbol{\xi}}e^{i\pi\frac{k_0}{s_0}\rho_0^2}d^2\boldsymbol{\rho_0} \quad (1.3.4)$$

3. Free space propagation between the lens plane $\Pi_\xi(\boldsymbol{\xi})$ and the image plane $\Pi_1(\boldsymbol{\rho_1})$, which is obtained again by the Fresnel diffraction integral, leading to

$$E_1(\boldsymbol{\rho_1}) = -\frac{k_0^2}{s_0 s_1}e^{i2\pi k_0(s_0+s_1)}e^{i\pi\frac{k_0}{s_1}\rho_1^2}\cdot \\ \cdot\iint E_0(\boldsymbol{\rho_0})P(\boldsymbol{\xi})e^{-i2\pi k_0\boldsymbol{\xi}\cdot\left(\frac{\boldsymbol{\rho_0}}{s_0}+\frac{\boldsymbol{\rho_1}}{s_1}\right)}e^{i\pi k_0\xi^2\left(\frac{1}{s_0}+\frac{1}{s_1}-\frac{1}{f}\right)}e^{i\pi\frac{k_0}{s_0}\rho_0^2}d^2\boldsymbol{\rho_0}d^2\boldsymbol{\xi} \quad (1.3.5)$$

where $s_1 = z_1 - z_\xi$.

Since we are interested in the imaging configuration described by the well-known thin-lens formula

$$\frac{1}{s_0}+\frac{1}{s_1}=\frac{1}{f}$$

equation 1.3.5 can be simplified as:

$$E_1(\boldsymbol{\rho_1}) \approx -\frac{k_0^2}{s_0 s_1}e^{i2\pi k_0(s_0+s_1)}e^{-i\pi\frac{k_0}{fM}\rho_1^2}\cdot\int E_0(\boldsymbol{\rho_0})\mathcal{P}\left(\frac{k_0}{s_1}\boldsymbol{\rho_1}+\frac{k_0}{s_0}\boldsymbol{\rho_0}\right)d^2\boldsymbol{\rho_0} \quad (1.3.6)$$

where $M = -\frac{s_1}{s_0}$ is the magnification factor and $\mathcal{P}$ is the Fourier transform of the pupil function P. In imaging applications, where we are interested only in the detected intensity at the image plane, the two phase factors outside the integral play no role and can be discarded [20]:

$$E_1(\boldsymbol{\rho_1}) \approx -\frac{k_0^2}{s_0 s_1} \int E_0(\boldsymbol{\rho_0}) \mathcal{P}\left(\frac{k_0}{s_1}\boldsymbol{\rho_1} + \frac{k_0}{s_0}\boldsymbol{\rho_0}\right) d^2\boldsymbol{\rho_0} \tag{1.3.7}$$

We can now introduce what is known as the Coherent Spread Function (CSF), which is simply a scaled version of the Fourier transform of the pupil function:

$$\begin{aligned} CSF(\boldsymbol{\rho}) = \left(\frac{k_0}{s_0}\right)^2 \int P(\boldsymbol{\xi}) e^{i2\pi\frac{k_0}{s_0}\boldsymbol{\rho}\cdot\boldsymbol{\xi}} d^2\boldsymbol{\xi} = \left(\frac{k_0}{s_0}\right)^2 \mathcal{P}\left(-\frac{k_0}{s_0}\boldsymbol{\rho}\right) = \\ = \pi a^2 \left(\frac{k_0}{s_0}\right)^2 \frac{J_1\left(2\pi\frac{k_0}{s_0}\rho a\right)}{2\pi\frac{k_0}{s_0}\rho a} \end{aligned} \tag{1.3.8}$$

where J_1 is the Bessel function of the first kind and a is the radius of the lens. The imaging relation given by 1.3.7 can now be expressed in terms of a convolution:

$$E_1(\boldsymbol{\rho_1}) \approx \frac{1}{M} \int E_0(\boldsymbol{\rho_0}) CSF\left(\frac{1}{M}\boldsymbol{\rho_1} - \boldsymbol{\rho_0}\right) d^2\boldsymbol{\rho_0} \tag{1.3.9}$$

For an incoherent light field, an analogous relation for the intensity can be found by applying the square modulus to the previous equation:

$$I_1(\boldsymbol{\rho_1}) \approx \frac{1}{M^2} \int I_0(\boldsymbol{\rho_0}) PSF\left(\frac{1}{M}\boldsymbol{\rho_1} - \boldsymbol{\rho_0}\right) d^2\boldsymbol{\rho_0} \tag{1.3.10}$$

where we introduced the Point Spread Function (PSF), which represents the response of an imaging system to a point source object:

$$PSF(\boldsymbol{\rho}) = \frac{|CSF(\boldsymbol{\rho})|^2}{\int |CSF(\boldsymbol{\rho})|^2 d^2\boldsymbol{\rho}} = \pi a^2 \left(\frac{k_0}{s_0}\right)^2 \left[\frac{J_1\left(2\pi\frac{k_0}{s_0}\rho a\right)}{2\pi\frac{k_0}{s_0}\rho a}\right]^2 \tag{1.3.11}$$

The shape of the PSF for a circular aperture is usually called Airy pattern and it plays a fundamental role in the quantification of the resolution achievable by an optical system.

Resolution defines the capability of distinguishing two equal-irradiance, incoherent and spectrally identical light sources. When the two sources are imaged by the same lens, two diffraction Airy patterns are produced, and they tend to blur and overlap into a single spot when the distance between the sources is reduced; the two objects are said to be resolved when the center of the first Airy disc falls on the first minimum of the second Airy pattern. The corresponding minimum center-to-center distance between the point-like sources is given by Abbe's law [20]:

$$\Delta = 0.61 \frac{\lambda}{NA} \tag{1.3.12}$$

where λ is the wavelength of light and NA is the numerical aperture, that can be written as:

$$NA = n \sin \beta \tag{1.3.13}$$

where n is the index of refraction of the embedding medium and α is the maximal half-angle of the cone of collected light.

Now, I would like to estimate the theoretical diffraction limit in our experimental situation (thermal cameras FLIR E40 and FLIR T650sc, FLIR Systems Inc., OR, USA). If we call a the radius of the thermal camera lens and d the distance between the detection lens and the sample plane, we have

$$a = d \tan \beta \tag{1.3.14}$$

a can be calculated using the values of f and $f_\#$ stated by the manufacturer [9] (respectively $f = 18\,mm$ and $f_\# = 1.3$ for the FLIR E40 camera, $f = 18\,mm$ and $f_\# = 1.0$ for the FLIR T650sc camera), obtaining $a = \frac{f}{2f_\#} = 6.9\,mm$ for the E40 camera and $a = 9\,mm$ for the T650sc camera.

The camera-sample distance d equals $30\,cm$ and $40\,cm$ for the E40 and the T650sc cameras, respectively. Hence, we get the same numerical aperture $NA = n \sin \beta = 0.023$ for both the configurations. Finally, the same resolution limit given by Abbe's law applies to the two employed thermal cameras and is given by

$$\Delta = 0.61 \frac{\lambda}{NA} = 265\,\mu m \tag{1.3.15}$$

Δ has been computed with $\lambda = 10\,\mu m$, equal to the middle value of the working range of the thermal camera (7.5-13 μm).

1.3.1 Temperature distributions imaged by the thermal camera

Equation 1.3.10 highlights that the detected intensity on the image plane is the convolution of the intensity distribution on the object (sample) plane with the camera Point Spread Function. Based on the quartic temperature dependence of the radiance in Stefan-Boltzmann's law, the signal sensed by the thermal camera should be derived starting from the fourth power of the temperature distribution on the sample plane. In other words, the convolution is computed as $T^4(x, y, 0, t) * PSF(x, y, 0)$ (for the sake of convenience, we adopt here the same notation of section 1.2, and identify the sample plane with coordinates x, y, and $z = 0$).

The PSF, provided by the Airy pattern of equation 1.3.11, can be approximated by a Gaussian curve with full width at half height Δ assigned by Abbe's law. Under the typical imaging conditions adopted in the present work, $\Delta = 265\,\mu m$ is much higher than the width of temperature peaks primed by focused laser-light illumination with beam waist $\omega \sim 30\,\mu m$ on the $\sim 100\,ms$ time-scale. The result is a pronounced broadening of the imaged temperature spatial distribution. This is exemplified in figure 1.5a,b with the comparison of a theoretical temperature increment predicted on the sample plane for a thermally-thin slab (eq. 1.2.13) with the corresponding PSF-convoluted temperature profile.

In the case of pixelated detectors (e.g., focal plane arrays in commercial thermal cameras), the resulting convoluted temperature distribution is also subject to a spatial average over the extended pixels of the image sensor. Pixel (i, j) will sense a space-averaged temperature increment

$$\overline{\Delta T}_{i,j} = \left\{ \frac{1}{l^2} \iint_{i,j} N \cdot [T^4(x, y, 0, t) * PSF(x, y, 0)] dx dy \right\}^{1/4} - T_m \tag{1.3.16}$$

where the integral runs over the area of pixel (i, j) having side length l. The convolution normalization factor N is defined as

$$N = \frac{\iint_{-\infty}^{\infty} T^4(x, y, 0, t) dx dy}{\iint_{-\infty}^{\infty} T^4(x, y, 0, t) * PSF(x, y, 0) dx dy} \tag{1.3.17}$$

Again, the effect of the spatial average procedure is exemplified in figure 1.5a-c, with the comparison of the aforementioned temperature profile predicted on the sample plane for a thermally-thin slab with the corresponding PSF-convoluted and pixelated temperature profile ($l = 420\,\mu m$). Figure 1.5c effectively represents a

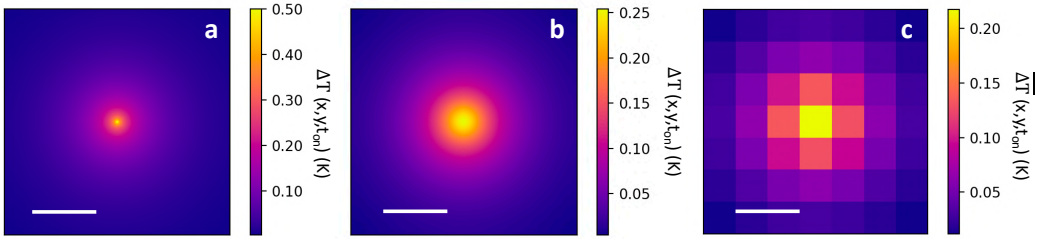

Figure 1.5: Effect of the camera PSF and of the pixel size on detected temperature increments. **(a)** Simulated spatial temperature profile on the front surface of a thermally thin sample ($D = 3.81 \times 10^{-6}\,m^2/s$, $k = 7\,W/mK$, $L = 100\,\mu m$) at time $t = \tau_{on} = 0.2\,s$ ($\omega = 30\,\mu m$, absorbed power $P_{abs} = 0.5\,mW$, $h = 10\,W/m^2K$). **(b)** Result of the convolution of the fourth power of the temperature profile exploited for panel (a) with the camera PSF ($\Delta = 265\,\mu m$). **(c)** Synthetic thermal-camera image produced by PSF-convolution and spatial average of the temperature distribution in (a) over square pixels with side $l = 420\,\mu m$. Scale bar: $850\,\mu m$. The numerical integration of eq. 1.2.13 and the computation of the PSF convolution have been performed by a custom-written Python code.

synthetic thermal camera image, analogous to the ones experimentally collected and employed throughout the next chapters.

The combined effect of the camera PSF and of the camera extended pixel size is explored in more detail in figure 1.6. The result of the PSF-convolution and of the pixel-wise spatial average is reported for the same simulated temperature profiles of figure 1.3 in both the thermally-thin and thermally-thick regimes. Beside evidencing the PSF-related broadening of temperature spatial profiles, figure 1.6b,d reveal that spatial temperature profiles imaged by a pixelated optical sensor can be effectively approximated by a Gaussian distribution. The comparison of figures 1.3 and 1.6 also reveals that the amplitude of temperature increments detected by the thermal camera is lowered relatively to the amplitude of the temperature variations effectively occurring on the sample plane, and that the characteristic rise time of the temperature signal as a function of time is remarkably increased. Anticipated here, these effects will retain a crucial importance in chapter 2, where the Gaussian surface fit of experimentally detected temperature peaks will enable their accurate localization, and in chapter 4, where both the amplitude and the exponential rise time of laser-induced temperature variations will be exploited for the quantification of thermal conductivity values.

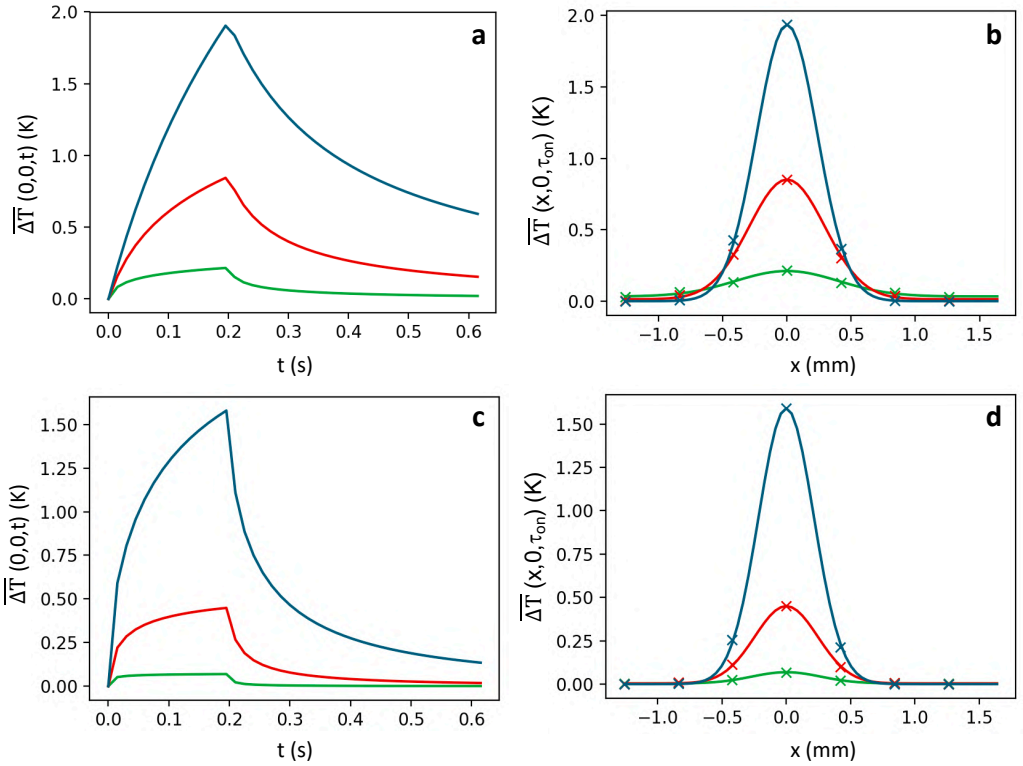

Figure 1.6: Simulated temperature increments in the thermally-thin (a,b) and thermally-thick (c,d) approximations, as predicted according to eq. 1.3.16 for a pixelated detector with pixel size $l = 420\,\mu m$ and point-spread-function width $\Delta = 265\,\mu m$. **(a)** Simulated temporal profile of the amplitude $\overline{\Delta T}(0,0,t)$ of the temperature variation induced by a laser pulse with duration $\tau_{on} = 0.2\,s$ and absorbed power $P_{abs} = 0.5\,mW$ impinging on different materials at fixed $L = 100\,\mu m$: polycarbonate (blue, $D = 1.41 \times 10^{-7}\,m^2/s$, $k = 0.2\,W/mK$), glass (red, $D = 5.03 \times 10^{-7}\,m^2/s$, $k = 0.9\,W/mK$), NaCl (green, $D = 3.81 \times 10^{-6}\,m^2/s$, $k = 7\,W/mK$). **(b)** Simulated spatial profiles of the temperature increment at time $t = \tau_{on} = 0.2\,s$ for the same materials and sample thickness of panel (a). Symbols represent temperature values averaged over square pixels, overlaid to the best Gaussian fit (continuous lines). **(c)** Same as (a) for an infinitely thick sample. **(d)** Same as (b) for an infinitely thick sample. Excitation beam waist $\omega = 30\,\mu m$, $h = 10\,W/m^2K$ for all the panels.

Chapter 2

Super-resolution photo-thermal imaging

In this chapter, I present the principles of a novel super-resolution infrared thermal imaging approach capable of overcoming the diffraction limit affecting conventional thermography and of achieving $\sim 50\,\mu m$ spatial resolution on variably extended (submillimeter- to centimeter-sized) fields of view. This technique is the common thread of the entire thesis: while I focus here on the conceptualization and the experimental validation of the imaging approach, the next chapters are devoted to the extension of the technique to the quantification and spatial mapping of relevant structural and thermo-physical properties of the imaged samples.

2.1 Motivation

Active photo-thermal imaging over submillimeter- to centimeter-sized fields of view with tunable spatial resolution in the $\sim$ 10-100 μm range is a valuable tool for the nondestructive characterization of the morphology and functional state of biological tissues. In the clinical and pre-clinical setting, for example, active medical thermography allows identifying the modified blood perfusion and metabolic activity associated to the presence of inflammations, cancer masses or physiological dysfunctions by accessing the resulting alterations in the tissues thermo-physical properties (e.g., the thermal conductivity [21], or the sample temperature during thermal relaxation phases [22]). Externally induced temperature variations also provide direct access to the spatial distribution of sample components, as demon-

strated with melanin for the identification of age-related macular degeneration in the retina [23] or the discrimination of in-situ and invasive malignant skin lesions in the context of melanoma screening and diagnosis [24, 25]. In nanomedicine and nanotechnological research, photo-induced heat release events allow characterizing the distribution of nanoparticles following systemic injection in animal model systems, and the development of related photo-thermal therapy protocols.

Overall, active medical thermography finds promising applications ranging from the development of quantitative screening tools for the (early-stage) detection of pathologies, to the characterization of disease progression and therapy response in forefront pre-clinical research. High resolution active thermal imaging is equally relevant to monitor the dissipation efficiency or detect the fault of electronic devices and micro-electro-mechanical systems [26, 27], or to perform quality controls on the thermo-conduction properties of materials [28, 29]. For all these applications, morphological imaging of the sample structure would benefit from achieving a spatial resolution lying well below the millimeter range.

Existing approaches reaching the highest (sub-micrometer) spatial resolution include fluorescence-based thermometry, where temperature is probed via its effect on the intensity, anisotropy and lifetime of the fluorescence emission of dyes, proteins and nano-constructs [30–33], and scanning thermal microscopy, that relies on the near-field interaction between a surface and a heated tip [34–38]. While being applicable in principle to the detection of externally (e.g., optically or electrically) induced temperature variations, these techniques are usually exploited to map the intrinsic temperature in the sample with sub-micrometer resolution over relatively small ($< 100\text{x}100\ \mu m^2$) regions. On the other hand, in the context of active thermography, the exploitation of the response of optical properties (reflectivity and index of refraction) to a modulated change in the sample temperature is at the basis of scanning thermo-reflectance microscopy [27, 39–41] and PHoto-thermal Imaging (PHI) [25, 42–45]. In the case of PHI, temperature increments are indirectly monitored by the variations in the refractive index: as a result, PHI images allow mapping the absorbers distribution, but cannot easily be converted into temperature maps. Scanning thermo-reflectance imaging can reach nanoscale spatial resolution and provides quantitative measurement of the induced temperature variations after sample-dependent calibration [27]. It finds however its best application in the characterization of electronic and opto-electronic devices [27, 46]; the sample coating with a thin metal transducer layer, which is often required to improve the sensitivity [47–49], may limit the applicability to biological systems.

More straightforward access to temperature values, coupled to imaging over

wider areas, can be achieved by infrared thermal imaging [1, 10, 50]. Upon calibration of the sample emissivity [1, 50, 51], temperature increments can be quantified non-invasively based on Stefan-Boltzmann's law by the measurement of the infrared radiance in the grey-body approximation (as reported in sections 1.1.2 and 1.1.3). However, the typical ~ 1-100 °C range of interest corresponds to peak radiances in the ~ 7-13 μm band [50] (Wien's law): even though expensive thermo-cameras with pixel size as low as 5-20 μm on the sample plane exist in commerce, the effective resolution is limited to ~ 0.1-1 mm [52–55] due to the thermal waves diffusion in the sample and to the diffraction of the far-infrared radiation at the low numerical aperture of Germanium or Zinc-Selenide optics. The mm-sized diffraction limited resolution of conventional thermography severely limits the applicability to high-resolution thermal characterizations and motivates the development of a super-resolution imaging approach capable of non-invasive, quantitative, spatially resolved temperature (and thermal conductivity) measurements on both biological and inorganic samples.

2.2 Experimental quantification of the thermo-camera spatial resolution

As discussed in section 1.3, the thermal camera spatial resolution is theoretically limited by the phenomenon of diffraction of far-infrared radiation at the camera collecting lens, and can be quantified as 265 μm for our thermal camera (FLIR E40, FLIR Systems Inc., USA) at the 10 μm wavelength lying at the center of the detection range. Nevertheless, the thermal camera does not work in ideal conditions, and other factors may contribute to worsen the spatial resolution that is effectively achieved. A first significant limitation is associated in our case to the extended size of the camera pixels on the sample plane (~ 400 μm at the minimum focus distance of the camera): it is clear that two point-like objects inside a region of at least 800 μm, that corresponds to the length of two consecutive pixels, cannot be resolved. Secondly, the resolution measurement is complicated by heat propagation. As predicted by the heat equation, any sub-resolved temperature peak would be subjected to an inevitable enlargement associated to heat diffusion in the sample, with the enlargement turning more and more pronounced as time elapses. Therefore, the resolution should ideally be evaluated by laser-priming a sub-resolved localized temperature increment on the sample, by quantifying its width as a function of time and by extrapolating the width of the temperature peak

at time point $t \to 0$ (at the very beginning of laser illumination, before any heat propagation takes place).

2.2.1 Resolution extrapolation from a single-pulse illumination profile

Aiming at the detection of a sub-resolved laser-primed temperature increment, I have taken advantage of a uniform ink printed microfiche sample subjected to focused laser light illumination (633 nm wavelength, $56 \pm 2\ \mu m$ beam $1/e^2$ diameter) with a long exposure time $\tau_{on} = 25\ s$. The ink provides a pronounced photo-thermal effect and, as anticipated with the more detailed discussion of section 1.3.1, the temperature profiles acquired by the thermal camera during laser illumination, reported in figure 2.1a-b, are well approximated by a best-fit Gaussian trial function of the type

$$\overline{\Delta T}(x,t) \simeq \overline{\Delta T}(t) e^{-\frac{(x-x_c)^2}{2\zeta(t)^2}} \tag{2.2.1}$$

The time dependence of the amplitude $\overline{\Delta T}$ and of the standard deviation ζ can be obtained by fitting every thermal camera frame along the illumination and relaxation phases to this Gaussian function. As reported in figure 2.1c, $\overline{\Delta T}(t)$ shows an exponential growth-and-decay temporal behavior. The time profile of the standard deviation $\zeta(t)$ (figure 2.1d) shows an initial increase up to the equilibrium plateau during laser illumination, followed by a faster increase during free heat diffusion upon the laser de-activation. This profile demonstrates the aforementioned enlargement of the laser-induced temperature increment due to heat propagation as a function of time. By extrapolating the profile full width at half maximum ($\sqrt{2\ln(2)}\zeta(0)$) at time $t \to 0$, it is possible to remove the effect of the heat diffusion and provide an unbiased resolution value for the thermal camera in its conventional operation. Based on figure 2.1d,

$$\Delta_{eff} = 2\sqrt{2\ln(2)}\zeta(0) = (1400 \pm 200)\ \mu m \tag{2.2.2}$$

This value, together with the theoretical Abbe's diffraction limit, will be recalled throughout the rest of the chapter as a comparison value to evaluate the performance and quantify the resolution enhancement of the proposed super-resolution imaging approach. It is also worth remarking that the temperature peak broadening (the $\zeta(t)$ profile) depends on the thermal properties (thermal conductivity and diffusivity) of the heated sample. The extrapolation at time-point zero eliminates such a dependence and allows deriving a resolution estimate that is independent

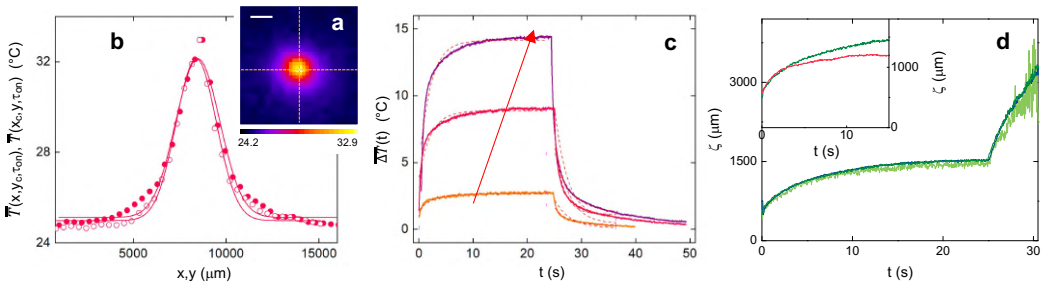

Figure 2.1: (a) Thermo-camera frame acquired at time $t = \tau_{on}$ by detecting the thermal radiation of a uniform ink square produced by microfiche printing illuminated at its center by a square-wave pulse at 633 nm with $\tau_{on} = 25\,s$ and power $P = 6\,mW$. Scale bar: 2850 μm. **(b)** Experimental x- and y- temperature profiles indicated by yellow lines in (a) (filled and open symbols, respectively) overlaid to the best Gaussian fit to eq. 2.2.1. **(c)** Time dependence of the amplitude $\overline{\Delta T}$ obtained by a Gaussian fit of the temperature variations induced by a single pulse with duration $\tau_{on} = 25\,s$ at the center of a uniform black ink square produced by microfiche printing. Excitation power $P = 3\,mW$, $6\,mW$ and $9\,mW$, increasing in the direction of the arrow. Dashed red lines are the best exponential growth and decay fits. **(d)** Time dependence of the standard deviation $\zeta(t)$ obtained by a Gaussian fit of the temperature variations induced by a single pulse with duration $\tau_{on} = 25\,s$ at the center of the uniform microfiche ink square; laser power on the sample plane $P = 9\,mW$ (navy), $6\,mW$ (green) and $3\,mW$ (light green). The $\zeta(t)$ profile is independent on the laser power. Inset: comparison of the standard deviation time profiles recovered under identical conditions ($P = 6\,mW$) on the microfiche sample and on a uniform black inkjet-printed square on paper (green and red, respectively). The intercept $\zeta(0)$ is the same for both the materials. Excitation beam $1/e^2$ diameter $= (56 \pm 2)$ μm for all the curves.

on the specific sample material. This is demonstrated in the inset of figure 2.1d, where the $\zeta(t)$ profile recovered on the microfiche-printed ink sample is compared to the analogous $\zeta(t)$ profile quantified on a uniform ink square printed on a paper support.

2.2.2 Resolution worsening due to heat diffusion

As already noticed, the method proposed in the previous section produces a resolution estimate that is not dependent on heat diffusion effects. However, a finite laser dwell time is always necessary to obtain a detectable temperature increment: in practical situations, thermal camera images are always collected at a certain time point following laser activation, so that the resolution limit predicted by equation

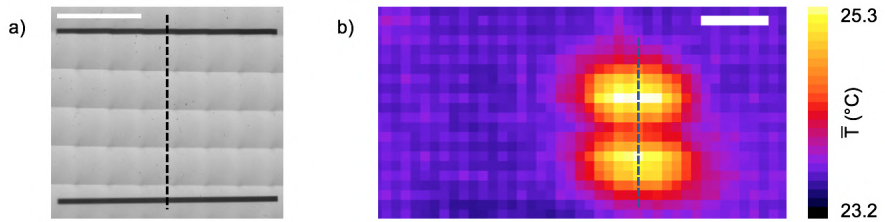

Figure 2.2: (a) Conventional transmitted-light image of two parallel ink stripes (90 μm in thickness and separated by a 3.2 mm distance) produced by microfiche printing. The grid effect is due to the mosaic (tile-scan) procedure used to acquire such an extended area. Scale bar: 1.66 mm. **(b)** Thermal image of the same stripes. Scale bar: 2.73 mm. In both (a) and (b) the dashed lines represent the direction chosen for the profiles plotted in figure 2.3.

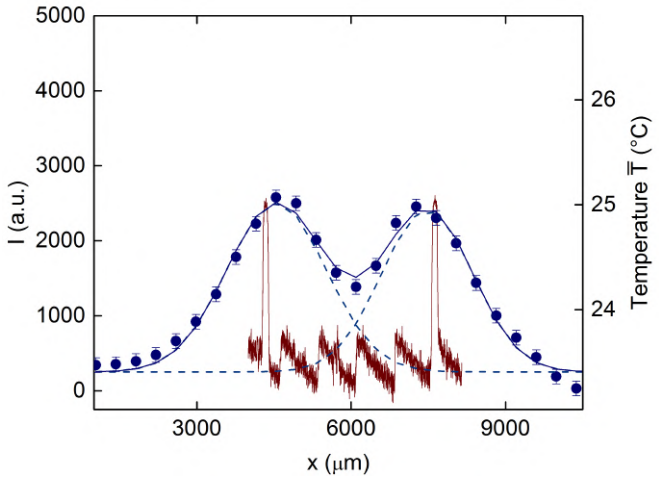

Figure 2.3: Red solid line: intensity profile extracted from the transmitted-light image in figure 2.2a; the sawtooth trend is due to the tile-scan (mosaic) image acquisition procedure. Blue circles: temperature profile from the thermal image in figure 2.2b. Blue continuous and dashed line: double-Gaussian fit of the temperature profile.

2.2.2 cannot be really achieved.

An example is reported in figure 2.2b with the thermal image of two sub-resolved parallel ink stripes printed on a microfiche support. The stripes are $90\,\mu m$ thick and are separated by a $3.2\,mm$ distance, as verified by conventional transmission microscopy (figure 2.2a and red profile in figure 2.3). The thermal image of the stripes has been obtained as the maximum projection of the raw stack acquired by the thermal camera during a fast raster-scanning illumination of the sample ($P = 18\,mW$ laser power on the sample plane, $3\,ms$ pixel dwell time). The temperature profile along the direction perpendicular to the stripes shows two partially overlapping peaks that can be distinguished by means of a double-component Gaussian fit (figure 2.3). The average full width at half maximum of the two Gaussian peaks equals $(2180 \pm 90)\,\mu m$, and reveals that each sub-resolved ink stripe is imaged with an effective width that is higher than the expected resolution estimated by equation 2.2.2. Since heat diffusion is time- and material- dependent, the situation could be even worsened by increased pixel dwell times or in the presence of sample substrates with larger thermal diffusivity.

2.3 Photo-activated thermography at sub-diffraction resolution

Having discussed and quantified the effective spatial resolution of our thermal camera in conventional operation, I outline here the fundamental principles of the image acquisition and processing scheme that we have specifically conceived to overcome Abbe's diffraction limit in the field of infrared thermography. The strategy relies on sparsely priming heat release in the sample via modulated raster-scanned laser-light illumination, and on subsequently identifying absorptive centers based on the accurate localization of the resulting isolated laser-induced temperature variations. To this aim, a low power Gaussian laser beam, with wavelength lying within the sample absorption band (here, $\lambda_{exc} = 633\,nm$), is focused on the sample with beam $1/e^2$ radius ω. It is convenient to consider at first the simple case of a single square-wave excitation pulse of duration τ_{on}, centered at (x_0, y_0). If the laser beam impinges on light absorbing and heat releasing entities (Fig. 2.4a), an approximately Gaussian 2D temperature distribution is observed in the acquired thermal camera images (Fig. 2.4b). The Gaussian amplitude obeys a temporal exponential rise and decay, with the maximum value at time τ_{on} equal to $\overline{\Delta T}_{max} = T_{max} - T_0$, where T_0 is the equilibrium sample temperature in the absence

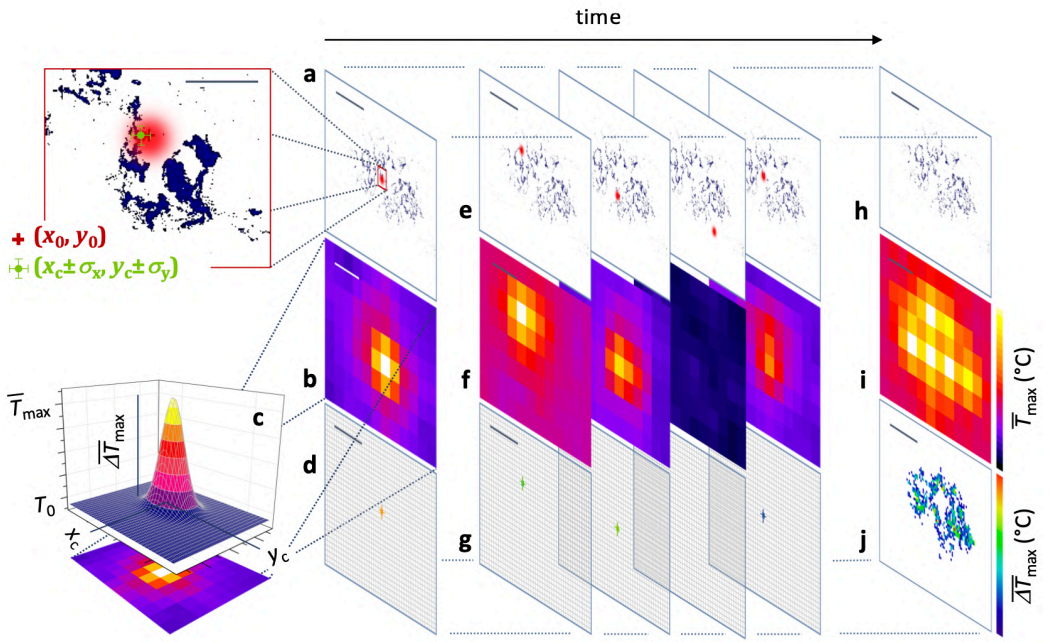

Figure 2.4: Photo-activated thermal imaging at sub-diffraction resolution. A Gaussian laser beam (red spot in (a)) is focused on the sample at (x_0, y_0) with a square pulse of duration τ_{on}. Light absorbing entities (blue) induce a local temperature increase, which is measured by the thermo-camera as an evolving 2D Gaussian peak. A Gaussian fit (c) of the frame collected at time τ_{on} (b, c) provides the temperature variation $\overline{\Delta T}_{max} = T_{max} - T_0$ and the peak coordinates $(x_c \pm \sigma_x, y_c \pm \sigma_y)$ that localize the center of the distribution of the absorbing objects within the laser spot size (magnified region in (a)). The procedure is repeated over sets of isolated points as exemplified in (e, f). The center coordinates provided by the Gaussian fit of temperature peaks identify the position of the absorbing entities on the scan grid (d, g) with uncertainty $\sigma_{x,y}$ and a color code assigned by the best-fit $\overline{\Delta T}_{max}$. A maximum projection of the signal across the raw thermo-camera image sequence provides a low ($\sim$ mm) resolution image of the sample (i), whereas a maximum projection of the stack containing all the localized absorptive centers provides the super-resolution image (j) of the scanned region (h). Scale bars (100 µm in the magnification of (a), 1000 µm elsewhere) indicate the typical imaged fields of view; note that the $\sim$ 50-µm laser spot and the whole magnified area in (a) lie within a single $\sim$ 400-µm typical thermo-camera pixel on the sample plane. All panels have been derived from experimental data acquired on an explanted murine skin biopsy treated with 30-nm Prussian blue nano-cubes analogous to the one employed in section 2.7.

of illumination. A non-linear 2D Gaussian fit of the temperature peak at time τ_{on} provides the amplitude $\overline{\Delta T}_{max}$, together with the Gaussian center coordinates (x_c, y_c) (Fig. 2.4c). Importantly, x_c and y_c identify the center of the distribution of the laser-excited absorbing objects within the area assigned by the excitation laser spot size. For a given thermal camera pixel size, the uncertainty $\sigma_{x,y}$ in the determination of the best-fit coordinates (x_c, y_c) is a function of the number of collected infrared photons and can be made arbitrarily small at increasing laser power and temperature variations. Therefore, localization of absorbing objects can be performed well below the theoretical resolution limit set by the diffraction of far-infrared radiation at the thermal camera collecting lens. Achievement of sub-diffraction information by the localization of sparse signal peaks has indeed been demonstrated by well-established techniques including Single Particle Tracking [56, 57] and the fluorescence-based PALM (Photo-Activated Localization Microscopy) [58] and STORM (STochastic Optical Reconstruction Microscopy) [59].

In order to reconstruct a super-resolution image across extended areas, the procedure of illumination and localization of absorbing centers is sequentially repeated (fig. 2.4e). A minimum distance Δx between pairs of consecutively irradiated points and/or a minimum time interval Δt in between their illumination have to be adopted to ensure that the two temperature variations appear as spatially and/or temporally separate peaks in the thermal camera images. This is crucial to enable the correct localization of the center of each detected temperature increment by Gaussian fitting. To this aim, a modulated laser illumination is adopted here: the sample is raster scanned by the focused laser beam while a synchronized shutter allows modulating the laser activation and de-activation. The scan grid, $N_x \times N_y$ pixels in format, has a pixel size $\delta x \sim 10\,\mu m$ and is oversampled relatively to the $\sim$ 400-μm thermo-camera pixel size on the sample plane. During each raster-scan, illumination (open-shutter condition) is only allowed on the limited subset of isolated pixels lying on a square lattice with characteristic spacings Δx and Δy along the horizontal and vertical directions, respectively (fig. 2.5). Complete coverage of the investigated area is achieved when the raster scan is repeated $\Delta x \Delta y$ times, since for each scan only $N_x N_y/(\Delta x \Delta y)$ pixels get illuminated. The laser pixel dwell time coincides with the shutter opening time ($\sim$ 100-1000 ms) during laser activation, whereas a $\sim 2\,ms$ dwell time is selected during shutter closure. This results in a total acquisition time $t_{tot} = N_x N_y \tau_{on} + N_x N_y \tau_{off}(\Delta x \Delta y - 1) \sim$ 10-100 minutes over millimeter-sized areas depending on τ_{on}, N_x, N_y, Δx and Δy (fig. 2.5).

During the scanning, the thermal camera acquires frames at rate f_{rate}, providing a typical 10^4-10^5 frames sequence (fig. 2.4b,f). If a maximum projection of the signal

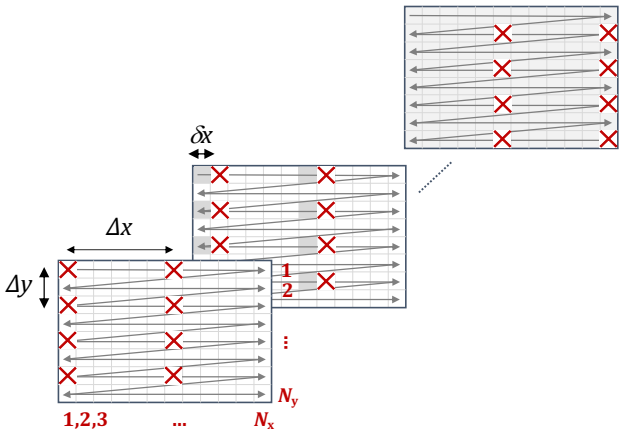

Figure 2.5: Schematic of the adopted raster-scanning modulated illumination scheme, depicted here with the first, second and last scans (from left to right) of a hypothetical exemplary acquisition. The laser beam is scanned uni-directionally (grey arrows) along a conventional raster path with grid size $N_x \times N_y$ and pixel size δx, but during a single complete raster scan illumination is only allowed (i.e., the shutter is only opened) on a limited set of isolated pixels (red crosses; grey pixels in each panel are those that have been illuminated during previous scans, whereas white pixels are those still to be illuminated by the laser beam). Δx is the minimum distance (in pixel units) between two consecutively illuminated pixels along the x-direction, while Δy defines the distance between the nearest lines where the shutter can be opened (for convenience sake, values for Δx and Δy are chosen among the divisors of N_x and N_y, respectively).

is performed along the time axis of the raw image stack, a low-resolution thermal image - resembling the one that would be produced under wide-field illumination of the sample - is obtained (fig. 2.4i). By contrast, when the center coordinates and amplitudes of all the detected temperature peaks are determined by Gaussian fitting and are associated to the corresponding pixel along the scan grid (fig. 2.4d,g), the center coordinates provide much better resolved topological information on the absorptive centers in the sample. Best-fit amplitudes encode the information on the sample absorption and local induced temperature variations, and provide the color code for the final super-resolution image that is obtained by superimposing all the color-coded pixels where absorptive centers have been localized (fig. 2.4j).

Significantly, if the scan pixel size and the localization uncertainty are smaller than the laser beam radius (δx, $\sigma_{x,y} \ll \omega$), the spatial resolution of the reconstructed

image is ultimately limited by the VIS/NIR excitation spot which can be focused at will down to a diffraction-limited $\sim 1\,\mu m$ size. In this regard, it is worth remarking that the visible-wavelength ($633\,nm$) beam is exploited to prime emission of thermal signal at much longer (far infrared) wavelength and is still subject to light diffraction: the proposed imaging approach allows overcoming the diffraction limit for the thermal wavelengths of the detected signal only. This is an important difference with respect to the PALM [58] and STORM [59] techniques, that instead allow super-resolving objects located inside the excitation laser spot.

2.3.1 Image reconstruction algorithm

Raw data for super-resolution thermography consist in the aforementioned image sequence of $\sim 10^4$-10^5 frames acquired by the thermal camera during the modulated laser illumination of the sample. The analysis is entirely performed offline, upon completion of the data acquisition. Due to the $\sim 10 \times 8\,cm^2$ field of view of the thermal camera employed here, the analysis is restricted to a Region Of Interest (ROI) covering the scanned area and easily identified by computing the maximum projection over the time axis of the acquired image stack. For each pixel i within the ROI, the temperature-versus-time profile $T_i(t)$ may contain N temperature peaks with approximately exponential rise and decay. Each peak is produced by a laser square pulse impinging on light-absorbing and heat-releasing entities located within the i-th pixel or in pixels nearby (due to heat diffusion). Since the scan pixel size δx oversamples the thermal camera pixel l ($\delta x \sim$ 10-100 μm, $l \sim 400\,\mu m$), tens to hundreds of peaks can be detected in a single $T_i(t)$ plot; peak amplitudes vary according to the distance of the illuminated heat-releasing objects from pixel i and from the center (highest-intensity portion) of the excitation laser spot at the time of illumination. A pattern-recognition algorithm can be exploited to locate the position of each peak on the time axis of the $T_i(t)$ profile. In the present case, fits to a 1D symmetric Gaussian function (that reasonably approximates the exponential rise and decay for the short adopted $\tau_{on} = 0.1$-$1\,s$) are performed by sliding a fit window over the entire time trace. The temporal coordinate of each local temperature maximum is stored, and the corresponding frame of the thermo-camera image stack is fitted to a Gaussian surface for the sub-diffraction localization of the center coordinates (x_c, y_c) of the laser-induced temperature increase. Surface Gaussian fits are performed in two steps: a first fit to a symmetric 2D Gaussian function with fixed variance provides the peak coordinates, which are fixed in a second step to recover the variance and the amplitude. Double-step fits

allow a minimization of the uncertainty associated to the localized peak coordinates [60].

Once the procedure has been repeated for all the pixels in the ROI, the peak coordinates (x_c, y_c) and amplitudes $\overline{\Delta T}_{max}$ of all the identified temperature increments are exploited to reconstruct the super-resolution image of the scanned area. Since the pixel size in the final image coincides with the pixel size δx of the scan grid, a bin size δx is employed to group all the best-fit peak coordinates (x_c, y_c) into the corresponding pixels along the scan grid. Then the highest among the $\overline{\Delta T}_{max}$ values associated to the temperature variations contained in each pixel is selected to provide the color-code for the pixel itself. A minimum threshold on rendered temperature increments (referred to as ΔT_{min}) is generally employed to exclude very low and spurious temperature variations that might be erroneously detected by the peak identification algorithm even in the absence of light absorption on noisy frames. The threshold does not eliminate any true laser-induced temperature variation, since the typical $\overline{\Delta T}_{max}$ values are at least twice as high as ΔT_{min}. I finally remark that the rendered image can be reported either with the amplitude of temperature variations (as in the present case), or with the absolute values obtained by summing temperature variations to the baseline temperature in the absence of laser illumination.

2.4 Materials and methods

2.4.1 Experimental setup

Figure 2.6 shows a schematic of the experimental photo-thermal imaging setup, that has been constructed and optimized based on the principles of the illumination-and-localization imaging approach. Sample absorption is primed by a He-Ne laser beam ($\lambda_{exc} = 633\,nm$, Thorlabs, NJ, USA) with 30-mW maximum output power. Grey filters are employed to adjust the laser power on the sample plane and achieve a minimum $0.1\,^{\circ}C$ temperature variation with a relatively short illumination time $\tau_{on} \sim$ 10-1000 ms. The excitation spot size on the sample plane may be adjusted by a two-lens Keplerian beam reducer with focal lengths f_1 and f_2: the $1/e^2$ beam diameter ranges from $56 \pm 2\,\mu m$ in the absence of the beam reducer down to $22 \pm 1\,\mu m$ with $f_1 = 3\,cm$ and $f_2 = 10cm$. When necessary, an Argon laser beam (Spectra Physics, CA, USA) at 488 and 514 nm can be employed as excitation source with typical $30 \pm 2\,\mu m$ waist and $\sim 30\,mW$ laser power on the sample plane.

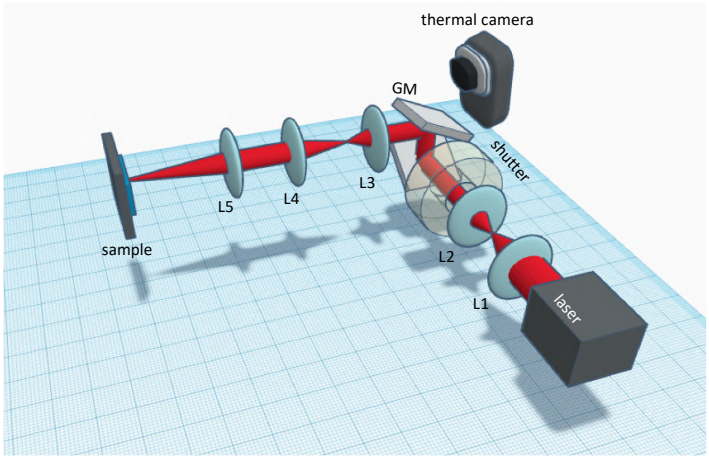

Figure 2.6: Photo-thermal imaging setup. Schematic of the setup employed for photo-activated thermal imaging at sub-diffraction resolution (L1-L5, lenses; GM, galvanometric mirrors).

A scanning unit with servo-board electronics and a pair of galvanometric mirrors (MicroMax Series 670, Cambridge Technology Inc., MA, USA) is coupled to a two-lens scan system ($f_3 = 4\,cm$, $f_4 = 10\,cm$), followed by beam focalization ($f_5 = 10\,cm$) onto the sample plane. The mirror positioning system is driven by a National Instrument board (LabVIEW RIO, National Instruments, TX, USA). Mirrors are operated in conventional raster-scanning mode (typical pixel size, 10-100 μm on the sample plane), with user-defined voltage values supplied to the mirrors to regulate the scan path length along the horizontal and vertical axes.

The board employed to drive the scan system is also exploited to synchronize the galvanometric mirrors with the electronic shutter (Oriel 76992, Newport, CA, USA; 150 Hz maximum operation frequency) aimed at modulating the laser illumination in time. During laser de-activation (i.e., shutter closure), a default 2-6 ms pixel dwell time of the laser beam along the scan grid is usually adopted. During laser activation, the shutter opening time is set to the desired value τ_{on} and the laser pixel dwell time is temporarily increased to the same value to ensure the sample illumination occurs at the same location. A simple practical criterion can be adopted to choose τ_{on} irrespectively of the sample thermal properties: based on the desired temperature peaks amplitude (i.e., the desired signal-to-noise ratio, which will impact in turn on the peaks localization uncertainty and the achievable

resolution), we adopt the minimum laser illumination time and the maximum laser power that ensure the achievement of such a desired signal amplitude while avoiding any sample photo-damage.

The detection of thermal radiation is performed by an uncooled microbolometer-based thermal camera (FLIR E40, FLIR Systems Inc., OR, USA) with 30-Hz frame rate. The detector provides 320x240 images, with $\sim 400\,\mu m$ pixel size on the sample plane. As detailed with the measurement procedure in section 1.1.3, the thermo-camera automatically corrects for the atmospheric attenuation and the sample reflection of the thermal radiation emitted by the surroundings. To this aim, the sample distance from the camera front lens, the sample emissivity ε, and the relative humidity and temperature of the atmosphere have to be provided to the camera software. A 50% humidity has been assumed for all the experiments of the present work, whereas the sample distance ($\sim 30\,cm$) and the ambient temperature have been measured for each imaging experiment. The emissivity has been experimentally characterized by the black-tape method [1] for both microfiche ink samples ($\varepsilon = 0.8$) and biological specimens ($\varepsilon = 0.95$) as described in sections 2.6.1 and 2.7.1. Finally, imaging of a known-size object at constant temperature has been exploited before each experiment to calibrate the pixel size and take small variations associated to the thermo-camera positioning into account.

All the experiments have been performed with a maximum 20° vertical tilt of the thermal camera with respect to the sample. Such a thermal camera tilt does not impact on measured $\overline{\Delta T}_{max}$ values, nor it impacts on the size of imaged objects [60].

2.4.2 Sample preparation

Microfiche-printed samples

Microfiche printing has been employed to produce reference ink patterns with convenient shape and known sub-resolved size for the initial experimental demonstration of super-resolution photo-thermal imaging. Patterns have been designed as white shapes over a black background (microfiche printing produces the negative of the original drawing). The pattern linear dimensions have been selected based on the desired size on the final printed film, taking the 28-times reduction factor of the printing procedure into account. Imaging by conventional transmission microscopy at 633 nm allows inspecting the uniformity of the printed ink layers as in fig. 2.9.

Prussian Blue nanocubes

Prussian Blue NanoParticles (PBNPs) have been synthetised according to the protocol in [61, 62] starting from $10\,mM\,FeCl_3(Fe^{III})$, $10\,mM\,K_4[Fe(CN)_6](Fe^{II})$ and $0.025\,M$ citric acid reagents. Solutions have been heated to $60°C$ during the synthesis and then allowed to cool at room temperature. Purification has been performed by ultracentrifugation for 25 min at 13000 rpm, followed by pellet re-suspension in half the original volume. The synthesis leads to cubic nanocrystals with an average side of $(29 \pm 8)\,nm$, as measured by TEM imaging, and with an absorption band peaked at $700\,nm$.

Murine skin biopsies

Murine skin biopsies have been explanted from the flank derma of sacrificed Balb/c mice at 6 weeks of age. Explanted tissue sections have been embedded in OCT freezing medium (Biooptica, I), cut in 10-μm sections on a cryostat and adhered to glass slides (Superfrost Plus, Thermo Fisher Scientific, MA, USA) for photo-thermal imaging. All the experiments have been performed under protocols approved by the Institutional Animal Care and Use Committee of the University of Milano-Bicocca and the Italian Ministry of Health.

Data analysis softwares

Photo-thermal imaging raw data have been acquired with the thermo-camera software (FLIR Tools +, FLIR Systems Inc., OR, USA), exported in .csv file format and entirely processed by a custom written Python code. Both non-linear 1D fits of temperature time profiles and the symmetric, asymmetric and skewed Gaussian surface fits of detected 2D temperature peaks have been performed by the same code with the curve fitting routine of the Scipy open source Python tool. Reconstructed super-resolution images have been saved as .txt files and rendered with ImageJ (US National Institutes of Health, MD, USA) for visualization and look-up table adjustment. Their comparison with the results of transmitted-light imaging has been accomplished by the Origin Pro 8 software (Origin Lab Corporation, MA, USA) based on temperature and intensity profile plots.

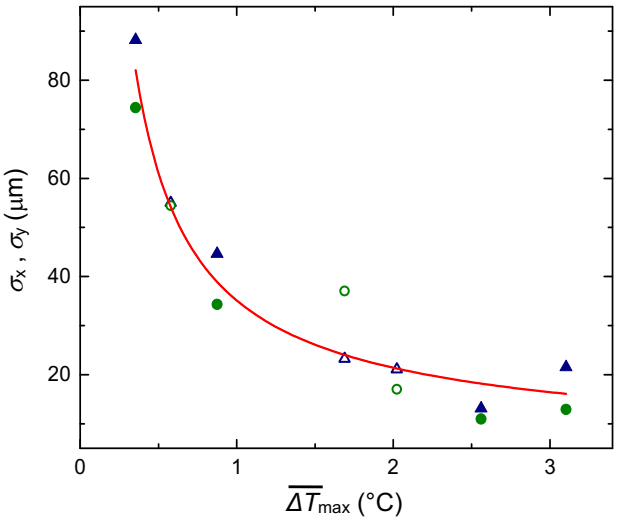

Figure 2.7: Localization uncertainties σ_x (triangles) and σ_y (circles) on the peak coordinates x_c and y_c reported as a function of $\overline{\Delta T}_{max}$ for the microfiche ink square (filled symbols) and the microfiche ink stripe (open symbols). The red solid line is the best global fit to eq. 2.5.1 with parameters $\gamma_1 = 600 \pm 220\,°C\mu m^2$ and $\gamma_1 = 630 \pm 130\,°C^2\mu m^2$. A power $P = 4.6\,mW$ and an excitation beam $1/e^2$ diameter $56 \pm 2\,\mu m$ have been exploited.

2.5 Quantification of the localization uncertainty

The theoretically attainable resolution assigned by the excitation spot size is only achieved if the coordinates (x_c, y_c) retrieved from the Gaussian fit of temperature peaks are determined with an uncertainty $\sigma_{x,y} \ll \omega$. In practical cases where $\sigma_{x,y}$ is comparable to ω, both contribute in defining the experimental resolution in the reconstructed images.

$\sigma_{x,y}$ depends on the signal-to-noise ratio of the fitted thermal camera images (i.e., on the number of detected photons, which is related in turn to the amplitude of the temperature variations). Aiming at the experimental quantification of $\sigma_{x,y}$, custom black ink patterns have been produced by microfiche printing: a uniform extended ($0.4x0.4\,cm^2$) ink square and a sub-resolved $30\,\mu m$ ink stripe have been subjected to periodical laser illumination at a fixed spatial location, and the repeatability in the localization of the ~ 150 resulting consecutive temperature variations has been evaluated. Specifically, the localization uncertainty has been quantified by the

standard deviations σ_x and σ_y of the localized center coordinates x_c and y_c of the consecutively induced temperature peaks. Measurements have been performed at increasing $\tau_{on} = 0.1\text{-}4\,s$: provided τ_{on} is shorter than the time required to reach a temperature plateau, changing τ_{on} allows inducing temperature increments of variable amplitude.

The results obtained on the uniform microfiche ink square are reported in figure 2.7. The standard deviations σ_x and σ_y of the localized center coordinates x_c and y_c exhibit a monotonically decreasing trend as a function of the amplitude $\overline{\Delta T}_{max}$ of the detected thermal signal. Similar results have been obtained in the case of the microfiche ink stripe with 30-μm width, which only partially covers the excitation spot with $1/e^2$ diameter $56 \pm 2\,\mu m$ (figure 2.7): plotting the uncertainties σ_x and σ_y resulting from the two-step Gaussian fit as a function of the best-fit $\overline{\Delta T}_{max}$ for both the ink square and the ink stripe reveals that all data points lie along the same expected curve [58, 63]:

$$\sigma_{x,y} \approx \sqrt{\frac{\zeta^2 + l^2/12}{N} + \frac{4\sqrt{\pi}b^2\zeta^3}{lN^2}} \approx \sqrt{\frac{\gamma_1}{\overline{\Delta T}_{max}} + \frac{\gamma_2}{\overline{\Delta T}_{max}^2}} \tag{2.5.1}$$

ζ in equation 2.5.1 is the standard deviation of the Gaussian function employed for the 2D fit of thermal camera frames, l is the thermo-camera pixel size on the sample plane and b is the number of background photons in the fitted images. Constants γ_1 and γ_2 have been introduced for the sake of compactness and N is the number of collected infrared photons, which is directly proportional to the induced temperature increment based on Stefan-Boltzmann's law [1]:

$$N \propto \varepsilon\sigma(T_{max}^4 - T_0^4) = \varepsilon\sigma((T_0 + \overline{\Delta T}_{max})^4 - T_0^4) \approx 4\varepsilon\sigma T_0^3 \overline{\Delta T}_{max} \tag{2.5.2}$$

With our typical $T_0 = 293\,K$ and $\overline{\Delta T}_{max} = 2\,K$ the approximation of equation 2.5.2 only results in a 1% underestimate of the exact value; the approximation holds within a 5% underestimate up to $\overline{\Delta T}_{max} = 10\,K$. The fit of the trend of $\sigma_{x,y}$ versus $\overline{\Delta T}_{max}$ to equation 2.5.1 (figure 2.7, best-fit parameters $\gamma_1 = 600 \pm 220\,°C\mu m^2$ and $\gamma_2 = 630 \pm 130\,°C^2\mu m^2$) allows extrapolating the localization uncertainty at any measured $\overline{\Delta T}_{max}$, thereby providing the estimate of $\sigma_{x,y}$ for all subsequent experiments on synthetic samples. Importantly, with typical detected temperature increments of $\sim 2\,K$ the localization uncertainty can be as small as $\sim 20\,\mu m$: combined to a $\sim$ 10-50 μm laser spot, such a localization uncertainty is sufficiently low to overcome the diffraction limit in super-resolution acquisition mode. It is finally

worth remarking that the similarity of the results obtained on the microfiche ink square and the microfiche ink stripe confirms that the exploitation of the same Gaussian fitting routine is justified irrespectively of the specific distribution of absorptive entities within the laser spot.

2.6 Proof-of-principle experiments on synthetic samples

Microfiche samples with desired shape and characteristic sub-resolved dimensions in the $\sim$ 10-100 μm scale have been subsequently exploited to perform proof-of-principle experiments aimed at validating the proposed super-resolution imaging approach.

2.6.1 Emissivity measurement

While black-bodies behave like perfect isotropically diffuse emitters, real grey-body surfaces may display a dependence of the emissivity ε on the angle of observation with respect to the surface normal [1, 51]. It is therefore important that the emissivity is measured at the very same detection angle subsequently exploited for photo-thermal imaging.

The emissivity of both synthetic and biological samples has been measured following the black-tape method suggested in the literature [1]. Half of the sample is covered by black matte tape of known angle-independent emissivity ($\varepsilon_{tape} = 0.95$) and, under thermal equilibrium, two regions of interest (ROIs) centered on the tape and on the sample, respectively, are selected on the thermal camera frames. While the emissivity ε_{tape} is employed for the temperature measurement in the tape ROI, an emissivity ε is set on the sample: the correct sample emissivity ε can then be found by varying it in the camera software until the thermal image provides the same temperature for the tape and sample ROIs. If the procedure is repeated by rotating the sample with respect to the thermal camera surface normal, the angle-dependence of the emissivity can be accessed and quantified as schematically depicted in figure 2.8.

The emissivity of microfiche samples has been measured on ink-printed areas at increasing tilt of the sample with respect to the thermal camera, covering the broad range $\theta = 0°$-$40°$ (at fixed $\phi = 0°$). No noticeable dependence on the angle of observation has been revealed in the experimental emissivity values (fig. 2.8) up to a 20° tilt (results agree with the literature, reporting constant emissivity from the

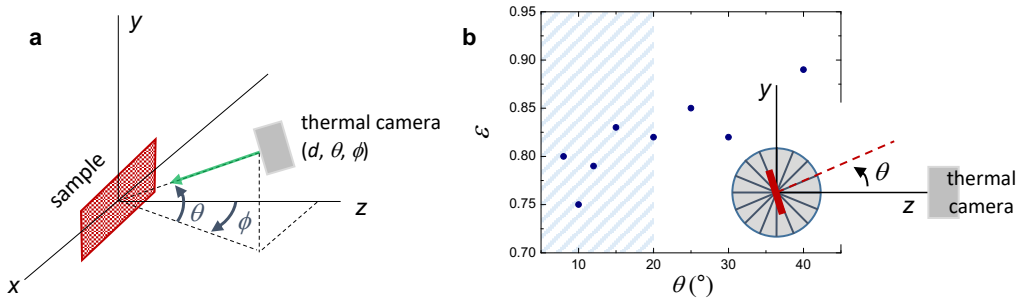

Figure 2.8: Emissivity angular dependence for microfiche samples. **(a)** Sketch of the thermal camera orientation with respect to the sample. The thermal camera points to the sample along the green arrow; ϕ defines the tilt in the horizontal xz-plane, whereas θ defines the vertical tilt in the yz-plane ($\phi = \theta = 0°$ corresponds to normal sample observation). **(b)** Emissivity of the microfiche samples (ink printed areas) as a function of the observation angle θ at fixed $\phi = 0°$. All the super-resolution imaging experiments of the present work have been performed with $\theta < 20°$ where the average emissivity equals $\varepsilon = 0.80 \pm 0.03$ (mean $\pm$ standard dev.). Inset: schematic of the setup for the measurement of the emissivity angular dependence. The microfiche sample (red) is attached to an angular scale, and half of the sample front surface is covered with black matte tape of known emissivity ($\varepsilon_{tape} = 0.95$ independently from the observation angle): under thermal equilibrium, the object emissivity can be found by varying ε in the camera software until the thermal image provides the same temperature for the sample and the tape. The procedure is repeated at increasing θ values by rotating the object to retrieve the emissivity dependence on the angle.

normal direction up to at least $\theta = 40°$-$45°$ for the majority of materials [1]). The average value $\varepsilon = 0.80 \pm 0.03$ recovered under the typical imaging geometry ($\phi = 0°$ and $\theta = 0°$-$20°$) has been therefore exploited for the analysis of photo-activated super-resolution thermal imaging experiments on microfiche samples.

2.6.2 Super-resolution imaging results

A LABS-shaped structure (acronym for Laboratory of Advanced BioSpectroscopy - fig. 2.9a) has been reconstructed first. The temperature variations induced by modulated illumination and localized by two-step Gaussian fitting of the thermo-camera frames have been exploited to render the final super-resolution image of the sample (fig. 2.9c). Visual inspection of fig. 2.9c already suggests

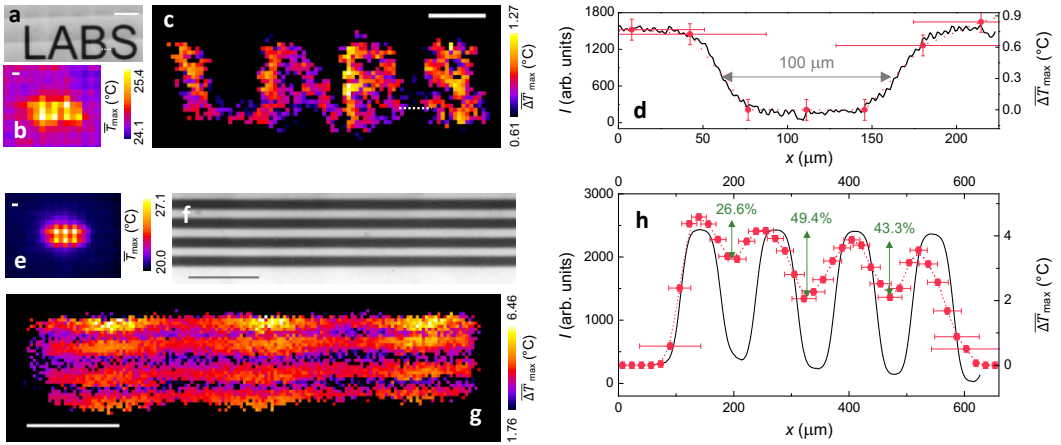

Figure 2.9: Proof-of-principle experiments. **(a),(f)** Transmitted-light images of microfiche samples. **(b),(e)** Temporal maximum projection of the raw thermo-camera image stacks acquired with modulated illumination on the samples in (a) and (f), respectively; acquisition parameters: $N_x \times N_y = 120 \times 36$, $\delta x = 34.4\,\mu m$, $\Delta x = 60$, $\Delta y = 6$, $\tau_{on} = 300\,ms$, $P = 4.6\,mW$, beam $1/e^2$ diameter $56 \pm 2\,\mu m$ in (b), $N_x \times N_y = 160 \times 42$, $\delta x = 15.3\,\mu m$, $\Delta x = 160$, $\Delta y = 6$, $\tau_{on} = 300\,ms$, $P = 15\,mW$, beam diameter $22 \pm 1\,\mu m$ in (e). **(c),(g)** Super-resolution images of the samples in (a) and (f), obtained from the image stacks employed for (b) and (e), respectively; $\Delta T_{min} = 0.3°C$ in (c), $0.7°C$ in (g). **(d)** Black: intensity profile along the dashed line in (a) upon a lookup-table inversion on the image; red: $\overline{\Delta T}_{max}$ profile along the dashed line in (c). **(h)** Black: average intensity profile along the vertical direction in (f) upon lookup-table inversion; red: average $\overline{\Delta T}_{max}$ profile along the vertical direction in (g) with contrast percentages between adjacent peaks. In (d),(h), uncertainties on $\overline{\Delta T}_{max}$ values equal the thermo-camera sensitivity $0.1°C$ and x-axis error bars for non-zero $\overline{\Delta T}_{max}$ values are extrapolated from the $\sigma_{x,y}$-versus-$\overline{\Delta T}_{max}$ plot (fig. 2.7). Scale bars: $500\,\mu m$.

proper reconstruction of the features of the printed pattern, and the $(0.14 \pm 0.01)\,°C$ standard deviation of the measured temperature variations (fig. 2.10) is close to the thermal camera sensitivity $\sigma_T = 0.1\,°C$ as stated by the producer (FLIR Inc., USA); the distribution of detected temperature variations is therefore compatible with the high sample homogeneity, in terms of ink distribution, shown by the transmitted-light image of the sample. None of the letters of the LABS pattern would instead be recognized by the thermal camera in conventional operation, as can be seen on the temporal maximum projection of the whole stack of the raw thermo-camera images in fig. 2.9b.

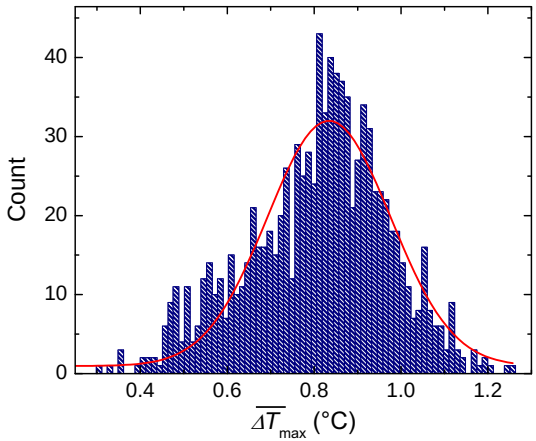

Figure 2.10: Histogram of $\overline{\Delta T}_{max}$ values over all the pixels of fig.2.9c. The standard deviation $(0.14 \pm 0.01)\,^{\circ}C$ of the detected temperature values is close to the thermal camera sensitivity $\sigma_T = 0.1\,^{\circ}C$ as stated by the producer (FLIR Inc., USA). It therefore confirms that the sample is uniform in terms of the absorption properties.

Quantitatively, the accuracy of the image reconstruction algorithm is demonstrated in fig. 2.9d by the comparison with the transmitted-light image of the same sample. The spatial profile of $\overline{\Delta T}_{max}$ values drawn along the spacing between the letters B and S of the ink pattern correctly superimposes to the corresponding intensity profile in the transmitted-light image, within the 30-50 μm localization error $\sigma_{x,y}$ expected from the values of $\overline{\Delta T}_{max} = 0.6\text{-}0.9^{\circ}C$ (fig. 2.7). The agreement between temperature variations and transmitted-light intensity profiles should further increase at increasing observed $\overline{\Delta T}_{max}$ (increasing laser intensity or activation time and decreasing $\sigma_{x,y}$). Still, the localization error $\sigma_{x,y}$ of the reported data-set allows discriminating absorbing structures (in fig. 2.9d, the letters B and S) 100 μm apart.

The 100 μm resolution achieved in figure 2.9c-d already demonstrates a 2.6-time gain with respect to the theoretical 265-μm diffraction-limited resolution of our thermal imaging setup. The resolution has been pushed further by both increasing the excitation laser power (and the detected $\overline{\Delta T}_{max}$ values) and reducing the spot $1/e^2$ diameter to $22 \pm 1\,\mu m$. A microfiche sample reproducing a grid of uniform ink stripes, 60 μm in width and relative distance (fig. 2.9f), has been imaged by modulated illumination yielding the super-resolution image in fig. 2.9g. Again, the

structures that would be unresolved in conventional thermal imaging (as shown by the temporal maximum projection over the raw image stack in fig. 2.9e) appear instead discernible in the super-resolved frame. The comparison with the transmitted-light (200-nm resolution) image of the same sample quantitatively confirms that the size of the imaged ink stripes is correctly retrieved (fig. 2.9h). Furthermore, the average spatial profile of temperature increments detected orthogonally to the ink stripes satisfies the 26.4% contrast threshold required by the well-known Rayleigh's criterion [64], thereby quantifying in $\leq 60\,\mu m$ the achieved resolution (fig. 2.9h). This corresponds to a 4.4-time gain relatively to the diffraction-limited prediction, and a 23-time gain with respect to the (1400 ± 200)-μm effective thermo-camera resolution in conventional operation (section 2.2).

2.7 Sub-diffraction thermal imaging on biological samples

Sub-diffraction thermal imaging has been finally tested on biological systems with sparse distributions of visible-light absorbers. I have taken advantage of explanted murine skin biopsies treated with 30-nm Prussian blue nanocubes (PBNPs), which exhibit a highly efficient thermal relaxation upon VIS/nearIR irradiation [61, 62]. The synthesis protocol [61, 62] allows producing nanocrystals with cubic shape and an average side of $(29 \pm 8)\,nm$, measured by TEM imaging (fig. 2.11b). The absorption band peaks at 700 nm, with a relative 60% absorbance at the 633-nm wavelength that we employ for photo-thermal imaging (fig. 2.11a).

2.7.1 Emissivity measurement

The emissivity of nanoparticle-treated skin sections has been measured under the same camera configuration ($\phi = 0°$ and $\theta = 20°$, cf. figure 2.8) adopted for super-resolution thermography. In order to evaluate the potential spatial variability of the emissivity across the skin tissue section, we can assume that the sample emissivity is everywhere comprised between: (i) the emissivity ε_{glass} of the bare glass coverslip, and (ii) the emissivity ε_{PBNP} of a solution of PBNPs cast on the glass coverslip at the very same concentration C employed for the NPs injection in the treated tissue section. Indeed, ε_{glass} would apply to all the pixels of the reconstructed image located outside the skin section, whereas ε_{PBNP} would apply to the pixels containing the nanoparticles at the highest possible concentration C. Since the remaining pixels would contain an intermediate local concentration of

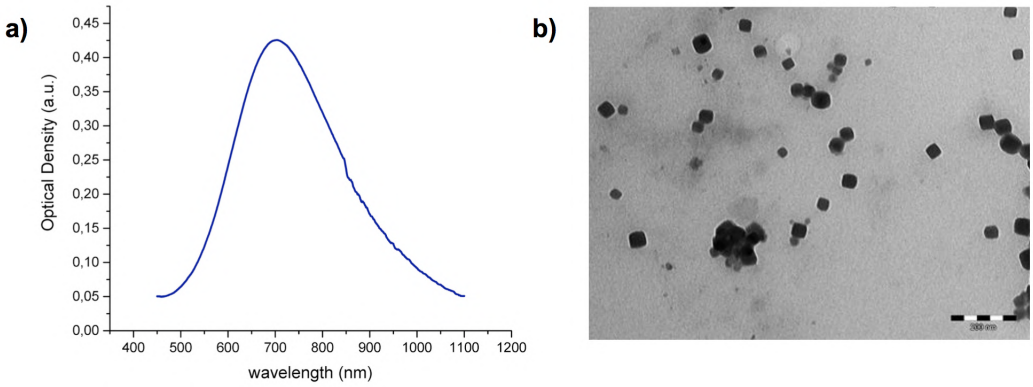

Figure 2.11: a) Prussian blue nanoparticles absorption spectrum. b) TEM image of Prussian blue nanoparticles. Scale bar: 200 nm.

nanoparticles, it is reasonable to assume the emissivity in those pixels could not exceed ε_{PBNP}. When the nanoparticles distribution and local concentrations are not known a priori (as in the present case), the range ε_{glass}-ε_{PBNP} provides the possible emissivity values for every pixel of the reconstructed thermal image.

I have therefore characterized both ε_{glass} and ε_{PBNP} by the black-tape method (as in section 2.6.1). Based on the results ($\varepsilon_{glass} = 0.93$ and $\varepsilon_{PBNP} = 0.97$), an average emissivity of 0.95 has been subsequently adopted for the datasets collected on all the murine biopsies (note ε_{PBNP} does not differ significantly from the emissivity of bare skin, values between 0.95 and 0.98 being reported in the literature for both human and murine skin [52, 65, 66]). At the same time, the range ε_{glass}-ε_{PBNP} has

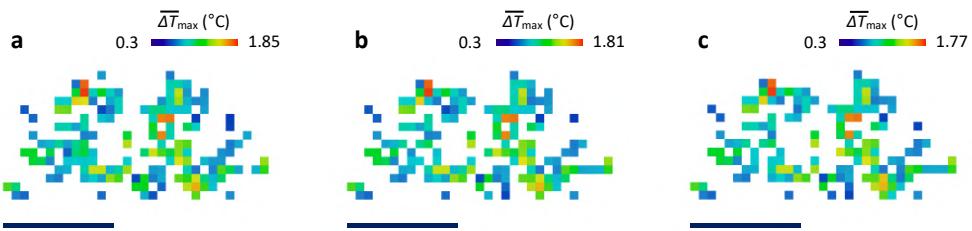

Figure 2.12: Effect of emissivity heterogeneity on treated skin biopsies. **(a)-(c)** Super-resolution photo-thermal images of the same data-set reported in fig. 2.13 upon analysis with constant emissivity of 0.93 (a), 0.95 (b) and 0.97 (c). Scale bar: 1 mm.

been exploited to quantify, at each pixel of the reconstructed images, how much the uncertainty on the emissivity value propagates to the uncertainty on temperature variations. When the very same dataset is analyzed with space-independent emissivities 0.93, 0.95 or 0.97, nearly identical maps of temperature variations are obtained: the uncertainty on the emissivity value in the range 0.93-0.97 does not hamper the thermal reconstruction of the nanoparticles distribution inside the tissue, and allows to estimate the local temperature increments with a maximum uncertainty of 0.1°C (figure 2.12). Based on these considerations, we can also conclude that the assumption of uniform emissivity does not affect sensibly the temperature values measured in murine skin sections in the present work.

2.7.2 Super-resolution imaging results

Upon the emissivity characterization, temperature increments induced by modulated illumination and localized with the two-step Gaussian fitting procedure have been exploited to provide a super-resolution spatial map of the distribution of the nanostructures inside a murine skin biopsy (fig. 2.13a,b). Details as close as $\sim 40\,\mu m$ appear resolved under the adopted imaging conditions, as highlighted by the magnified area in fig. 2.13c (it is to be noted that the 345-μm lateral size of the magnified region is comparable to the thermo-camera theoretical diffraction-limited resolution). The achieved resolution gain appears even larger when the reconstructed images (fig. 2.13b,c) are compared to the conventional thermographic image obtained as the temporal maximum projection over the raw thermo-camera image stack (fig. 2.13d).

A high degree of co-localization has been observed between the temperature variations in the super-resolution image and the lowest-intensity pixels in the corresponding transmitted-light image of the same sample, ascribed to PBNPs (fig. 2.13a-c and fig. 2.14). Results are highly reproducible, as evidenced with the super-resolution thermal image of a second tissue section in figure 2.15, and highlight the specificity of thermal detection in imaging NPs at sub-diffraction resolution in a heterogeneous environment.

This conclusion is reinforced by the results obtained on nanoparticle-untreated samples under identical imaging conditions. In the absence of exogenous nanoparticles, nearly no temperature variation is detected. Only if the ΔT_{min} threshold is lowered from 0.3 °C (as adopted for treated samples in fig. 2.13b) to 0.1 °C (corresponding to the thermal camera sensitivity), a few spurious temperature increments get identified (fig. 2.16). The quantitative comparison of the histograms of the

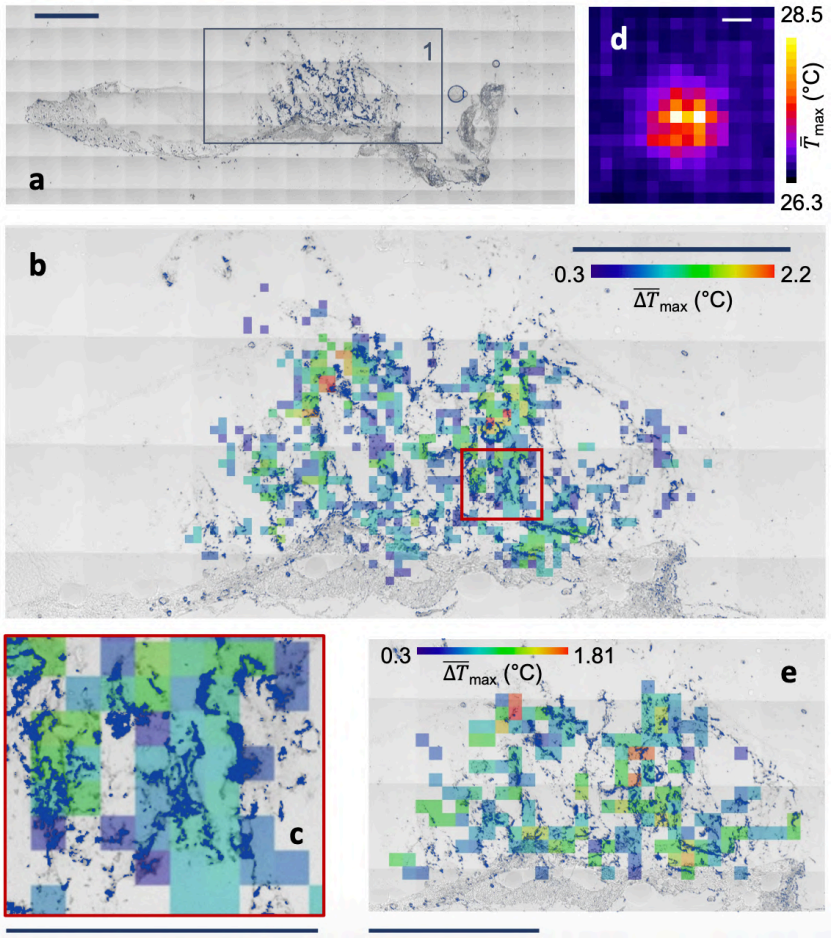

Figure 2.13: **(a)** Transmitted-light tile-scan image of an explanted murine skin biopsy treated with 30-nm PB nanocubes, which are highlighted in navy by an upper threshold on intensity counts. **(b)** Super-resolution image of ROI 1 in (a) ($N_x \times N_y = 100 \times 48$, $\delta x = 37.6\,\mu m$, $\Delta x = 50$, $\Delta y = 1$, $\tau_{on} = 1s$, $P = 15\,mW$, beam $1/e^2$ diameter $22 \pm 1\,\mu m$, $\Delta T_{min} = 0.3\,^{\circ}C$) overlaid to the transmitted-light image. **(c)** Magnification of the red boxed region in (b). **(d)** Temporal maximum projection of the thermo-camera stack employed for (b). **(e)** Same as (b) with doubled pixel size ($N_x \times N_y = 50 \times 24$, $\delta x = 75.3\,\mu m$, $\Delta x = 25$, $\Delta y = 2$), overlaid to the transmitted-light image; only a $2.7 \times 1.6\,mm^2$ ROI is shown for the sake of display. Scale bar: $345\,\mu m$ in (c), $1\,mm$ elsewhere.

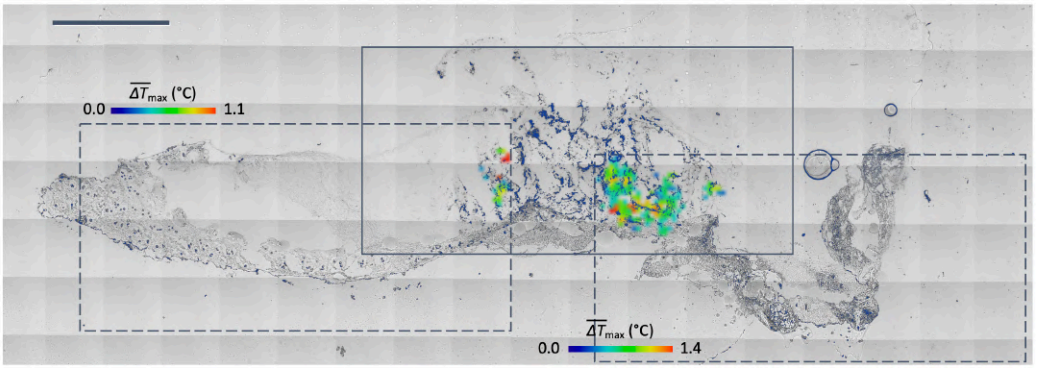

Figure 2.14: Transmitted-light tile-scan image of the explanted murine skin biopsy treated with 30-nm PB nanocubes exploited for the experiments reported in fig. 2.13; nanocubes are highlighted in navy by an upper threshold on the intensity counts. In the dashed ROIs the transmitted-light image is overlaid to the super-resolution photo-thermal images acquired with $N_x \times N_y = 100 \times 48$, $\delta x = 37.6\,\mu m$, $\Delta x = 50$, $\Delta y = 1$, $\tau_{on} = 1s$, $P = 15\,mW$, laser beam $1/e^2$ diameter $22 \pm 1\,\mu m$ ($\Delta T_{min} = 0.3\,°C$). It is worth remarking that no endogenous temperature variation is detected outside the area of nanoparticles injection. Scale bar: 1 mm. The super-resolution image of ROI 1 (boxed region) is reported in fig. 2.13.

$\overline{\Delta T}_{max}$ values in treated and untreated samples allows to unambiguously ascribe the induced heat release in treated samples to injected nanoparticles (fig. 2.16c).

It is worth remarking that $\overline{\Delta T}_{max}$ values as low as 0.3-1.5 °C provide sufficient signal-to-noise ratio to enable the discrimination of NP clusters $\sim 40\,\mu m$ apart (fig. 2.13c). The corresponding laser power $P = 15\,mW$ is sufficiently low not to induce any photo-damage of the imaged structures, as verified through sequential imaging by transmission microscopy before and after photo-thermal data acquisitions (figure 2.17). Finally, at fixed laser power and illumination time, the total acquisition time varies with the scan parameters N_x, N_y and δx. A doubled pixel size allows retaining the major information on the PBNPs distribution inside the treated tissue (fig. 2.13e), while reducing the total acquisition time from 90 to 20 minutes over the $3.7 \times 1.8\,mm^2$ scanned area.

2.8 Results discussion

I conclude by summarizing the main results reported throughout the chapter. The proposed photo-modulated thermal imaging technique allows to overcome

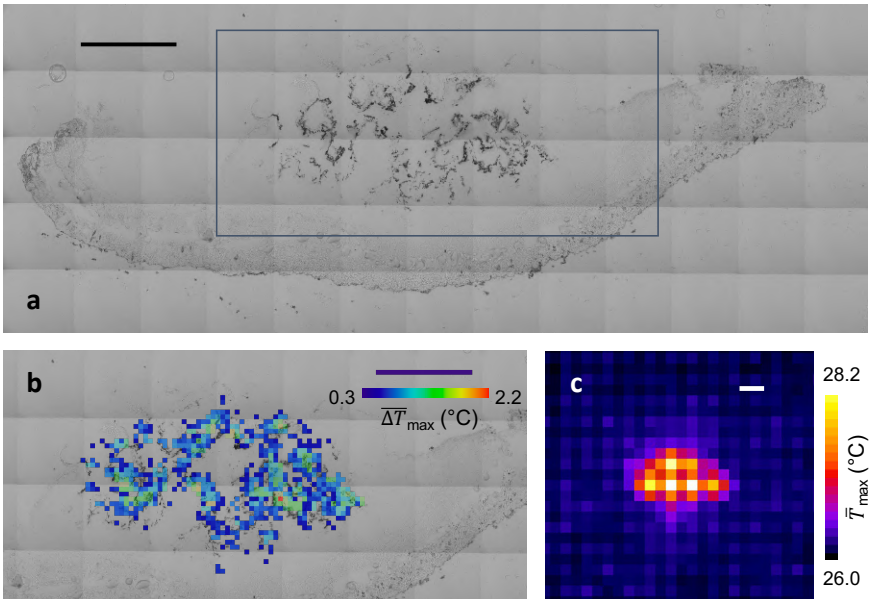

Figure 2.15: **(a)** Transmitted-light tile-scan image of an explanted murine skin biopsy treated with 30-nm PB nanocubes. **(b)** Super-resolution image of ROI in (a) ($N_x \times N_y = 100 \times 48$, $\delta x = 37.6\,\mu m$, $\Delta x = 50$, $\Delta y = 1$, $\tau_{on} = 1s$, $P = 15\,mW$, beam $1/e^2$ diameter $22 \pm 1\,\mu m$, $\Delta T_{min} = 0.3\,^\circ C$) overlaid to the transmitted-light image. **(c)** Temporal maximum projection of the thermo-camera stack employed for (b). Scale bar: 1 mm.

Abbe's resolution limit for the emitted thermal wave on a conventional thermo-camera. The strategy takes advantage of a compact, easily aligned and low-cost (hardware cost $\sim$ 20 k€) benchtop microscope, where a continuous-wave laser beam is raster-scanned and synchronously modulated by a programmable shutter. By relying on the localization of the isolated induced temperature variations, the proposed approach reconstructs the distribution of the absorptive centers in the sample and combines this morphological information with the quantitative measurement of induced pixel-averaged temperature variations.

Sub-diffraction 60-μm resolution has been demonstrated by proof-of-principle experiments, thereby enabling a 4.4-enhancement with respect to the 265-μm diffraction-limited prediction and a 23-time enhancement with respect to the $1400 \pm 200\,\mu m$ effective resolution of our thermal camera in conventional operation. The

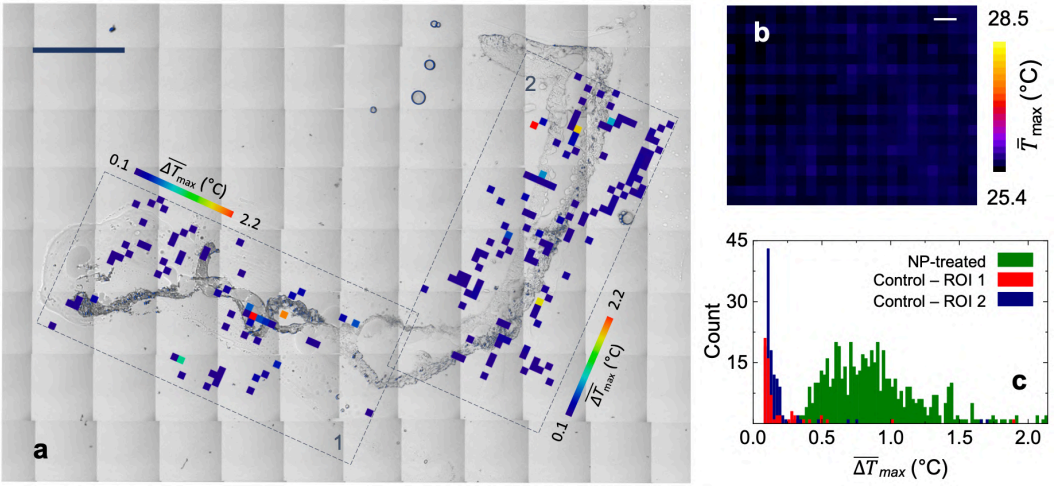

Figure 2.16: (a) Transmitted-light tile-scan image of the untreated explanted murine skin biopsy exploited for the control experiments. In the ROIs 1 and 2 (dashed areas) the transmitted-light image is overlaid to the super-resolution photo-thermal images acquired with parameters $N_x \times N_y = 50 \times 24$, $\delta x = 75.3\,\mu m$, $\Delta x = 25$, $\Delta y = 2$, $\tau_{on} = 1\,s$, $P = 15\,mW$, laser beam $1/e^2$ diameter $22 \pm 1\,\mu m$ ($\Delta T_{min} = 0.1\,^{\circ}C$). **(b)** Temporal maximum projection of the thermo-camera stack employed for (a). **(c)** Histograms of the $\overline{\Delta T}_{max}$ values of the super-resolution images in fig.2.13a (NP-treated, green) and in ROIs 1,2 (control sample, red and blue respectively). Scale bar: 1 mm.

achieved resolution already proves sufficient to accurately map the distribution of light-absorbing nanostructures injected into explanted murine skin biopsies.

I have shown that, with single-spot scanning, a $3.7 \times 1.8\,mm^2$ area can be scanned with 40-μm pixel size in 90 minutes, and this time reduces to 20 minutes with a 75-μm scan pixel size. Extended acquisition times are common to all the super-resolution techniques (e.g., PALM and STORM) that rely on a stochastic molecular switching and readout [58, 59, 67]. A number of bio-relevant applications would benefit from the achievement of super-resolution spatial information while not necessarily requiring transient thermal imaging at high temporal resolution: exemplary applications could be envisioned in the characterization of the distribution of metallic nanoparticles in explanted biopsies for the optimization of photo-thermal therapies, or in the development of active thermography ex-vivo (pre-) clinical protocols in the context of melanoma screening and diagnosis. Whenever beneficial for in-vivo biological applications, our current imaging time could

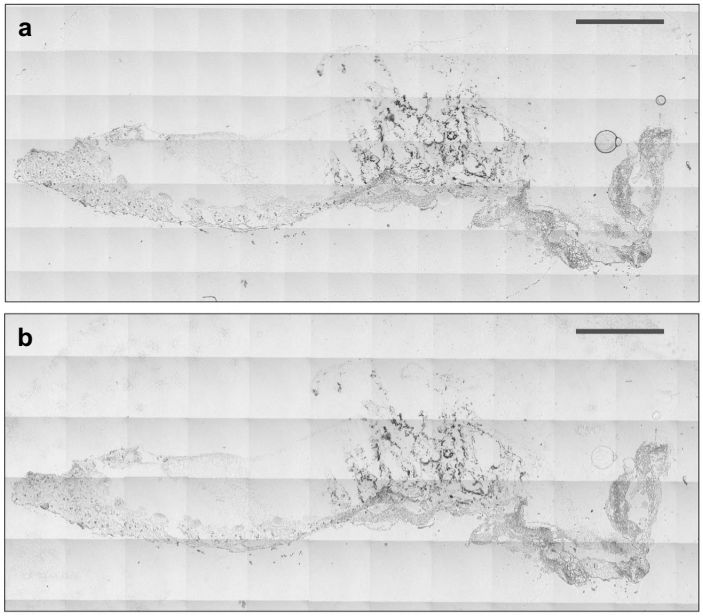

Figure 2.17: Absence of photo-damage on murine skin biopsies. **(a)**,**(b)** Transmitted-light tile-scan images at $\lambda_{exc} = 633\,nm$ of the explanted murine skin biopsy treated with Prussian blue 30-nm nanocubes exploited for super-resolution photo-thermal imaging in fig. 2.13. Images have been collected under identical conditions before **(a)** and right after **(b)** the 90-min data acquisition of fig. 2.13 to demonstrate the absence of sample photo-damage induced by modulated laser light illumination at 15 mW power. Scale bars: 1 mm.

be shortened by multi-spot illumination (via a Spatial Light Modulator) and/or by relaxing the constraint on the observation of individual, isolated temperature peaks. Classes of algorithms allow handling multiple and overlapping signal peaks, based on deep-learning, sequential fitting, sparsity, or maximum-likelihood estimation, and could be adopted to speed up the imaging process [68–70]. Methods developed for ghost imaging [71] could be borrowed as well, especially for those applications (e.g., in cryptography) that require the recognition of an encrypted but known pattern.

By taking advantage of the full analytical description of the space-time dependence of the photo-activated temperature spots imaged on the thermal camera, it should also be possible to combine the reconstruction of super-resolved images

with the quantitative characterization of the sample thermal properties. The possibility of producing 2D maps of (spatially heterogeneous) thermal conductivity values or of the concentration of laser-excited photo-thermal species in the sample will be the object of the next chapters.

Chapter 3

Melanin concentration maps in melanoma biopsies

Surgical excision followed by histopathological examination is the present gold standard for melanoma screening and diagnosis. The color- and texture-based visual inspection of hematoxylin-and-eosin-stained biopsies enables the extraction of relevant morphological, immunohistochemical and topographical features, but fails in providing a non-destructive, space-resolved and quantitative characterization of the melanin content in melanocytic lesions.

Super-resolution photo-activated thermal imaging is presented here as a quantitative method to determine the microscopic distribution and the absolute concentration of melanin pigments in excised melanoma biopsies. The efficient photo-thermal effect primed by melanin absorption of visible raster-scanned laser light is exploited to provide contrast in label-free configuration, and super-resolution far-infrared thermal image acquisition is employed to spatially map melanin pigments at sub-diffraction 40-μm resolution. The conversion of temperature maps into quantitative images of the melanin absolute molar concentration is performed based on finite-element numerical simulations and on the solution of the 3D heat equation in the presence of modulated laser illumination.

Maps of the absolute concentration of melanin pigments are reconstructed on B16 murine melanoma biopsies with 5×10^{-4} M concentration sensitivity. Being readily applicable to human melanoma biopsies in combination with subsequent hematoxylin-and-eosin staining, the proposed approach complements and strengthens traditional histopathology in the characterization of pigmented lesions ex-vivo.

3.1 Motivation

Melanomas are malignant tumors originating from melanocytes in the skin [72–75]. Worldwide annual incidence rates have increased by nearly 50% over the past decade (with ~ 325000 diagnoses of melanoma skin cancer reported worldwide in 2020 [76]), and the extremely aggressive nature of melanomas in metastasizing to distant organs is often associated to unfavorable prognosis [77]. The resulting high mortality, cost and complexity of care pose significant social burdens and demand for the elucidation of the still unclear biological mechanisms underlying melanomas [75] and for the development of effective early-stage diagnostic tools, which are essential to successful treatment [78]. In this context, novel quantitative methods are required to complement and strengthen the robustness of standard histopathological analyses, which still currently rely on a partially subjective visual inspection of immunohistochemistry-stained or hematoxylin-and-eosin (H&E) stained biopsies [79–82].

A major function differentiating normal and malignant melanocytes involves the synthesis of melanin [83]. Although the detailed structure of the final products of melanin biosynthesis is still unknown [84, 85], it is widely recognized that melanogenesis is controlled by nutritional, hormonal and physicochemical factors [86], and that it consists in a multistep transformation of L-tyrosine and L-DOPA (L-3,4-dihydroxyphenylalanine) into melanin biopolymers via oxidoreduction reactions [86–88]. Melanogenesis can be highly deregulated in melanomas [73, 86] and may favor tumor progression due to immunosuppressive, genotoxic and mutagenic properties [83, 86]. The production of pigment has been pointed out as adversely affecting the clinical outcome of metastatic melanomas [86], it attenuates the tumor susceptibility to radio- and chemo-therapy [87] and plays a controversial role in regulating melanoma invasiveness [73, 87]. Melanin provides the necessary protection against ultraviolet radiation and reactive oxygen species in the skin [86], and, at the same time, acts as a marker for melanocyte differentiation [86] serving as potential diagnostic tool [87]. Overall, melanin behaves as a double-edge sword [83, 87] in providing an antioxidant and photoprotective shield while playing a regulatory role in cancer evolution [89]. Such a role has suggested the exploitation of the melanin concentration and spatial distribution as informative biomarkers, to be included in synoptic reports by pathologists, to complement the aforementioned standard histopathological analyses of pigmented skin lesions [80, 83].

Analytical techniques aimed at quantifying melanin in biological samples often rely on destructive chemical degradation and analysis [80], and perform in-vitro

assays on 2D and 3D cell cultures by absorption spectroscopy [89], fluorescence spectrophotometry [90] or high performance liquid chromatography [91] with no spatial resolution [92]. Similarly, Raman spectroscopy [93] and electron paramagnetic resonance spectrometry [94] are less invasive, but still limited to single-point or low-resolution ($\sim 0.5\,\mathrm{mm}$) experiments, thereby being insensitive to the spatial distribution of melanin in the putative melanoma.

To my knowledge, non-destructive and label-free high resolution melanin-based imaging on human and murine melanoma ex-vivo has only been demonstrated by sophisticated optical methods ranging from fluorescence lifetime (FLIM) imaging [95] and confocal reflectance microscopy [96, 97] to pump-and-probe spectroscopy [80, 98] and Photothermal Imaging (PHI) [24, 25, 43, 99]. Both the dominant melanin species (eumelanin and pheomelanin) exhibit a peculiar monotonically decreasing absorption spectrum in the 300-1100 nm range [85, 93] (fig. 3.1), and give rise to fluorescence emission upon near-infrared two-photon excitation [100, 101] or to a highly efficient thermal relaxation upon visible to near infrared light absorption. Despite the moderate melanin fluorescence quantum yield [85], FLIM imaging has allowed differentiating histologically-confirmed benign and malign melanocytic skin lesions by keratinocytes-melanocytes classification [95]. On the other hand, PHI [24, 25, 99] and pump-probe imaging [80, 98] map the spatial distribution of eu- and pheomelanin pigments ex-vivo by taking advantage of non-fluorescent contrast (non-linear refractive index changes and transient absorption, respectively), with the main advantages of optical sectioning capability, high sensitivity and sub-micrometer spatial resolution. Major drawbacks of these approaches consist in a limited size (typically less than $100 \times 100\,\mu\mathrm{m}^2$) of the imaged fields of view, and in the exploitation of costly and complex experimental setups with lock-in detection schemes. Furthermore, no quantification of the melanin absolute concentration is achieved; images are converted at most into relative concentration maps upon calibration on reference melanin solutions [80].

In this chapter, I propose a novel alternative approach aimed at the characterization of the spatial distribution and absolute concentration of melanin pigments in melanoma biopsies by means of super-resolution photo-activated thermal imaging (cf. chapter 2) [60, 102]. The highly efficient photo-thermal effect primed by melanin absorption of focused low-power ($\sim 10\,\mathrm{mW}$) visible laser light provides contrast with no need for labeling. The resulting laser-induced local temperature variations in the sample get detected by far-infrared thermography [1], and the super-resolution image acquisition approach described in chapter 2 is exploited to spatially map melanin pigments at sub-diffraction tunable $\sim 40\,\mu\mathrm{m}$ resolution

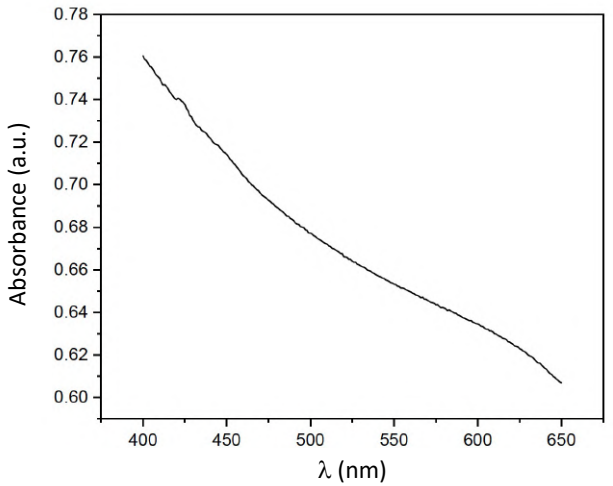

Figure 3.1: Visible absorption spectrum of Sepia eumelanin. With pronounced light absorption and extremely high (0.99) heat-release efficiency, melanin is ideally suited to photo-activated thermography.

over extended (mm^2-cm^2 sized) tissue sections. Super-resolved thermal images are subsequently converted into quantitative maps of the melanin absolute molar concentration based on the results of finite-element simulations and the numerical integration of the 3D heat equation in the presence of modulated laser illumination. A concentration sensitivity of 5×10^{-4} M ($0.09\ \frac{mg}{ml}$) is achieved as a consequence of the employed 33-mW excitation laser power and of the 0.1-K temperature sensitivity of our commercially available thermal camera.

The feasibility of the approach is demonstrated on B16 murine melanoma biopsies [77]. On these samples, sub-diffraction thermography brings into evidence a multipeaked distribution of the amplitudes of laser-induced temperature increments. By the multimodal combination of infrared thermography and fluorescence confocal microscopy, a negative correlation between the thermal signal amplitude and the size of fluorescently stained cell nuclei is further highlighted. Provided the nuclear size and the melanin content may be related to cellular proliferation [103, 104] and maturation stage [80], the results of this chapter pave the way for the future exploitation of super-resolved infrared thermal imaging for the discrimination of different cellular subtypes in excised pigmented skin lesions.

3.2 Materials and methods

3.2.1 Super-resolution photo-thermal imaging setup

Super-resolution thermal imaging is performed on a custom-made benchtop optical setup, which is described in section 2.4.1. For what concerns this chapter, the absorption in the sample is primed by an Argon laser beam (514-nm wavelength, Spectra Physics, CA, USA) with $1/e^2$ spot diameter $\omega = 30\,\mu m$ and typical 30-mW power on the sample plane. The detection of thermal radiation is performed in the 7.5-13 μm spectral range by an uncooled microbolometer-based thermal camera (FLIR T650sc, FLIR Systems Inc., OR, USA) with 30-Hz frame rate. The detector provides 640×480 images, with 420 μm pixel size on the sample plane. The thermo-camera corrects for the atmospheric attenuation and the sample reflection of the thermal radiation emitted by the surroundings provided that the sample distance from the camera front lens, the sample emissivity ε, and the relative humidity and temperature of the atmosphere are inserted in the camera software (cf. section 1.1.3). A 50% humidity has been assumed for all the experiments of the present work, whereas the sample distance ($\sim 40\,cm$) and the ambient temperature have been measured for each imaging experiment. An emissivity $\varepsilon = 0.98$ has been employed as reported for skin in the literature [105]. The analysis of raw thermal camera frames has been performed by the two-dimensional non-linear Gaussian fit of each detected temperature peak at the end of the corresponding laser illumination event lasting τ_{on}; each fit provides the peak center coordinates and the amplitude $\overline{\Delta T}_{max}$ (as described in section 2.3).

3.2.2 Transmission and fluorescence microscopy setup

A Leica TCS SP5 STED-CW scanning confocal microscope (Leica Microsystems, D) has been employed for transmitted-light and fluorescence imaging of melanoma biopsies. The laser source consists in a 633-nm He-Ne beam or a 514-nm Argon beam (power $P \sim 10\,\mu W$ on the sample plane), which is focused on the sample by a 20x 0.5-NA air objective (HCX PL Fluotar, Leica Microsystems, D). Transmitted-light images have been acquired on both stained and unstained melanoma biopsies by detecting the transmitted laser light signal with a non-spectral dedicated photo-multiplier tube, with no confocal pinhole along the detection optical path. For DRAQ5 stained biopsies, the dye fluorescence signal has been collected by a PMT (Photo-Multiplier Tube) in the 660-700nm band. A 400-Hz raster scan frequency

per line has been adopted, and millimeter-sized sample regions have been imaged using a tile-scan (mosaic) acquisition mode.

3.2.3 B16 biopsies

For the preparation of murine B16 melanoma biopsies, the murine tumor cell line B16 has been cultured in IMDM-10 complete medium (IMDM, 10% heat-inactivated FBS (EuroClone, I), 2 mM l-glutamine, 100 U/ml penicillin, 100 µg/ml streptomycin). Cells at 70% confluence have been collected for injection of a tumorigenic dose of 2×10^6 cells in the deep derma of the left flank of C57bl/6 mice at 7-12 weeks of age. At day 7 or day 14, mice have been euthanized and the tumor has been collected. Explanted tissue sections have been cut on a cryostat in 20-µm sections upon embedding in OCT freezing medium (Biooptica, I) and adhered to glass slides (Superfrost Plus, Thermo Fisher Scientific, MA, USA) for super-resolution photo-thermal imaging. When necessary, fluorescence staining with the DRAQ5 nucleic-acid stain has been performed after completion of photo-thermal data acquisition on the biopsies. For hematoxylin-and-eosin staining the skin sections have been stained with Meyer's hematoxylin solution for 8 minutes and then washed in warm running tap water for 5 minutes. Sections have been stained with Eosin Y solution for 1 minute, washed in warm running water for 5 minutes, rinsed in distilled water and then dehydrated through passages in 95% and absolute alcohol. Slides have been cleared in xylene and mounted with Eukitt. H&E images have been acquired with a NanoZoomer scanner (Hamamatsu, JP). All the experiments have been performed under protocols approved by the Institutional Animal Care and Use Committee of the University of Milano-Bicocca and the Italian Ministry of Health.

3.2.4 Nuclei segmentation

The automatic segmentation of cellular nuclei from fluorescence confocal microscopy images has been implemented in a custom-written macro in the freeware software FiJi [106]. The macro reads the raw fluorescence image in .tif format and routinely performs the nuclei segmentation on adjacent Regions of Interest (ROIs) of adjustable size (typically, 3000×3000 pixels with $\sim$ 250-nm pixel size). For each ROI, a Gaussian blur filter with 1.5-pixel standard deviation is applied first; then the ROI image gets converted into a binary file upon selection of an intensity threshold and separation of individual nuclei by the FiJi built-in Water-

shed algorithm. The nuclei segmentation is performed based on the FiJi "Analyze particle" tool with acceptable identified nucleus radius in the 15-300 μm^2 range, with acceptable nucleus circularity in the 0.2-1 range, and by excluding all nuclei located on the ROIs edge. Results of the segmentation procedure are saved in a .txt file as a list of the area and center coordinates of each nucleus, so that a final image with chosen pixel size can be reconstructed and color-coded based on the average area of all the nuclei identified in each pixel.

3.2.5 Data analysis software

Photo-thermal imaging raw data have been acquired with the thermo-camera software (FLIR Tools+, FLIR Systems Inc., OR, USA), exported in .csv file format and entirely processed by a custom-written Python code. A custom Python code has also been employed for the numerical integration of eq. 1.3.16 and eq. 3.4.1 for fig. 3.9. Statistical significance tests in fig. 3.10 have been performed by GraphPad Prism (GraphPad Software, CA, USA).

Finite-element simulations employed for fig. 3.7 and fig. 3.8 have been performed by the COMSOL Multiphysics software (COMSOL AB, S). k and D values for both skin and Corning glass have been derived from the COMSOL Material Library. The spatial average of temperature profiles over a square pixel size has been implemented in the simulation program (pixel size $l = 420\,\mu m$). Convective and radiative heat losses have been implemented with emissivity $\varepsilon = 0.9$ and a convective heat transfer coefficient $h = 10\,W m^{-1} K^{-1}$.

3.3 Spatial distribution of melanin pigments

Super-resolution photo-thermal imaging is adopted here to image and quantify melanin pigments at sub-diffraction 40-μm resolution over mm^2-cm^2-sized excised murine melanoma biopsies. I have taken advantage of biopsies of the B16 murine melanoma model excised 14 days upon cells inoculation in the mouse flank (cf. section 3.2). The presence of melanin, which is responsible for evident pigmentation of the excised tissue sections, has been confirmed by Fluorescence Lifetime Imaging (FLIM). Excitation at 800 nm and detection of the two-photon excited endogenous fluorescence in the 600/40 nm band allows quantifying a double-component fluorescence lifetime, equal to $\tau_1 = (0.51 \pm 0.05)\,ns$ and $\tau_2 = (2.21 \pm 0.05)\,ns$ with 21% and 79% relative fractions, respectively. Recovered lifetime values agree with those

reported in the literature [95] for melanin-containing melanocytes and keratinocytes and confirm the abundance of melanin pigments in the tissue.

For super-resolution photo-thermal imaging experiments, light-absorption and the photo-thermal effect have been primed at the 514-nm wavelength of an Argon beam. With a typical excitation laser power on the sample plane $P = 33$ mW, and a laser activation time $\tau_{on} = 200$ ms per excitation event, retrieved temperature increments lie in the $\overline{\Delta T}_{max} = 0\text{-}10$ K range (fig. 3.2a).

As revealed in fig. 3.2a with the super-resolution photo-thermal image of a typical tissue section, the spatial distribution and the amplitude of laser-induced temperature increments are highly heterogeneous, with only portions of the imaged biopsy effectively contributing to a non-zero detected thermal signal. The visual comparison of the super-resolved thermal map (fig. 3.2a) with the corresponding conventional transmitted-light image (fig. 3.2e) and with the image acquired upon hematoxylin-and-eosin staining of the same biopsy (fig. 3.2b) confirms accurate reconstruction of the sample morphology. When super-resolved thermal imaging is extended to the whole excised biopsy (fig. 3.3), the superposition of the thermal map to the corresponding transmitted-light image further confirms that the sample morphology is properly reconstructed. It is also worth remarking that with the typical measured temperature increments ($\overline{\Delta T}_{max} = 0\text{-}10$ K) no photo-damage is induced on the sample. This has been verified by sequential transmitted-light imaging before and after photo-thermal data acquisitions, and a further confirmation is provided by the possibility of performing hematoxylin-and-eosin staining of the very same tissue section right after the completion of photo-thermal data acquisition (fig. 3.2a-b).

Hematoxylin-and-eosin staining results in cellular nuclei being stained blue and the cells cytoplasm and the extracellular matrix being stained pink [79]; melanin, which is not specifically stained, appears in H&E-stained B16 melanoma as optically contrasted brown-black eumelanosome-like granules [79, 87, 91]. A close-up inspection of magnified regions of interest in the H&E image (fig. 3.2c,d) highlights that melanin is prominently present in those regions of the biopsy where a pronounced photo-thermal effect has been detected (fig. 3.2a,c). By contrast, clearly less abundant melanin pigments are observed in those areas where no heat release above the 0.1-K thermal camera sensitivity has taken place upon laser irradiation (fig. 3.2a,d). Therefore, while not enabling a straightforward routine quantification of the melanin content, the hematoxylin-and-eosin image of the biopsy confirms that the detected thermal signal can be ascribed to the photo-thermal activity of melanin. Such a conclusion is reinforced by the nearly absent photo-thermal signal

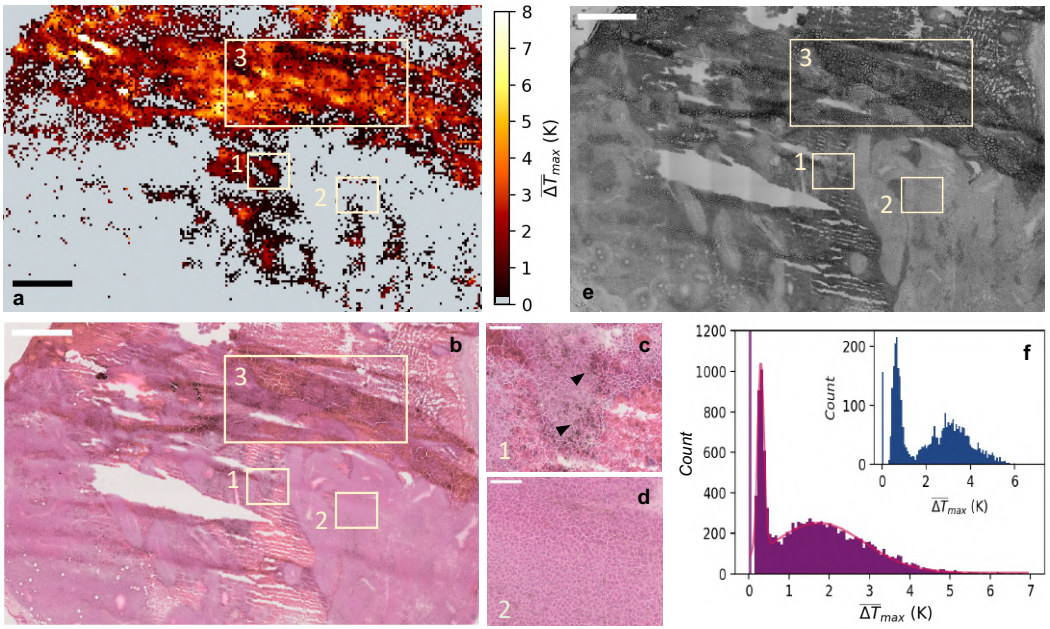

Figure 3.2: (a) Super-resolution label-free photo-thermal image of a B16 murine melanoma biopsy. Acquisition parameters: $\lambda_{exc} = 514$ nm, $P = 33$ mW, $\tau_{on} = 200$ ms, laser $1/e^2$ radius $\omega = (28 \pm 1)$ µm, pixel size $\delta x = 37.8$ µm. Notice that grey color codes for pixels where no thermal signal above the thermal camera sensitivity (0.1 K) has been detected. **(b)** H&E image of the same biopsy imaged in (a). H&E staining has been performed upon completion of photo-thermal imaging. **(c,d)** Magnification of ROIs 1 and 2 from the H&E image in (b). Black arrows in (c) point to melanin pigments appearing brownish in color. **(e)** Transmitted-light image of the same biopsy imaged in (a) and (b). Scale bar: 1000 µm in (a,b,e), 100 µm in (c,d). **(f)** Histogram of the amplitude of laser-primed temperature increments detected in (a), overlaid to the best fit to a two-component Gaussian distribution. Best-fit peaks correspond to $\Delta T_{max} = (0.30 \pm 0.08)$ K and $\Delta T_{max} = (1.7 \pm 1.1)$ K. The y-axis has been limited to the 0-1200 count range for the sake of display. Inset: histogram of the amplitude of laser-primed temperature increments detected in ROI 3 of panel (a) at increased $\tau_{on} = 600$ ms (the corresponding super-resolved thermal image is reported in figure 3.5).

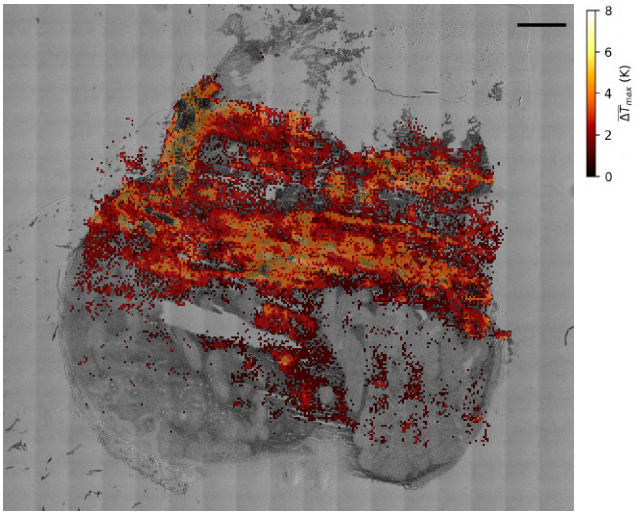

Figure 3.3: Super-resolution thermal image of the whole B16 murine melanoma biopsy employed for fig. 3.2a, overlaid to the transmitted-light image of the same section. Scale bar=1000 μm. Acquisition parameters for thermal imaging are the same of fig. 3.2a.

exceeding the thermal camera sensitivity in less pigmented B16 melanoma biopsies excised 7 days after cells injection (fig. 3.4).

The histogram of the amplitudes of laser-induced temperature increments extracted from fig. 3.2a reveals a multipeaked distribution (fig. 3.2f). 20% of the imaged area appears associated to $\overline{\Delta T}_{max}$ values lying above the 0.1-K thermal camera sensitivity. Above 0.1K, temperature increments identify two clearly separated peaks, with the lower- and higher-amplitude peaks centered at $\overline{\Delta T}_{max} = (0.30 \pm 0.08)$ K and $\overline{\Delta T}_{max} = (1.7 \pm 1.1)$ K, respectively (mean $\pm$ standard deviation). Super-resolved thermal imaging on a selected region of interest of the same biopsy at increased laser activation time $\tau_{on} = 600$ ms retrieves systematically higher temperature increments, as expected, but still preserves the double-peaked distribution of the detected thermal signal above the camera sensitivity (fig. 3.2f and fig. 3.5). We can therefore exclude that the 0.3-K temperature peak is a spurious result of erroneous Gaussian surface fits performed on the thermal-camera frames at moderately low signal-to-noise ratio. The reproducibility of the results is also highlighted by the superposition of the histograms of laser-induced temperature increments recovered on tissue sections excised from different tumors and im-

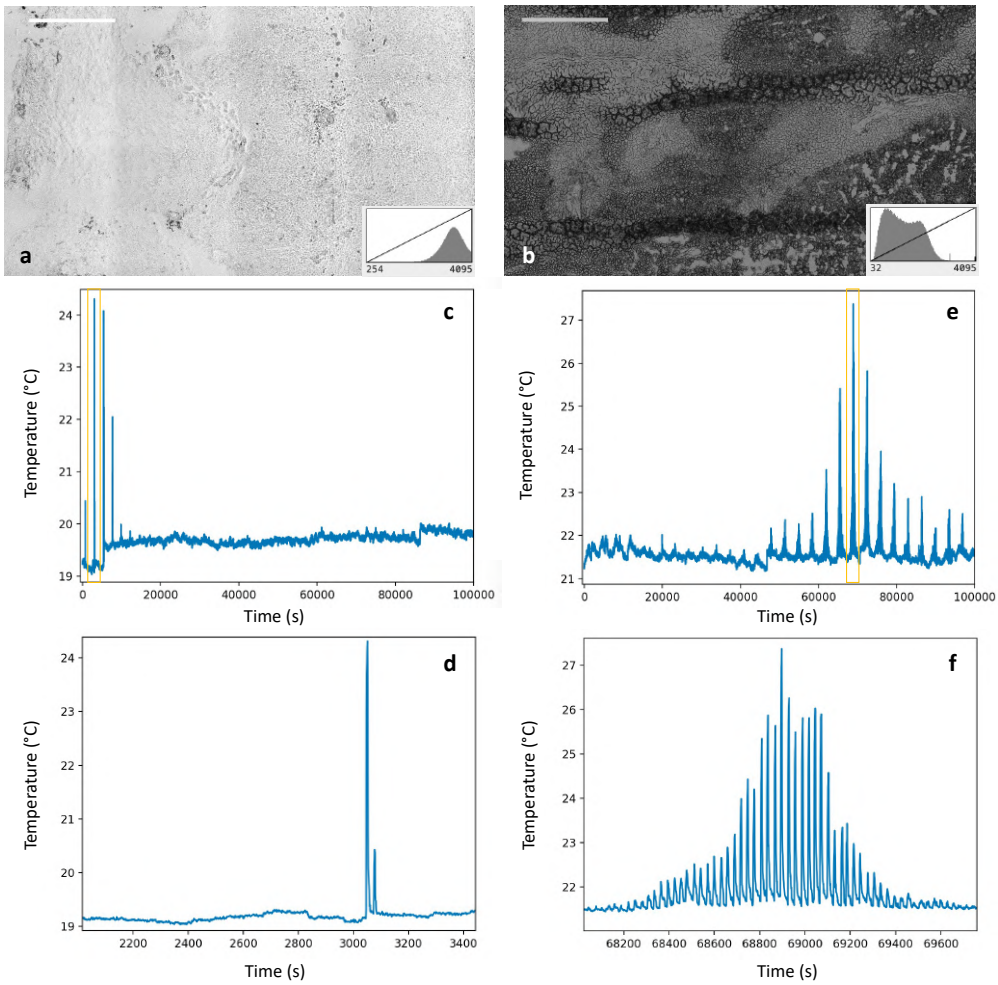

Figure 3.4: **(a,b)** Transmitted-light images of murine melanoma biopsies excised 7 (a) and 14 (b) days upon B16 cells inoculation in the mouse flank. Higher transmitted-light intensities in (a) are associated to a significantly lower pigmentation of the 7-day biopsy relatively to the 14-day one. Insets: histograms of intensity counts in arbitrary units. **(c,e)** Temperature time-trace extracted from an exemplary thermal camera pixel during super-resolution photo-thermal imaging on the tissue section shown in (a) and (b), respectively. **(d,f)** Magnification of the yellow-boxed regions from (c) and (e), respectively. Each peak in the temperature time traces identifies a laser-primed heat-release event in the sample: panels (c-f) highlight therefore a nearly-absent photo-thermal signal in the 7-day biopsy and a much more abundant photo-thermal signal in the more pigmented 14-day biopsy.

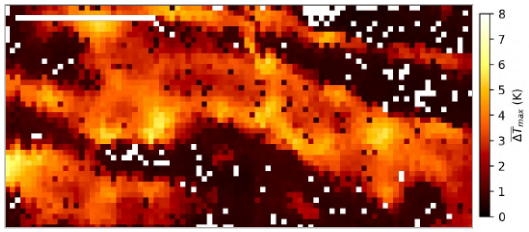

Figure 3.5: Super-resolved photo-thermal image of the region identified as ROI 3 in figure 3.2a at increased laser activation time $\tau_{on} = 600$ ms. Acquisition parameters: $\lambda_{exc} = 514$ nm, $P = 33$ mW, laser $1/e^2$ radius $\omega = (28 \pm 1)$ µm, pixel size $\delta x = 37.8$ µm as in figure 3.2a. Scale bar: 1 mm. The histogram of the $\overline{\Delta T}_{max}$ amplitudes is reported in the inset of figure 3.2f.

aged under identical conditions (fig. 3.6). The multipeaked signal distribution is preserved, with similar center values and variable relative fractions for the three temperature peaks.

Based on the results of figures 3.2- 3.3, in the following (i) I demonstrate the conversion of temperature-based images into quantitative maps of the absolute concentration of melanin pigments, and (ii) I combine infrared thermography and fluorescence confocal microscopy in a multimodal approach aimed at elucidating the presence of different cellular populations in the tissue as suggested by the thermal-signal distributions of fig. 3.2f and fig. 3.6.

3.4 Super-resolution images of the absolute molar concentration of melanin pigments

The amplitude $\overline{\Delta T}_{max}$ of the temperature increment resulting from a laser-induced photo-thermal effect and sensed by the pixelated detector (focal plane array) of a far-infrared thermal camera is the result of the convolution of the camera point-spread-function with the temperature profile, followed by the spatial average of the convoluted temperature distribution over the extended camera pixel size (cf. section 1.3.1). With the same notation of chapter 1, I denote here with $T(x, y, 0, \tau_{on})$ the temperature distribution on the sample front surface ($z = 0$) at time-point $t = \tau_{on}$, primed by an excitation laser beam centered at $(x, y, z) = (0, 0, 0)$. I denote with $\overline{\Delta T}_{max}$ instead the amplitude of the temperature distribution resulting from the convolution of $T(x, y, 0, \tau_{on})$ with the camera PSF and from its spatial average

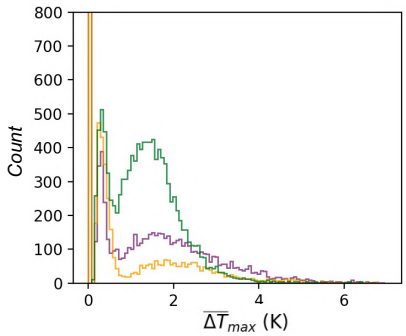

Figure 3.6: Reproducibility of the histogram of the amplitude of laser-primed temperature increments detected in 3 biopsies excised from 3 different tumors under the same imaging conditions of fig. 3.2a. Histograms have been derived from equal-sized ROIs ($5.2\times4.1\ mm^2$).

over the square camera pixel of side l; as in chapter 2, $\overline{\Delta T}_{max}$ is evaluated at time-point $t = \tau_{on}$.

The expressions for $T(x, y, 0, \tau_{on})$ and $\overline{\Delta T}_{max}$ have to be explicitly derived in the presence of a focused Gaussian laser beam (having power P and $1/e^2$ beam waist ω on the sample plane) impinging on a two-layer material composed of a 1-mm thick glass slide and a 20-μm thick tissue section. However, the reduced thickness of the tissue biopsy relatively to the much larger thickness of the underlying glass substrate suggests that the contribution of the glass slab might dominate in the overall heat transfer: in this case, a single-layer approximation could simplify the theoretical modeling. Aiming at verifying if a similar approximation holds, two finite element simulations have been implemented in the Comsol Multiphysics software. The temporal evolution of the amplitude of the temperature increment primed by a laser pulse with beam waist $\omega = 30\,\mu m$ and duration $\tau_{on} = 200\,ms$ has been simulated on (i) a 1020-μm thick glass slide (thermal conductivity $k = 0.9\,Wm^{-1}K^{-1}$, thermal diffusivity $D = 5.02 \times 10^{-7}\,m^2s^{-1}$) and (ii) a two-layer material composed of a 20-μm thick tissue section (skin tissue, $k = 0.37\,Wm^{-1}K^{-1}$, $D = 9.84 \times 10^{-8}\,m^2s^{-1}$) overlaid to a 1-mm thick glass slide. Results, reported in fig. 3.7, reveal that, when compared to the case of a single-layer glass substrate at identical absorbed laser power, the lower thermal conductivity of the 20-μm tissue layer increases the amplitude of the laser-primed temperature increment (fig. 3.7a); the temporal kinetics of temperature evolution is unchanged instead (fig. 3.7b). Therefore, an identical temperature change and temporal evolution can in principle

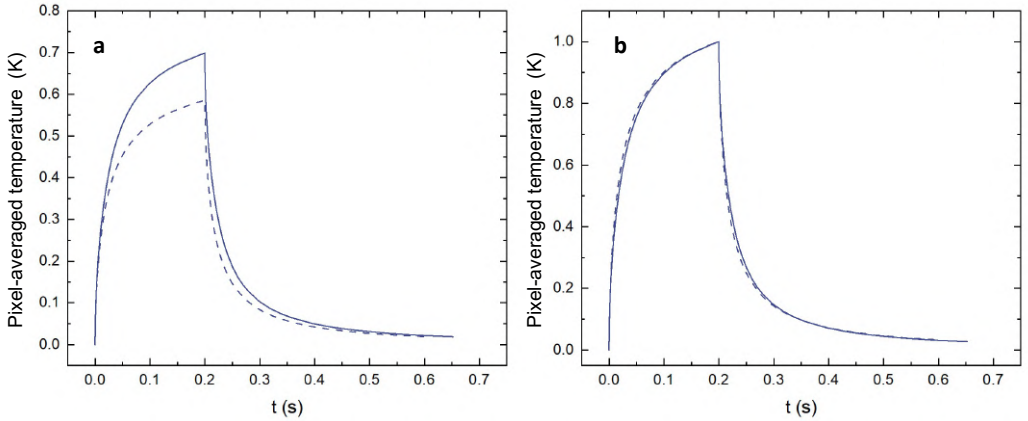

Figure 3.7: (a) Dashed blue line: temporal evolution of the amplitude of the temperature increment primed by a laser pulse with beam waist $\omega = 30\,\mu m$ and duration $\tau_{on} = 200\,ms$ on a 1020-μm thick glass slide (thermal conductivity $k = 0.9\,Wm^{-1}K^{-1}$, thermal diffusivity $D = 5.02 \times 10^{-7}\,m^2s^{-1}$; 0.5-$mW$ absorbed laser power). Continuous blue line: temporal evolution of the amplitude of the temperature increment primed by a laser pulse with beam waist $\omega = 30\,\mu m$ and duration $\tau_{on} = 200\,ms$ on a two-layer material composed of a 20-μm thick tissue section (skin tissue, $k = 0.37\,Wm^{-1}K^{-1}$, $D = 9.84 \times 10^{-8}\,m^2s^{-1}$; 0.5-$mW$ absorbed laser power) overlaid to a 1-mm thick glass slide. **(b)** Normalization to unity of the profiles in (a).

be obtained on the single-layer 1020-μm thick glass sample and on the double-layer glass+tissue sample provided the glass slide is subject to an increased effective laser power P_{eff}. Given the linear proportionality of the amplitude of temperature peaks to the excitation laser power, from the ratio of the temperature profiles in fig. 3.7a we retrieve $P_{eff} = 1.2 \cdot P$, where P denotes the laser power employed in the presence of the skin tissue section.

Experimentally, it is therefore reasonable to assume that the overall heat transfer propagation in the imaged biopsies is dominated by the contribution of the underlying glass substrate (as intuitive based on the difference between the 1-mm and the 20-μm thicknesses), while light absorption and heat release are only determined by the absorbance $\mathcal{A}$ of the 20-μm tissue layer (no light absorption and heat release are observed for a single-layer 1-mm thick glass slide at the adopted incident 33-mW laser power). Hereafter, I model therefore each biopsy sample as a 1020-μm thick glass slide subject to a laser power P_{eff}.

Provided the negligible contribution of both convective and radiative losses (fig.

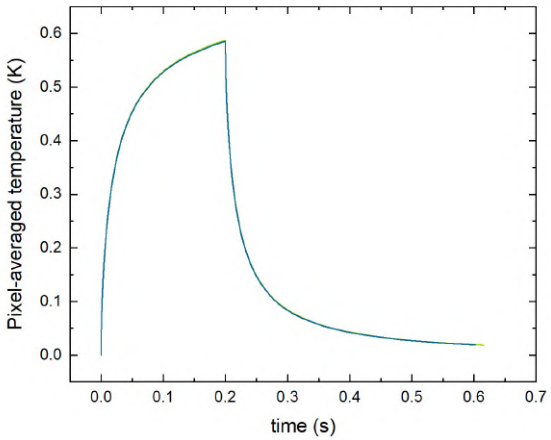

Figure 3.8: Comparison of the temporal profiles of the amplitude of the temperature increment primed by a laser pulse with beam waist $\omega = 30\,\mu m$ and duration $\tau_{on} = 200\,ms$ on a 1020-μm thick glass slide ($k = 0.9\,Wm^{-1}K^{-1}$, $D = 5.02 \times 10^{-7}\,m^2s^{-1}$, 0.5-$mW$ absorbed laser power) in the presence of radiative and convective heat losses (blue; emissivity $\varepsilon = 0.9$ and convective heat transfer coefficient $h = 10\,Wm^{-1}K^{-1}$), and in the absence of heat losses (green).

3.8), as anticipated in chapter 1 [17, 102] the laser-primed temperature distribution $T(x, y, z, t)$ on such a single-layer thermally thick specimen can be expressed as

$$T(x,y,z,t) \approx P_{eff}(1 - e^{-2.303EC\ell})\phi_{pt}\frac{2D}{\pi k}\cdot \cdot \int_{t_0}^{t} dt_1 \frac{1}{\omega^2 + 8Dt_1} exp\left(-\frac{2(x^2+y^2)}{\omega^2+8Dt_1}\right)\frac{1}{\sqrt{\pi Dt_1}} exp\left(-\frac{z^2}{4Dt_1}\right) + T_m \quad (3.4.1)$$

Based on eq. 1.2.15, eq. 3.4.1 has been modified to account for the transmittance properties of the sample: by definition of absorbance, the absorbed laser power has been expressed as $P_{eff}(1 - e^{-2.303EC\ell})$, where $\ell = 20\,\mu m$, E is the molar extinction coefficient of light-absorbing and heat-releasing entities, and C is their molar concentration within the laser-illuminated voxel defined by the thickness ℓ and the excitation laser beam waist. P_{eff} equals $P_{eff} = 1.2 \cdot P$ as quantified in fig. 3.7, and the contribution of laser-light reflection by the pigmented tissue is assumed negligible in comparison with absorption [107]. ϕ_{pt} corresponds to the heat-release efficiency of the photo-thermal sample. In the integral, $t_0 = 0$ if $t < \tau_{on}$ and

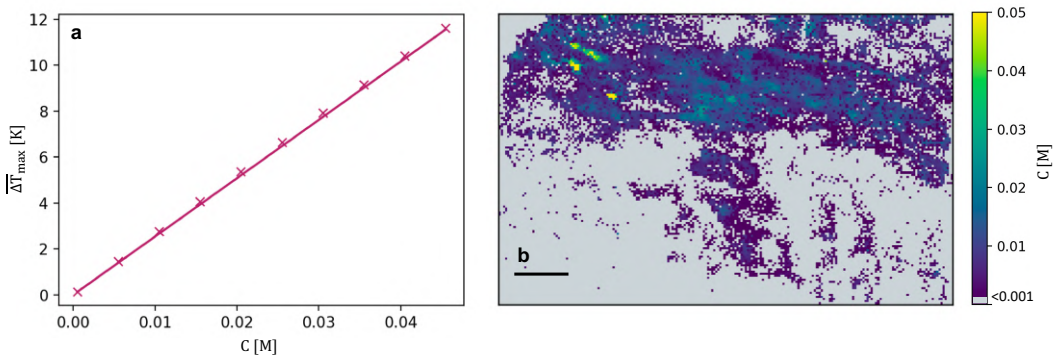

Figure 3.9: (a) $\overline{\Delta T}_{max}$ dependence on the absolute molar concentration C of light-absorbing and heat-releasing entities simulated based on eq. 1.3.16 and eq. 3.4.1 for a single-layer 1020-μm thick slab with $k = 0.9\ Wm^{-1}K^{-1}$, $D = 5.02 \times 10^{-7}\ m^2s^{-1}$, $\omega = 30\ \mu m$, $P_{eff} = 39.6\ mW$, $\tau_{on} = 0.2\ s$ and $l = 420\ \mu m$. The solid line is the best linear fit to $\overline{\Delta T}_{max} = mC$ with zero intercept and $m = 254\ KM^{-1}$. **(b)** Super-resolution image of the absolute molar concentration of melanin pigments in the B16 melanoma biopsy employed for figure 3.2a. The image is derived from figure 3.2a by the pixel-wise conversion $C = \overline{\Delta T}_{max}/m$. Scale bar: 1000 μm.

$t_0 = t - \tau_{on}$ if $t \geq \tau_{on}$. By numerically integrating $T(x, y, 0, \tau_{on})$ over a square region of size l (equation 3.4.1 into eq. 1.3.16), the theoretical dependence of $\overline{\Delta T}_{max}$ on the concentration C can be evaluated.

Results are reported in figure 3.9a for melanin pigments under the typical experimental conditions adopted here for super-resolution thermography. In the 0-10 K range of our experimentally measured temperature increments, a linear relation well approximates the dependence of $\overline{\Delta T}_{max}$ on the concentration C. This allows establishing a direct proportionality of the type $\overline{\Delta T}_{max} = mC$ between the experimental amplitudes $\overline{\Delta T}_{max}$ and the concentration of photo-thermal laser-excited pigments in the tissue. In the present case ($l = 420\ \mu m$, $P_{eff} = 39.6$ mW, $\tau_{on} = 200$ ms, $\omega = 30\ \mu m$, $\ell = 20\ \mu m$, $k = 0.9\ Wm^{-1}K^{-1}$, $D = 5.02 \times 10^{-7} m^2s^{-1}$, $\phi_{pt} = 0.99$ [108] and $\varepsilon = 1500\ M^{-1}cm^{-1}$ for melanin at the 514-nm excitation wavelength [109]), the slope m equals $m = 254\ KM^{-1}$. Super-resolution photo-thermal images of melanoma biopsies can be therefore converted into quantitative maps of the absolute molar concentration of melanin pigments by a simple pixelwise computation of the concentration according to $C = \overline{\Delta T}_{max}/m$. The concentration limit of detection for a 33-mW incident excitation laser power is determined

by the 0.1-K temperature sensitivity of our thermal camera and by the temperature/concentration slope $m = 254\ KM^{-1}$ and equals $5 \times 10^{-4}\ M$, corresponding to a $0.09\ \frac{mg}{ml}$ concentration based on the eumelanin monomer molar mass [110] $171\ gmol^{-1}$. Such a concentration sensitivity could be further improved by incrementing the excitation laser power up to the maximum value allowed by the absence of photo-induced sample damage.

The super-resolved thermal image of figure 3.2a is converted into a concentration image in figure 3.9b. The retrieved melanin concentration up to $0.05\ M$ ($9\ \frac{mg}{ml}$) is comparable with reference values reported in the literature for human melanoma and human retinal pigment epithelium ex-vivo [101, 111]. The reproducibility in the magnitude of the detected thermal signal (fig. 3.6) confirms the feasibility of a quantitative comparison of the melanin concentration maps extracted from different melanoma biopsies imaged under identical conditions.

3.5 Correlation between the photo-thermal signal amplitude and the size of cell nuclei

The histograms of the amplitudes of laser-primed temperature increments (fig. 3.6) detected on murine melanoma biopsies (or equivalently, the corresponding histograms of the melanin concentration) reveal a multipeaked distribution, suggesting that two major populations, differing in the melanin content, contribute to the collected thermal signal. A third cellular population can be identified as the one corresponding to all areas of the biopsy where no thermal signal exceeding the camera sensitivity has been detected. Aiming at further elucidating the presence of different cell populations in the imaged biopsies, a multimodal combination of super-resolved thermography and fluorescence confocal microscopy has been adopted. Following infrared thermography experiments, the same B16 murine melanoma biopsies have been fluorescently stained with the DRAQ5 dye, that specifically stains DNA with a broad fluorescence emission above $665\ nm$. The exemplary confocal fluorescence image reported in figure 3.10a highlights a pronounced heterogeneity in the dimensions of cellular nuclei. Quantitatively, an automated Watershed segmentation of individual nuclei and the measurement of the corresponding occupied area (figure 3.10d-e) demonstrates significantly different nuclear sizes (figure 3.10f) in the two regions of interest of figure 3.10b,c. Extension of the segmentation procedure to the entire $\sim 2.5\ mm^2$ region of figure 3.10a provides a broad overall distribution for the nuclear size (figure 3.10f), with a two-

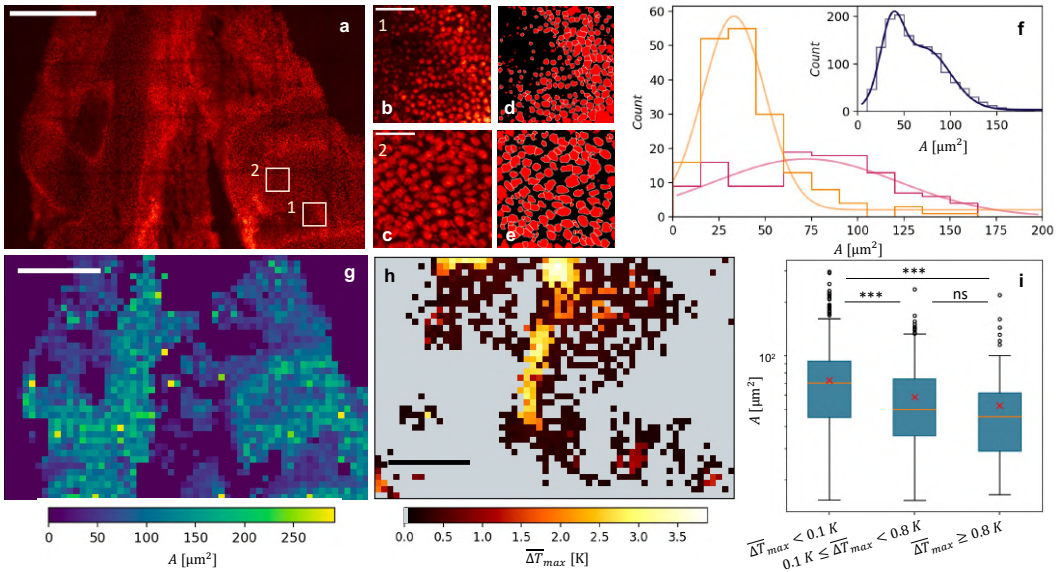

Figure 3.10: Nuclei segmentation on a B16 melanoma biopsy. **(a)** Confocal fluorescence image ($\lambda_{exc} = 633$ nm, $\lambda_{em} = 660 - 700$ nm) of a region of interest of a B16 murine melanoma biopsy (maximum z-projection over 9 planes sampled at 2.5-μm z-step). Cell nuclei are stained with the DRAQ5 dye. **(b,c)** Magnification of ROIs 1 and 2 from panel (a). **(d,e)** Results of the automated nuclei segmentation on panels (b,c), with borders of segmented nuclei highlighted in white. **(f)** Histograms of the areas of segmented nuclei from (d) and (e) (orange and pink, respectively). Best Gaussian fits provide average nuclear sizes (33 ± 17) μm^2 and (72 ± 50) μm^2. Inset: histogram of the areas of segmented nuclei from panel (a), overlaid to the best two-component Gaussian fit centered at $A_1 = (37 \pm 12)$ μm^2 and $A_2 = (72 \pm 27)$ μm^2. **(g)** Nuclear size map recovered from the nuclei segmentation on panel (a). Dark blue areas correspond to regions where nuclei are not sufficiently contrasted for the segmentation procedure. **(h)** Super-resolution thermal image acquired on the same biopsy (same region of panel (a)) prior to fluorescence staining. The 37.8-μm pixel size is the same for (g) and (h). Scale bars: 500 μm in (a), (g), (h), 50 μm in (b)-(e). **(i)** Box chart of average nuclear sizes retrieved in pixels where a laser-primed temperature increment $\overline{\Delta T}_{max}$ has been measured below 0.1 K (left, group A), above 0.8 K (right, group C) and within the 0.1-0.8 K range (middle, group B) (black circles: outliers, red cross: mean, orange line: median). Data have been tested for statistical significance with the Brown-Forsythe and Welch ANOVA test (***: $p < 0.001$, ns: $p > 0.12$).

component Gaussian fit identifying two distribution centers at $A_1 = (37 \pm 12)\ \mu m^2$ and $A_2 = (72 \pm 27)\ \mu m^2$.

Based on nuclei segmentation, a nuclear-size image can be reconstructed with the color code assigned by the average nuclear size retrieved in each pixel (section 3.2). If the same 37.8-μm pixel size of super-resolved photo-thermal images is adopted, the nuclear size map (figure 3.10g) can be correlated with the same region of interest of the corresponding thermal image (figure 3.10h). Indeed, the box-chart analysis of figure 3.10i reveals that those pixels where no thermal signal above the camera sensitivity has been detected (group A) appear to be associated to the largest average nuclear area $A_{\overline{\Delta T}_{max}<0.1\ K} = (70 \pm 35)\mu m^2$ (mean $\pm$ standard deviation). If a 0.8-K temperature threshold is selected according to the separation of the two peaks in the $\overline{\Delta T}_{max}$ histograms of figure 3.2f, the pixel-wise comparison of figure 3.10g and figure 3.10h reveals that those pixels where the amplitude $\overline{\Delta T}_{max}$ is comprised between the camera sensitivity and 0.8 K (group B) correspond to an average nuclear area $A_{0.1\,K \leq \overline{\Delta T}_{max} < 0.8\,K} = (60 \pm 30)\ \mu m^2$, and that those pixels where the amplitude $\overline{\Delta T}_{max}$ exceeds 0.8 K (group C) correspond to an average nuclear area $A_{\overline{\Delta T}_{max} \geq 0.8\,K} = (50 \pm 30)\ \mu m^2$ (figure 3.10i). The statistical significance of the difference between the mean nuclear area of group A and the mean nuclear area of both groups B and C (figure 3.10i, $p < 0.001$) highlights an inverse correlation between the amplitude of laser-primed temperature increments and the cellular nucleus size, with the cells with the largest nuclei not providing any $>$ 0.1-K temperature increment. In the literature, the melanin concentration is pointed out as a marker for melanocyte differentiation [80] and is strictly related to the degree (stage I to IV) of maturation of melanosomes [112]. Recent experiments on B16-F10 ear-pinnae-implanted primary tumors have revealed an accumulation of melanosomes in poorly pigmented proliferating melanoma cells, suggesting that most of the melanosomes in the proliferative phase are amelanotic (i.e., in stage I-II) [103]. Proliferative activity has been pointed out in turn to be positively correlated to the mean nuclear area, with nuclei of proliferating cells exhibiting higher mean surface in melanocytic skin tumors [104]. This suggests that those cells not providing a detectable thermal signal and possessing a low melanin content below our 10^{-3} M detection sensitivity correspond to the largest, and most likely highly proliferating, melanocytes. The two populations contributing to a non-zero detected thermal signal appear unresolved instead in the overall nuclear-size distribution of figure 3.10f (the mean nuclear areas of groups B and C in figure 3.10i are not statistically different at the 0.05 level).

Based on the above discussion, the biological origin of the double temperature peak in figure 3.10e,f is still unclear. Even if an analogous bimodal distribution has been reported for the length of melanosomes isolated from bovine retinal pigment epithelium [113], no similar evidence has been reported for murine melanosomes. Furthermore, considering the ~micrometer size of melanosomes, the $\sim$ 40-μm resolution of our technique should not readily enable the discrimination of different melanosomal populations, so that such a discrimination is unlikely at the basis of the temperature peaks evidenced by super-resolved thermography. Future efforts will be devoted to further identify the two different cellular subtypes observed in the B16 tissue sections: on the basis of our results, I envision the possibility of exploiting a photo-thermal analysis to extract additional features to discriminate healthy and cancerous tissue and/or to stage the temporal evolution of melanomas.

3.6 Results discussion

Super-resolved photo-activated thermal imaging is applied in this chapter as a powerful approach for the high-resolution spatial mapping of the absolute concentration of melanin pigments in excised melanoma biopsies. The technique takes advantage of a compact, low-cost benchtop microscope and relies on the accurate a-posteriori localization of laser-primed temperature variations to reconstruct the distribution of light-absorbing and heat-releasing entities in the sample with sub-diffraction $\sim$ 40-μm resolution. In particular, excitation at 514nm allows exploiting the peculiar broadband absorption and thermal relaxation properties of melanin to image pigments in label-free configuration, thereby avoiding the Fontana-Masson (FM) technique [114] as well as lengthy formalin-fixed paraffin-embedded (FFPE) immunohistochemical melanoma-black-45, Melan-A or S-100 exogenous stainings [92]. Melanin specificity is ensured by the fact that melanin is the dominant photo-thermal chromophore in pigmented skin lesions [115], with 0.99 thermal relaxation efficiency [108] and an absorption coefficient about four times higher than the absorption coefficient of hemoglobin at 514 nm [24, 116].

By the numerical integration of the full 3D heat transfer model, I have proposed and demonstrated the data-analysis protocol to convert temperature-based maps into quantitative images of the melanin absolute molar concentration. The 5×10^{-4} M lower limit of detection defined by the adopted 33-mW excitation power and by the thermal-camera temperature sensitivity has proven sufficient to investigate melanin in the $\sim$ 0.001-0.05 M concentration range, which is comparable to what

is reported for both human melanoma and human retinal pigment epithelium in the literature [101, 111]. In deriving the necessary formalism via equation 3.4.1, I have assumed that light scattering by melanin pigments is negligible relatively to absorption and transmission at $514\,nm$. Such an approximation is justified for dilute well-solubilized melanin solutions [107], but might require refinements in the presence of particle aggregation and represents the main source of uncertainty in the estimate of the melanin concentration via the relation $C = \overline{\Delta T}_{max}/m$.

By combining the implementation of super-resolution image acquisition (which retains fundamental importance to enable the characterization of pigmented skin lesions on the tissue spatial scale) with the quantification of the melanin absolute concentration, the proposed approach significantly expands the applicability of infrared thermography in the context of melanoma screening and diagnosis. In fact, even though dermatology is a compelling application area for infrared thermal imaging [22], to date conventional thermography has been limited to a few pioneering and debated qualitative clinical studies [117], aimed for example at the in-vivo malignancy-benignancy discrimination of pigmented lesions [22] or at the patient follow-up after treatment [118] based on spatially-averaged temperature measurements. For the first time, the results presented here extend far-infrared thermography to the space-resolved melanin-based imaging of mm^2- to cm^2-sized explanted biopsies: provided the crucial role played by melanin pigments in regulating the overall melanoma development and evolution, the strategy could represent a useful complement to more traditional histopathological analyses of explanted skin sections. Demonstrated here on murine B16 melanoma, the very same technique could be readily extended without necessary adaptation to the inspection of ex-vivo human melanoma biopsies in the clinical setting. With approximately 90% of all human invasive melanomas being classified as melanocytic [115], I envision broad applicability for melanin-based photo-thermal imaging of excised biopsies.

I finally remark that, in its current implementation, super-resolution thermography only exploits the thermal signal emitted from the surface of excised biopsies. However, a natural extension of the proposed imaging method would consist in the extraction of light-induced temperature depth profiles in melanomas. Numerical methods, which have been originally developed in the field of photo-acoustic imaging and have been extended to the solution of the inverse problem of heat diffusion, could allow reconstructing the laser-primed temperature field in three dimensions [119]. Even in the presence of scattering biological tissues, a tomographic image of light-absorbing entities in the sample could therefore be derived starting from the surface signal collected by the thermal camera. Coupled with a reduction of the

total imaging time, such a depth-resolved thermal imaging could be extended to the characterization of the melanoma depth in-vivo, thereby helping in the assessment of the melanoma thickness and driving surgical excision of pigmented skin lesions.

Chapter 4

A novel method for microscale thermal conductivity measurements

Thermal conductivity measurements play a crucial role in most areas of the applied physical sciences, thereby demanding for new non-invasive methods capable of providing high-resolution spatial mapping of absolute thermal conductivities on heterogeneous samples ranging from solid-state bulk materials to low-dimensionality structures. In this chapter, I lay the theoretical foundations and provide the experimental demonstration of a novel method aimed at quantitative thermal conductivity mapping with tunable ~ 50-μm resolution by the extension of the super-resolution photo-activated thermography approach presented in chapter 2. While morphological super-resolved thermal imaging only requires the amplitude of localized laser-primed temperature variations, the quantification of the sample thermal properties can be accomplished by the further exploitation of the full temperature rise-and-decay temporal kinetics. Provided proper theoretical modeling of the three-dimensional heat transfer within laser-illuminated solid slabs, the same data-sets acquired for super-resolution thermal imaging can be exploited for thermal conductivity imaging. By coupling temperature maps with the extraction of thermal properties at high spatial resolution, the results of this chapter significantly expand the capability of state-of-the-art infrared imaging technology in fully capturing the structural heterogeneity and/or functional state of the imaged materials.

4.1 Motivation

A variety of research areas, ranging from materials engineering to biotechnology, benefit from the ability of monitoring thermal conduction. The measurement of the thermal conductivity allows, for example, to optimize energy harvesting devices, to improve the lifetime and performance of electronic, thermoelectric and opto-electronic components subject to intensive heat load, and to develop heat transfer models for biological soft materials for disease diagnosis and hyperthermia-based therapeutics [21, 120, 121]. There is therefore constant demand for the development of methods capable of directly quantifying absolute thermal conductivity values over a broad (three-to-four order-of-magnitude) range in a noninvasive (non-contact) manner. Ideally, the point-like measurement of the thermal conductivity on homogeneous samples should be complemented with high resolution spatial mapping of the thermal property across extended (μm- to cm-sized) areas on heterogeneous samples ranging from solid-state bulk materials to low-dimensionality structures. Further requirements involve ease in sample preparation and flexibility in the handled sample size, geometry and mechanical properties.

The simplest techniques quantify the conductivity via Fourier's law by exploiting a known steady-state heat flow across macroscopic samples [122]. Major concerns in these contact-based techniques are heat losses and the thermal resistance between the sample surface, the heat source and the thermocouples/thermistors used for temperature sensing [122]. Furthermore, measurements are averaged over wide areas and prevent probing anisotropies due to, for example, interfaces, grain boundaries, impurities and structural heterogeneities.

More sophisticated transient (time and frequency domain) techniques provide the thermal conductivity of materials ranging from bulks to sub-micrometer films, at the expense of complicated setups (e.g., pump-probe configurations with lock-in detection schemes) [122]. Spatially resolved measurements have been obtained by thermo-reflectance imaging [123–125], Raman spectroscopy [126], extensions of the Atomic Force Microscope [127], photoluminescence imaging [128] and the combination of the 3ω method [129] with scanning thermal microscopy [122, 130]. Thermal conductivity or conductance have been mapped on halide perovskite films [130], large-grained polycrystalline diamond [131], thermal transistors [132], barrier coatings [133], $\beta \rightarrow \alpha$ cristobalite [134] and compositional diffusion multiples [135]. High ($\sim$ 100 nm-5 μm) spatial resolution has been achieved, but imaged areas are relatively small in size with typical 10- to 300-μm side.

Along with the benefits of a non-contact measurement, imaging over larger

mesoscale fields of view is a key advantage of infrared thermography [1, 136]. Recent advances ranging from the design of increasingly sensitive image sensors to the proposal of super-resolution acquisition schemes (cf. chapter 2) [60, 137–139] have turned infrared thermal imaging into a mature technology, capable of space-resolved temperature mapping down to 20-40 millikelvin resolution. Still, the technique suffers from limited specificity in fully capturing the material functional state and/or structural heterogeneity: due to the concurrence of several material and environmental parameters in determining the temperature kinetics [17], temperature images are rarely [54] converted into maps of any thermal property. The well-established laser flash method [140] provides spatially averaged thermal diffusivity measurements under uniform laser irradiation. Even under focused illumination, the radial temperature profile encoded in thermographic images is used only to retrieve diffusivity values averaged over few mm^2 [141–143]. The thermal conductivity is then deduced provided that separate measurements of the sample density and specific heat are available.

In this chapter, I develop and validate a simple procedure to (i) quantify absolute thermal conductivities over three decades ($0.1 - 100\ \frac{W}{mK}$) on both bulks and thermally thin specimens by non-contact infrared photo-activated thermal imaging, and (ii) spatially map the conductivity at sub-diffraction $\sim 50\ \mu\mathrm{m}$ resolution over extended (mm- to cm-sized) areas. This approach significantly expands the capability of infrared imaging technology towards quantitative thermal conductivity imaging over the millimeter mesoscale that is not tackled by existing state-of-the-art techniques. The method is based on the prediction that the product of the amplitude and characteristic rise time of the temperature variations primed by focused low-power laser-light illumination obeys a universal inverse proportionality on the sample thermal conductivity. Such a proportionality is initially highlighted on thermally thick and thermally thin homogeneous solid slabs by both the approximated analytical solution of the 3D heat equation and by finite-element numerical simulations in the presence of radiative and convective heat losses. The measurement procedure is validated on reference samples and, by building on the super-resolution photo-thermal image acquisition scheme presented in chapter 2 [60], it is combined with thermal imaging at sub-diffraction resolution on mm-sized areas on historical eighteenth-century tin organ pipe fragments. The product of the sample local thickness and thermal conductivity, mapped at 40-$\mu\mathrm{m}$ resolution, is pointed out as an informative parameter to characterize the sample conservation state, thereby exemplifying potential application of the proposed approach in the context of cultural heritage conservation and non-destructive material testing.

4.2 Role of the thermal conductivity in the sample thermal response

We are specifically interested here in active photo-thermal imaging, where a focused low-power continuous-wave laser beam, with visible or near-infrared wavelength lying within the sample absorption band, primes absorption and local heat releases in the sample. Under this condition, the overall Fourier's heat transfer law in the presence of conduction and convection [3] allows surmising that the laser-primed temperature increment ΔT is related to the energy flow rate $Q/\Delta t$ via the relation $Q/\Delta t = kL_c\Delta T + hA_c\Delta T$ (cf. section 1.1.1 for the details on the heat transfer modes). Here k is the sample thermal conductivity, h is the convective heat transfer coefficient, L_c and A_c represent the characteristic length and area over which heat propagation occurs. By rearranging the terms, we retrieve an expression analogous to Ohm's law: $\Delta T = R_T\dot{Q}$ with $R_T = (kL_c + hA_c)^{-1}$ acting as a thermal resistance. The product $\Delta T\Delta t$ over a whole heating ramp depends therefore on the thermal resistance times the released heat, which is proportional in turn to the excitation laser intensity I. Fourier's law allows therefore to hypothesize a universal scaling law of the type $\Delta T\Delta t \propto I/(kL_c + hA_c)$: this suggests the possibility of extracting the sample thermal properties (specifically, the thermal conductivity) from the temperature maps acquired by photo-thermal imaging in the presence of modulated laser-light illumination. In this section, I demonstrate indeed that the product of the amplitude and characteristic rise time of the temperature variations primed by focused laser-light illumination obeys an inverse proportionality on the sample thermal conductivity, irrespectively of density and specific heat capacity.

The role of the thermal conductivity in defining the thermal response of the heated sample should be theoretically derived and justified based on the full 3D heat transfer model introduced in section 1.2. Reported here for the reader's ease, the heat equation for a laser-illuminated solid slab with thermal conductivity k and thermal diffusivity D (eq. 1.2.1) reads

$$\frac{k}{D}\frac{\partial T(\mathbf{r},t)}{\partial t} - k\nabla^2 T(\mathbf{r},t) = S(\mathbf{r},t) \tag{4.2.1}$$

with the proper boundary conditions based on convective and radiative losses as specified in equation 1.2.2. The source term S accounts for modulated laser illumination (it contains the laser power and activation time, but also the sample absorption $\mathcal{A}$ and/or reflectance $\mathcal{R}$), and significantly increases the complexity of the theoretical framework. In fact, the analytical solution of the heat equation

only allows deriving complex integral expressions for the temperature space and time dependence in the approximated cases of thermally thin and thermally thick opaque solid samples. As derived in detail in section 1.2, such solutions can be written in the following forms for the case $hL/k \ll 1$ and for the case $L \to +\infty$, respectively:

$$T_{thin}(x,y,t) \approx \frac{I(1-\mathcal{R})D}{kL} \cdot \cdot \int_{t_0}^{t} \frac{\omega^2}{\omega^2+8Dt_1} exp\left(-\frac{2(x^2+y^2)}{\omega^2+8Dt_1}\right) exp\left(-\frac{2Dht_1}{kL}\right) dt_1 + T_m \quad (4.2.2)$$

$$T_{thick}(x,y,z,t) \approx \frac{I(1-\mathcal{R})D}{k} \cdot \cdot \int_{t_0}^{t} \frac{\omega^2}{\omega^2+8Dt_1} \exp\left(-\frac{2(x^2+y^2)}{\omega^2+8Dt_1}\right) \frac{1}{\sqrt{\pi Dt_1}} \exp\left(-\frac{z^2}{4Dt_1}\right) dt_1 + T_m \quad (4.2.3)$$

with $t_0 = 0$ if $t < \tau_{on}$ and $t_0 = t - \tau_{on}$ if $t \geq \tau_{on}$.

Translation of the theoretical treatment to the description of data-sets acquired in super-resolution thermal imaging experiments further requires the computation of the convolution of the temperature profiles with the camera point-spread-function, followed by a spatial average of the resulting temperature distributions over the square thermo-camera pixels, as previously detailed in section 1.3.1. The integral form of equations 4.2.2 and 4.2.3, and the double spatial integral which is inherent in the computation of pixel-averaged temperatures, clearly prevent the full derivation of the analytical expressions for $\overline{T}$ and $\overline{\Delta T}$ values.

Numerical simulations provide an alternative and feasible approach to evaluate the dependence of pixel-averaged temperature values on the sample thermal properties. The solution of eq. 4.2.1 has been therefore implemented in the COMSOL Multiphysics software (COMSOL AB, Sweden), and both the amplitude and characteristic rise time of laser-induced temperature variations have been evaluated by finite-element simulations as a function of the sample properties (conductivity k, diffusivity D and thickness L).

4.2.1 Finite-element simulations

Simulations have been performed in the thickness range $L = 20\,\mu m$-$1\,cm$, and the thermal conductivity has been varied in the broad range $k = 0.1$-$100\,W/mK$ in

order to model the behavior of materials ranging from polymers to metals. For all the materials, the thermal conductivity, thermal diffusivity, density and specific heat capacity are specified in table 4.1. Results are reported for a laser activation time $\tau_{on} = 0.2\,s$, a sample emissivity $\varepsilon = 0.9$, a laser beam waist $\omega = 30\,\mu m$ and a camera pixel size $l = 420\,\mu m$, as in our experimental configuration. A convective heat transfer coefficient $h = 10\,W/m^2K$ has been assumed, as usually adopted for the convection of air at standard conditions [4, 5, 17], and the laser power absorbed by the sample has been varied as $P_{abs} = (1-\mathcal{R})P = 0.5\text{-}1.5\,mW$. The corresponding laser intensity has been set to $I_{abs} = 2P_{abs}/(\pi\omega^2)$.

Table 4.1: Thermal diffusivity D, thermal conductivity k, density ρ and specific heat capacity C of the materials employed in finite-element simulations (from the Comsol Multiphysics Material Library and the references therein [144]).

Material	$D\left[m^2/s\right]$	$k\left[\frac{W}{mK}\right]$ at 293 K	$\rho\left[\frac{kg}{m^3}\right]$	$C\left[\frac{J}{kgK}\right]$
1. Polycarbonate	1.41×10^{-7}	0.2	1200	1186
2. Glass (Corning 1737)	5.02×10^{-7}	0.9	2545	704
3. NaCl	3.81×10^{-6}	7	2165	848
4. Li_2O	4.17×10^{-6}	15	2010	1790
5. Al_2O_3 (α, polycrystalline)	1.15×10^{-5}	35	3990	764
6. Tin (polycrystalline)	3.90×10^{-5}	65	7300	228
7. Cobalt (polycrystalline)	2.67×10^{-5}	101	8900	424

For each combination of the parameters, the simulation software allows recovering the temperature evolution as a function of space and time: it is possible to inspect both the exponential temperature rise-and-decay curve at the center of laser illumination as a function of time, and the approximately Gaussian temperature profile along the x- and y- directions of the sample plane. The average of the temperature distribution over a square region of arbitrary size (mimicking the camera pixel) and the convolution with a Gaussian point-spread-function are implemented as well, so that $\overline{T}$ and $\overline{\Delta T}$ can be directly recovered.

In the whole range for k and L, simulated $\overline{T}(t)$ temporal profiles are approximated by an exponential rise and decay [3] based on the fit trial function

$$\begin{aligned}\overline{T}(t) = &\left[\overline{\Delta T}_{max}(1 - e^{-t/\tau}) + T_m\right] \mathcal{H}(-t + \tau_{on}) + \\ &+ \left[\overline{\Delta T}_{max}(1 - e^{-\tau_{on}/\tau}) e^{-(t-\tau_{on})/\tau_d} + T_m\right] \mathcal{H}(t - \tau_{on}) \qquad (4.2.4)\end{aligned}$$

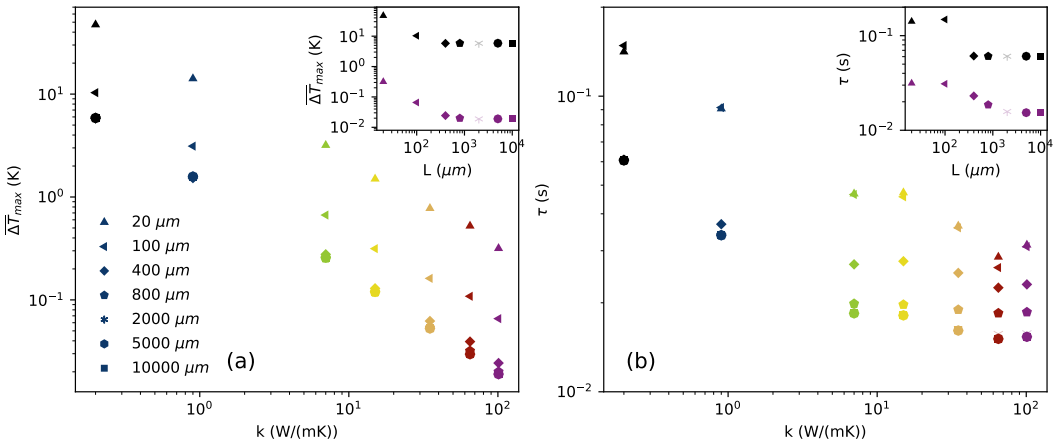

Figure 4.1: Dependence of $\overline{\Delta T}_{max}$ and τ on the thermal conductivity k, simulated by means of Comsol Multiphysics. **(a)** Predicted temperature increment $\overline{\Delta T}_{max}$ as a function of the sample thermal conductivity k. Symbols code for the sample thickness L, colors code for k and the sample materials listed in table 4.1 (polycarbonate: black, glass: blue, NaCl: green, Li_2O: yellow, Al_2O_3: orange, tin: red, cobalt: violet). Inset: predicted temperature increment $\overline{\Delta T}_{max}$ as a function of the sample thickness L at fixed k (polycarbonate: black, cobalt: violet). **(b)** Exponential rise time τ of the temperature $\overline{T}(t)$ as a function of the sample thermal conductivity k. Symbols code for the sample thickness L and colors code for k and the sample material as in (a). Inset: exponential rise time τ as a function of the thickness L at fixed k (cobalt: violet, polycarbonate: black).

$\mathcal{H}$ is the Heaviside function ($\mathcal{H}(x) = 0$ for $x \leq 0$, $\mathcal{H}(x) = 1$ for $x > 0$), while T_m is the baseline temperature. The fit of the $\overline{T}(t)$ profiles provides the plateau amplitude $\overline{\Delta T}_{max}$ of the temperature increment that would be reached at $t \to +\infty$ under continuous illumination ($\tau_{on} \to +\infty$), and the rise and decay times τ and τ_d.

From the fitted simulated $\overline{T}(t)$ profiles, no simple relationship can be drawn between the thermal conductivity k and $\overline{\Delta T}_{max}$ or τ alone (fig. 4.1). In particular, at fixed thickness, $\overline{\Delta T}_{max}$ monotonically decreases at increasing k, so that a measurement of $\overline{\Delta T}_{max}$ could in principle yield the thermal conductivity provided the slab thickness is known. However, the dependence of $\overline{\Delta T}_{max}$ on the thickness L is non-linear (inset in fig. 4.1a), and changes with k ($\overline{\Delta T}_{max}$-versus-$k$ curves in fig. 4.1a are not parallel at different L values). As a result, the overall dependence $\overline{\Delta T}_{max}(k, L)$ is empirically hard to identify.

The same considerations regarding the functional form $\overline{\Delta T}_{max}(k, L)$ apply to

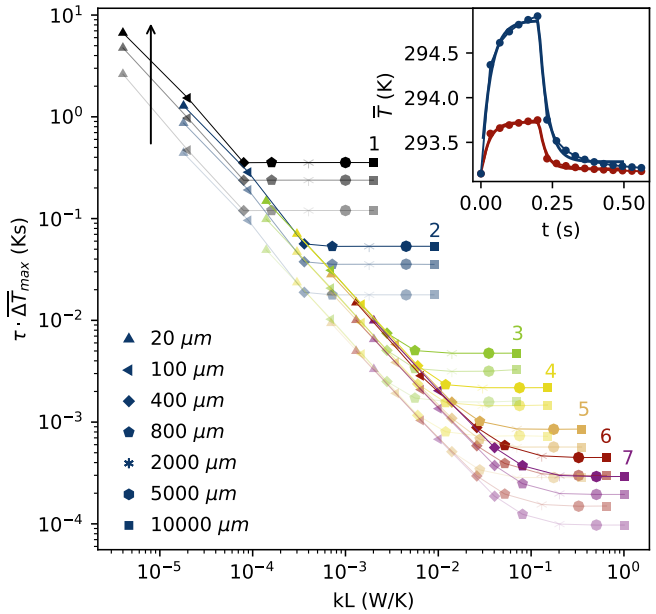

Figure 4.2: $\tau\overline{\Delta T}_{max}$ as a function of kL simulated for the seven materials listed in table 4.1 (#1 polycarbonate: black, #2 glass: blue, #3 NaCl: green, #4 Li_2O: yellow, #5 Al_2O_3: orange, #6 tin: red, #7 cobalt: violet). The thickness L is varied as listed in the legend. $P_{abs} = 0.5, 1, 1.5\,mW$ increasing along the arrow. Inset: Exemplary simulated temperature profiles for $k = 65\,W/mK$ and $L = 20\,\mu m$ (red), and for $k = 0.9\,W/mK$ and $L = 2000\,\mu m$ (blue), overlaid to the best-fit to eq. 4.2.4 ($P_{abs} = 1.5\,mW$).

$\tau(k, L)$ as well: as for $\overline{\Delta T}_{max}$, the complex dependence of τ on k and L prevents recovering k from the measurement of τ alone. The dependence of τ on the conductivity is indeed irregular even at fixed sample thickness (fig. 4.1b).

As previously discussed, Fourier's heat transfer law suggests that the product $\tau\overline{\Delta T}_{max}$ could exhibit a simpler dependence on the sample parameters k and L. This is effectively confirmed in fig. 4.2, which demonstrates that the product $\tau\overline{\Delta T}_{max}$ can be directly related to the product of k and the sample thickness L, irrespectively of the material density and heat capacity. More specifically, at fixed laser power, two regimes can be identified on the $\tau\overline{\Delta T}_{max}$-versus-kL plot depending on the thickness L (fig. 4.2). In a first regime $\tau\overline{\Delta T}_{max}$ is inversely proportional to kL, whereas in the second regime $\tau\overline{\Delta T}_{max}$ becomes constant in the $\tau\overline{\Delta T}_{max}$-versus-kL plot at fixed k: it is intuitive that, when the thickness L largely exceeds the thermal penetration

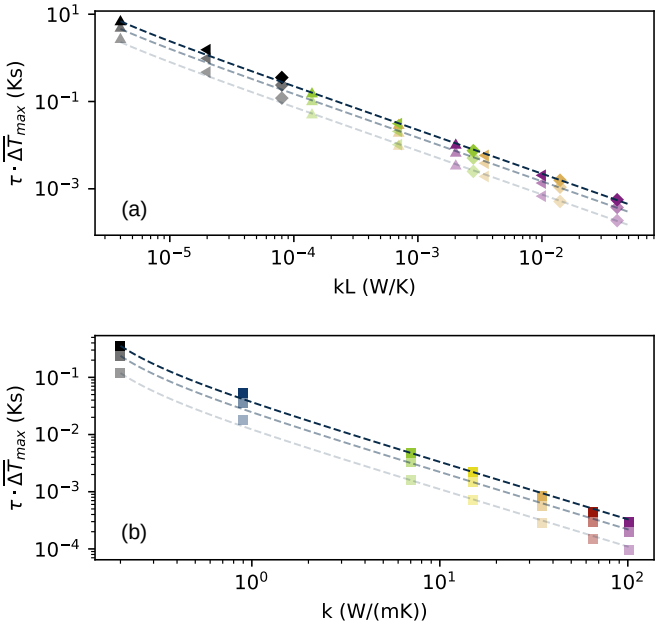

Figure 4.3: (a) Fit of the $\tau\overline{\Delta T}_{max}$-versus-kL plot to eq. 4.2.5 in the low-thickness regime. **(b)** Fit of the $\tau\overline{\Delta T}_{max}$-versus-k plot to eq. 4.2.6 in the high-thickness regime. Data points are reported from fig. 4.2 (same color and symbol code) in the range 20-400 μm for materials #1, 3, 5 and 7 in (a), and at $L = 1$ cm in (b).

length, further increasing L does not affect neither τ nor $\overline{\Delta T}_{max}$ any more. In both the regimes, $\tau\overline{\Delta T}_{max}$ appears to be directly proportional to the absorbed laser power. Overall, fig. 4.2 evidences that the conductivity can be retrieved from the experimental profile $\overline{T}(t)$: while in the low-thickness regime the knowledge of the sample thickness and of the absorbed laser power is required, in the large-thickness regime the measurement of the absorbed laser power is sufficient to directly yield the thermal conductivity from the $\tau\overline{\Delta T}_{max}$ value.

Quantitatively, in the first regime the dependence of $\tau\overline{\Delta T}_{max}$ on kL (fig. 4.3a) can be cast in the form

$$\tau\overline{\Delta T}_{max} = \frac{P_{abs}}{c_1 + c_2(kL)} \tag{4.2.5}$$

c_1 and c_2 are constants assigned by the laser waist ω, the camera pixel size l and

the losses coefficient h. In the present case ($\omega = 30\,\mu m$, $l = 420\,\mu m$, $h = 10\,\frac{W}{m^2K}$) $c_1 = (-5 \pm 2) \times 10^{-5}\,\frac{W}{sK}$ and $c_2 = (68 \pm 5)\,s^{-1}$. In the second regime instead (fig. 4.3b), a rational trial function provides direct access to the thermal conductivity via $\tau\overline{\Delta T}_{max}$ according to

$$\tau\overline{\Delta T}_{max} = \frac{P_{abs}}{c_3 + c_4 k} \tag{4.2.6}$$

For $\omega = 30\,\mu m$, $l = 420\,\mu m$, $h = 10\,\frac{W}{m^2K}$, $c_3 = (-4.9 \pm 0.7) \times 10^{-3}\,\frac{W}{sK}$ and $c_4 = (0.046 \pm 0.003)\,\frac{m}{s}$.

Equations 4.2.5 and 4.2.6 provide the explicit expressions that I will exploit to derive thermal conductivity values from experimental $\tau\overline{\Delta T}_{max}$ values throughout this chapter. For the sake of generality, the dependence of the c_1-c_4 constants on ω and h is detailed in section 4.2.2.

Regarding the separation of the two regimes identified in fig. 4.2 and eqs. 4.2.5-4.2.6, it is worth observing that such a separation occurs at variable value of the sample thickness depending on the conductivity k, with a threshold thickness typically comprised in the $\sim$ 400-800 μm range. It could be intuitive to ascribe the two regimes separation to the transition from a thermally-thin to a thermally-thick behavior. In other words, the threshold thickness could be identified based on the definition of the Biot number, with the first regime corresponding to all thickness values where the approximation $hL/k \ll 1$ holds. This is however not the case: for example, at fixed $k = 0.2\,W/(mK)$, the approximation $hL/k \ll 1$ fails at a thickness $\sim 2\,mm$, in clear contrast with what is observed in fig. 4.2. The exact dependence of the threshold thickness on the sample thermal properties is still object of investigation.

I conclude this section by remarking that the results of fig. 4.2- 4.3 agree with the predictions of Fourier's heat transfer law in demonstrating that the photo-thermal response of a laser-irradiated sample is determined by the thermal conductivity, irrespectively of density and specific heat capacity. The results I have obtained by finite-element simulations find further confirmation in the approximated analytical treatment of the 3D heat equation reported with eqs. 4.2.2, 4.2.3: the numerical integration of the approximated integral analytical solutions confirms the inverse proportionality of $\tau\overline{\Delta T}_{max}$ on kL and k depending on the sample thickness L (fig. 4.4). Of course, the integration of the analytical solutions of the heat equation is not capable of capturing the behavior of $\tau\overline{\Delta T}_{max}$ across the entire μm-cm range due to the approximations inherent in eqs. 4.2.2, 4.2.3 (inset in fig. 4.4).

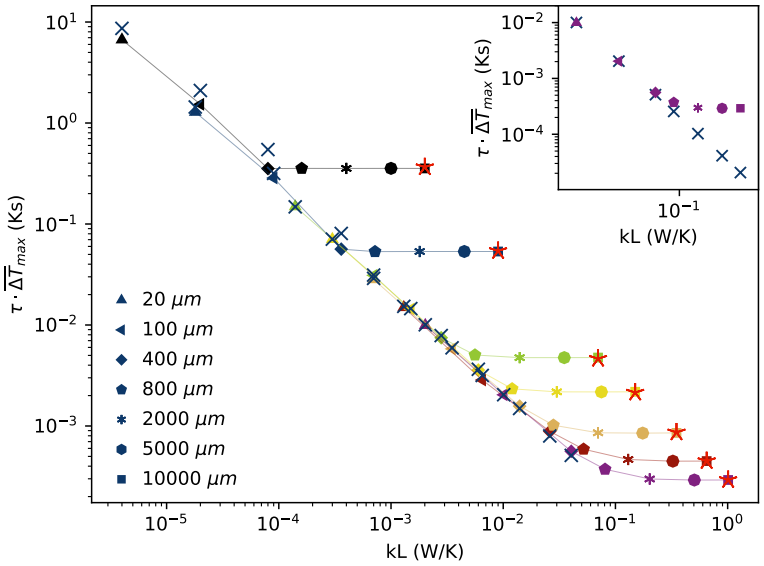

Figure 4.4: Comparison of finite-element simulations with the prediction of the approximated analytical solution of the heat equation. Blue crosses: product $\tau\overline{\Delta T}_{max}$ as a function of kL for the 7 materials exploited for fig. 4.2 at sample thickness $L = 20\text{-}400\,\mu m$. Data points are the results of the fit to an exponential rise and decay (eq. 4.2.4) of the pixel-averaged temperature time-profiles obtained by the numerical integration of the approximated analytical solution of eq. 4.2.2. Red crosses: product $\tau\overline{\Delta T}_{max}$ as a function of kL for the 7 materials investigated in fig. 4.2 at sample thickness $L = 1\,cm$. Data points are the results of the fit to an exponential rise and decay (eq. 4.2.4) of the pixel-averaged profiles obtained by the numerical integration of the approximated analytical solution of eq. 4.2.3. Colored symbols: $\tau\overline{\Delta T}_{max}$ as a function of kL is reported from fig. 4.2 at $P_{abs} = 1.5\,mW$ (same code for k as in fig. 4.2; L is coded in the panel legend) for direct comparison of finite-element simulations with the results of the numerical integration of the heat equation. Simulation parameters: $\omega = 30\,\mu m$, $\tau_{on} = 0.2\,s$, $\varepsilon = 0.9$, $l = 420\,\mu m$, $P_{abs} = 1.5\,mW$ for all data points. $h = 10\,\frac{W}{m^2K}$ for blue crosses and colored symbols; $h = 0\,\frac{W}{m^2K}$ for red crosses as assumed in eq. 4.2.3. Inset: Comparison of finite-element simulations (violet symbols) and the prediction of eq. 4.2.2 (crosses) for fixed $k = 101\,\frac{W}{mK}$ in the thickness range $L = 20\,\mu m$-$1\,cm$. Above $800\,\mu m$ the approximation of thin-sample contained in eq. 4.2.2 fails in correctly describing the temperature profile and the resulting value of $\tau\overline{\Delta T}_{max}$.

4.2.2 Beam waist and heat losses effect

The finite-element simulations exploited to construct figures 4.2 and 4.3 have been performed at fixed values of the excitation laser beam waist ($\omega = 30\,\mu m$) and of the convective heat transfer coefficient $h = 10\,W/(m^2K)$. It is therefore necessary to inspect the possible dependence on both ω and h for the value of the four constants c_1-c_4 that I have introduced for the fitting functions relating the product $\tau\overline{\Delta T}_{max}$ to kL and k (eqs. 4.2.5 and 4.2.6, respectively).

Simulations have been repeated at first at fixed $\omega = 30\,\mu m$ and increasing $h = 0\text{-}100\,W/(m^2K)$. $\tau\overline{\Delta T}_{max}$ has been recovered for polycarbonate, NaCl, Al_2O_3 and Co, and it has been plotted as a function of the product kL in the thermally thin regime ($L = 20\text{-}400\,\mu m$, figure 4.5a) and as a function of k in the thermally thick regime ($L = 1\,cm$, figure 4.5b). Convective heat losses only affect the $\tau\overline{\Delta T}_{max}$-versus-$kL$ plot at 20-μm thickness and small thermal conductivity (the two outliers in the green dataset of fig. 4.5a correspond to $L = 20\,\mu m$ at $k = 0.2\,\frac{W}{mK}$ and $k = 7\,\frac{W}{mK}$). The effect of the h parameter is even less pronounced at high sample thickness: no remarkable change in the $\tau\overline{\Delta T}_{max}$-versus-$k$ plot is observed at 1-cm thickness up to $h = 100\,\frac{W}{m^2K}$. Provided the heat transfer coefficient typically equals $h = 10\,W/(m^2K)$ for a solid sample immersed in air at standard conditions, figure 4.5a-b allows concluding the same constants c_1-c_4 can be employed under the experimental conditions of the present work irrespectively of the exact value of the heat transfer coefficient.

Figure 4.5c-d reports simulated $\tau\overline{\Delta T}_{max}$ values at fixed $h = 10\,W/(m^2K)$ and increasing ω in the decade 30-300 μm. In the thermally thin regime ($L = 20\text{-}400\,\mu m$), the beam waist does not significantly affect the $\tau\overline{\Delta T}_{max}$-versus-$kL$ plot: the same constants $c_1 = (-5 \pm 2) \times 10^{-5}\,\frac{W}{sK}$ and $c_2 = (68 \pm 5)\,s^{-1}$ can be adopted irrespectively of the beam waist up to the relatively large value 300 μm. At thickness $L = 1\,cm$, no significant effect of a beam waist variation in the range $\omega = 30\text{-}100\,\mu m$ is noticed (fig. 4.5d): best-fit constants c_3 and c_4 are the same reported in the previous section. At $\omega = 300\,\mu m$, the beam waist slightly modifies the $\tau\overline{\Delta T}_{max}$-versus-$k$ plot, with best-fit parameters $c_3 = (-7.2 \pm 0.2) \times 10^{-3}\,\frac{W}{Ks}$ and $c_4 = (0.058 \pm 0.001)\,\frac{m}{s}$. Of note, a 300 μm waist is unlikely to be used in a super-resolution photo-thermal imaging experiment, thereby confirming again the reported constants $c_3 = (-4.9 \pm 0.7) \times 10^{-3}\,\frac{W}{sK}$ and $c_4 = (0.046 \pm 0.003)\,\frac{m}{s}$ can be adopted for any beam waist value of practical interest.

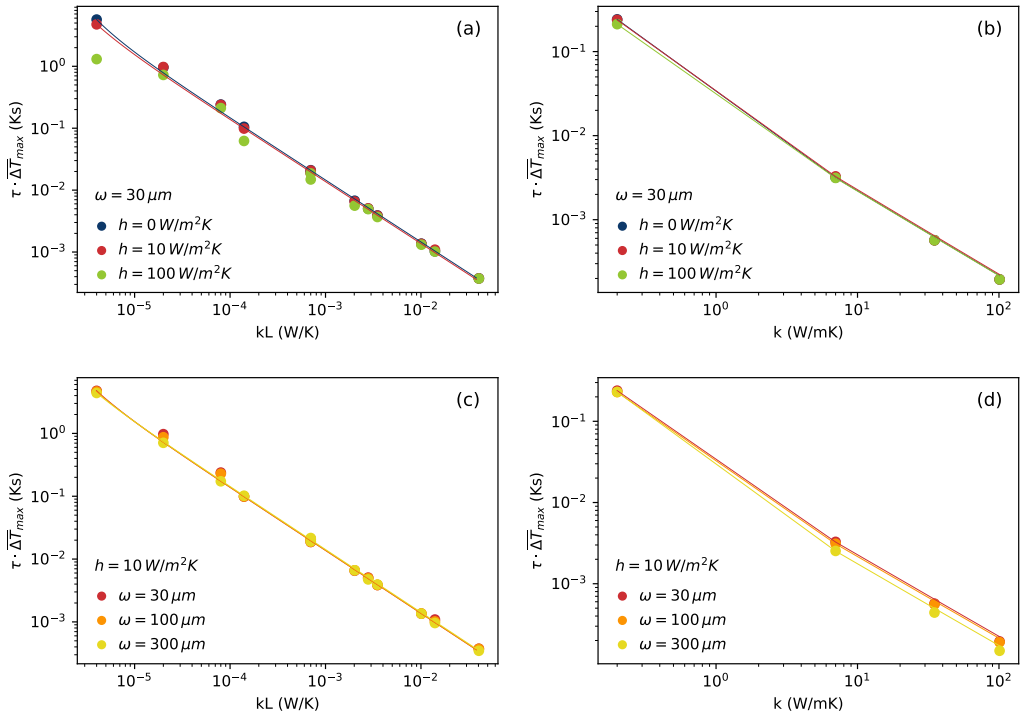

Figure 4.5: Beam-waist and heat-losses dependence of $\tau\overline{\Delta T}_{max}$. **(a)** Dependence of $\tau\overline{\Delta T}_{max}$ on the product kL at increasing h in the range h = 0-100 $\frac{W}{m^2K}$ at fixed beam waist ω = 30 µm. Data points are reported for the same materials and sample thicknesses of fig. 4.3a (polycarbonate, NaCl, Al_2O_3 and cobalt, L = 20-400 µm). **(b)** Dependence of $\tau\overline{\Delta T}_{max}$ on the thermal conductivity k at increasing heat losses h in the range h = 0-100 $\frac{W}{m^2K}$ at fixed beam waist ω = 30 µm. Data points are reported for polycarbonate, NaCl, Al_2O_3 and cobalt at fixed L = 1 cm. **(c)** Dependence of $\tau\overline{\Delta T}_{max}$ on the product kL at increasing ω = 30-300 µm at fixed h = 10 $\frac{W}{m^2K}$. Data points are reported for the same materials and sample thicknesses of fig.4.3a (polycarbonate, NaCl, Al_2O_3 and cobalt, L = 20-400 µm). The beam waist does not significantly affect the $\tau\overline{\Delta T}_{max}$-versus-kL plot in the decade 30-300 µm. **(d)** Dependence of $\tau\overline{\Delta T}_{max}$ on the thermal conductivity k at increasing ω = 30-300 µm at fixed h = 10 $\frac{W}{m^2K}$. Data points are reported for polycarbonate, NaCl, Al_2O_3 and cobalt at fixed L = 1 cm. Best fits to eq. 4.2.5 and to eq. 4.2.6 are shown as continuous lines in (a),(c) and in (b),(d), respectively. In panel (d), no significant effect of a beam-waist variation ω = 30-100 µm is noticed, so that best-fit constants c_3 and c_4 are the same reported in the text. Best-fit parameters at ω = 300 µm are $c_3 = (-7.2 \pm 0.2) \times 10^{-3}\ \frac{W}{Ks}$ and $c_4 = (0.058 \pm 0.001)\ \frac{m}{s}$. All the data points have been obtained by finite-element simulations (Comsol Multiphysics) with fixed $P_{abs} = 1.0\,mW$.

4.3 Materials and methods

4.3.1 Experimental setup

The photo-thermal imaging setup is described in detail in section 2.4.1. Specifically, the detection of thermal radiation is performed in the 7.5-13 μm spectral range by an uncooled microbolometer-based thermal camera (FLIR T650sc, FLIR Systems Inc., OR, USA) with 30-Hz frame rate. The detector provides 640×480 images, with $420\,\mu m$ pixel size on the sample plane. The thermo-camera automatically corrects for the atmospheric attenuation and the sample reflection of the thermal radiation emitted by the surroundings (cf. section 1.1.3). To this aim, the sample distance from the camera front lens ($40\,cm$, in the present case), the sample emissivity, and the relative humidity and temperature of the atmosphere have to be provided to the camera software. The emissivity has been experimentally characterized by the black-tape method [1] for all the samples.

Reflectance measurements on nylon and delrin cylinders used for the validation measurements (section 4.4) have been performed by means of a 60-mm integrating sphere (ISN-923 sphere on a V-770 UV-VIS-NIR spectrophotometer, JASCO Inc., JP), whereas reflectance measurements on historical organ pipe fragments (section 4.5) have been performed by a custom-built 20-cm integrating sphere [145] equipped with an RGB CMOS camera. The absorbance of the microfiche-printed ink sample has been quantified by means of a power meter (PM100D, Thorlabs Inc. NJ, USA) in transmission mode.

4.3.2 Finite-element simulations

Finite-element simulations have been performed by COMSOL Multiphysics [31] following equations 1.2.1 and 1.2.2. The sample has been modeled by a cylindrical slab of thickness L and radius r and the constituent material has been selected from the software material library. The employed materials are reported in table 4.1 with the corresponding values for thermal conductivity, thermal diffusivity, density and specific heat capacity. L has been varied in the range $20\,\mu m$-$1\,cm$, while the sample radius has been fixed to at least $2\,cm$ to ensure the sample behaves as an infinitely large slab in the radial direction. Due to the Gaussian symmetry of the laser beam and the overall axisymmetric properties of the system, the cylindrical slab has been modeled as a 2D rectangle and the full 3D temperature profile has been subsequently generated by rotation, with significant reduction of the total

computation time. A triangular mesh has been employed for all the simulations with 80 nm minimum element size and 10 μm maximum element size.

4.3.3 Data analysis softwares

Photo-thermal imaging raw data have been acquired with the thermo-camera software (FLIR Tools +, FLIR Systems Inc., OR, USA), exported in .csv file format and entirely processed by a custom written Python code. Data processing has been performed by the numpy and scipy Python libraries and reconstructed super-resolution images have been rendered with Python matplotlib for visualization [146].

4.4 Proof-of-principle thermal conductivity measurements

The findings of finite-element simulations (equations 4.2.5 and 4.2.6) suggest that, once the sample absorption is known, it is possible to measure k or the product kL for thick or thin samples, respectively, from the experimental measurement of $\tau\overline{\Delta T}_{max}$. The measurement is straightforward on homogeneous specimens, where a single laser illumination event at a fixed location allows quantifying the conductivity. I demonstrate here the feasibility of such single-point experiments by reporting the results obtained on reference test samples with known thermal properties.

In the low-thickness regime, a polyester (Polyethylene Terephthalate) sheet ink-printed as microfiche has been exploited ($L = 180 \pm 30$ μm; the emissivity of ink-printed polyester is $\varepsilon = 0.80 \pm 0.03$ as measured in section 2.6.1). The ink layer, deposited on the polyester substrate in a 0.4×0.4 cm^2 uniform square, is a few micrometers in thickness and provides surface absorption at 633 nm (He-Ne laser). Due to the partial transparency of the sample at the illumination wavelength, both the contributions of light transmission and light reflection have to be accounted for when measuring the absorbed laser power. If we assume, as it is reasonable, that the reflectance is the same on printed and non-printed regions of the polyester sheet, the transmittances $\mathcal{T}$ and $\mathcal{T}_{ink}$ of the plain polyester substrate and of the ink-printed polyester areas satisfy $\mathcal{T} = 1 - \mathcal{R} = P_T/P$ and $\mathcal{T}_{ink} = 1 - \mathcal{R} - \mathcal{A} = P_{ink}/P$. In this notation, P is the incident laser power, P_T is the laser power transmitted by plain polyester regions and P_{ink} is the laser power transmitted by printed polyester areas. Overall, the printed polyester absorption

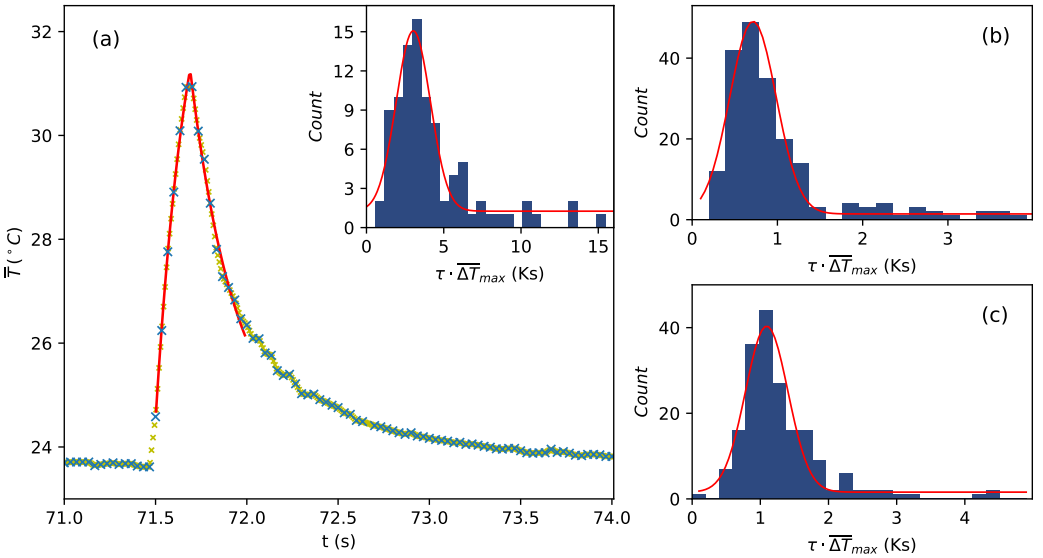

Figure 4.6: Proof-of-principle thermal conductivity measurements. **(a)** Blue crosses: experimental temperature time-profile primed on an ink-printed polyester sheet ($L = 180 \pm 30\,\mu m$), overlaid to the best fit to eq. 4.2.4 (red line). The raw time trace has been interpolated linearly to 5 times the frame rate (yellow crosses) for fitting. Inset: histogram of $\tau\overline{\Delta T}_{max}$ recovered from $N = 92$ temperature peaks. **(b)**, **(c)** Histogram of the $\tau\overline{\Delta T}_{max}$ values recovered on delrin and nylon, respectively ($N = 198$ in (b) and $N = 191$ in (c)). The best estimates of $\tau\overline{\Delta T}_{max}$ provided by Gaussian fitting of the histograms (red lines) are reported in the text for all the samples.

coefficient $\mathcal{A}$ can be retrieved as $\mathcal{A} = (P_T - P_{ink})/P$, leading to an absorbed laser power $P_{abs} = \mathcal{A}P = P_T - P_{ink}$. Measurement of P, P_T and P_{ink} by a power-meter has led to $P_{abs} = (8.8 \pm 0.2)\,mW$. Illumination has been repeated $N = 92$ times with $\tau_{on} = 0.2\,s$ at the same location on the sample plane, and an image sequence has been asynchronously acquired by a thermal camera at 30-Hz frame rate. Each detected temperature rise-and-decay has been fit to eq. 4.2.4 (fig. 4.6a), and by the Gaussian fit of the histogram of all the recovered $\tau\overline{\Delta T}_{max}$ values (fig. 4.6a) the best estimate $\tau\overline{\Delta T}_{max} = (3.03 \pm 0.11)\,Ks$ (mean $\pm$ standard error) has been recovered. By substitution of $\tau\overline{\Delta T}_{max}$, P_{abs} and the thickness $L = (180 \pm 30)\,\mu m$ into eq. 4.2.5, a thermal conductivity $k = (0.24 \pm 0.05)\,\frac{W}{mK}$ has been obtained, in agreement with the value $k = 0.17$-$0.24\,\frac{W}{mK}$ reported for polyester in the literature [147–149].

Sequential repeated illumination has been employed here for statistical purposes.

The standard deviation $\sigma_{\tau\overline{\Delta T}_{max}} = 1.1\,Ks$ of the Gaussian histogram of the $N = 92$ measurements (fig. 4.6a) provides an estimate of the uncertainty on the $\tau\overline{\Delta T}_{max}$ value when a single measurement is exploited. The corresponding uncertainty on the thermal conductivity can be estimated in $0.1\,\frac{W}{mK}$.

In the thermally thick regime, validation experiments have been performed on 5-cm thick opaque nylon and delrin (Polyoxymethylene) cylinders. A 60-mm integrating sphere has been employed to quantify the total (diffuse and specular) reflectance at 633-nm, yielding $\mathcal{R} = (0.040 \pm 0.003)$ for delrin and $\mathcal{R} = (0.046 \pm 0.003)$ for nylon. The corresponding absorbed laser power has been set to $P_{abs} = P(1-\mathcal{R}) = (11.2 \pm 0.1)\,mW$ for both the experiments. The laser pulse ($\tau_{on} = 0.2\,s$) has been repeatedly shot at the same location and the temperature time-trace has been acquired by the thermal camera following the evaluation of the samples emissivity ($\varepsilon = 0.93 \pm 0.01$) by the black-tape method [1]. Each of the N temperature rise-and-decay responses has been fit to eq. 4.2.4 to recover $\tau\overline{\Delta T}_{max}$. The Gaussian fit of the histogram of the $\tau\overline{\Delta T}_{max}$ values (fig. 4.6b,c) provides the best estimates $\tau\overline{\Delta T}_{max} = (0.71 \pm 0.02)\,Ks$ (mean $\pm$ standard error, $N = 198$) and $\tau\overline{\Delta T}_{max} = (1.09 \pm 0.02)\,Ks$ (mean $\pm$ standard error, $N = 191$) for delrin and nylon, respectively. By the substitution of $\tau\overline{\Delta T}_{max}$ and P_{abs} into eq. 4.2.6, the thermal conductivities can be estimated in $k = (0.45 \pm 0.03)\,\frac{W}{mK}$ for delrin and $k = (0.33 \pm 0.03)\,\frac{W}{mK}$ for nylon. Both values agree with separate measurements ($k = (0.46 \pm 0.02)\,\frac{W}{mK}$ and $k = (0.36 \pm 0.02)\,\frac{W}{mK}$ for delrin and nylon, respectively) performed by a portable transient-line-source thermal conductivity meter (ThermTest TSL-100, Thermtest Instruments, NB, CA) operating according to the ASTM D5334-14 standard.

4.5 Super-resolution kL imaging on eighteenth-century tin-rich organ pipe fragments

Proof-of-principle single-point experiments reported in section 4.4 demonstrate the possibility of quantifying kL and the thermal conductivity from experimental $\tau\overline{\Delta T}_{max}$ values at a single spatial location of a homogeneous sample. The procedure can be readily extended to spatially resolved measurements on heterogeneous specimens. Indeed, any time the focused excitation beam impinges on a light-absorbing and heat-releasing area, the resulting temperature variation encodes information on (i) the local sample thermal property (kL or k, depending on the thickness L) via the temperature kinetics in the form of the product $\tau\overline{\Delta T}_{max}$, and (ii)

Figure 4.7: Photography of the organ pipe fragment. The three red ROIs indicate the regions that have been analyzed and will be presented in the following. Specifically, the results obtained on ROI 1 are reported in fig. 4.9, whereas those recovered on ROIs 2 and 3 are shown in fig. 4.10.

the location of the absorptive center, that can be determined by centroid Gaussian surface fit of the temperature profile imaged by the thermal camera.

In chapter 2, I have demonstrated that the localization of temperature peaks can be performed well below the $\sim 265\,\mu m$ resolution limit set by the diffraction of 7.5-13 μm thermal radiation at the low-numerical-aperture collecting lens (Abbe's law). Specifically, provided the sample is laser scanned, a temperature-based map of the sample heat-releasing centers can be reconstructed and color-coded by the localized centers and amplitudes of all the measured temperature peaks [60]. Here, I extend this approach so that for each induced temperature peak I extract the time-trace $\overline{T}(t)$, fit it to eq. 4.2.4 in order to recover $\tau\overline{\Delta T}_{max}$, and reconstruct a $\tau\overline{\Delta T}_{max}$ image at tens-of-μm resolution. Its overlay to a reflectance image of the same sample region allows to derive a super-resolution image of kL (or k) by the pixelwise application of eq. 4.2.5 (or eq. 4.2.6).

The feasibility of the approach has been demonstrated by imaging experiments on a flattened historical organ pipe fragment (fig. 4.7). The sample is a lamina from an eighteenth-century instrument located in a church in Ragusa (Sicily, Italy). The

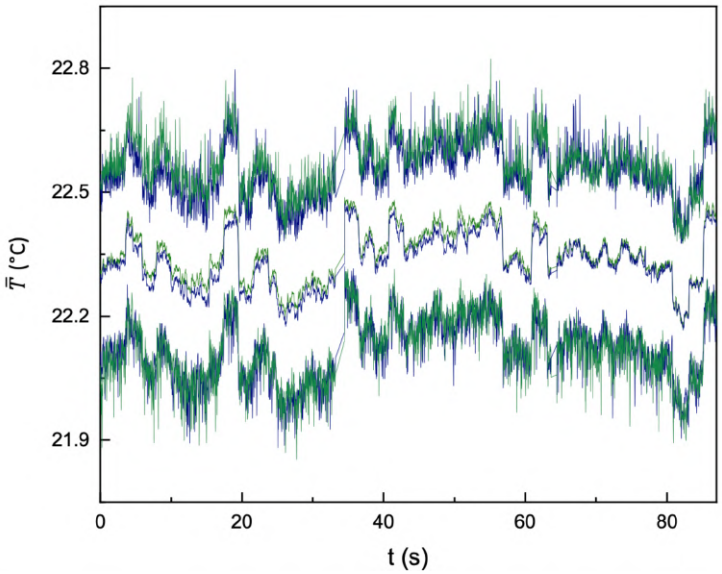

Figure 4.8: Emissivity measurement on the organ pipe fragment by the black-tape method [1]. Continuous blue lines: temporal evolution of the maximum, average and minimum temperature signals detected in the tape ROI with $\varepsilon_{tape} = 0.95$. Continuous green lines: temporal evolution of the maximum, average and minimum temperature signals exported from an exemplary ROI on the organ pipe with $\varepsilon = 0.93$.

fragment, made of a tin-rich alloy, is affected by evident deterioration. The alteration patterns can be ascribed to the presence of different crystallographic phases, possibly ranging from beta-tin to the tin oxides romarchite (SnO) and cassiterite (SnO_2). It is indeed well known that the major deterioration of historical organs is due to the so-called tin pest, that is an autocatalytic allotropic transformation of the metallic tin beta phase to the brittle tin alpha phase. This phase transformation is spontaneous at temperatures of 13.2 °C and below, but it is strongly accelerated by lower temperatures (roughly below −30 °C [150]), highly humid atmosphere or high concentration of halides in the environment (for instance in seaside towns) [151]. On the other hand, the addition of lead, antimony or other metals to the cast would usually delay the process [152]. Tin oxides have been highlighted as possible precursors of the tin pest [153], and have already been observed on mid-eighteenth-century organ pipe fragments, even in the absence of the tin alpha phase [150].

The presence of holes up to a few mm in lateral size produces variability in the sample thickness from a few μm up to $\sim 600\,\mu m$, classifying the lamina as a thermally thin slab obeying equation 4.2.5. Aiming at verifying whether the compositional heterogeneities also translate into alterations of the thermal conductivity, super-resolved thermography has been applied to the organ pipe lamina upon characterization of the sample emissivity by the black-tape method [1] as already employed in section 2.6.1. Briefly, part of the sample has been covered by black matte tape of known emissivity ($\varepsilon_{tape} = 0.95$) and, under thermal equilibrium (at room temperature), two regions of interest centered on the tape and on the sample, respectively, have been selected on the thermal camera frames. While the emissivity ε_{tape} is employed for the temperature measurement in the tape ROI, an emissivity ε is set on the sample ROI: the correct sample emissivity ε is retrieved by varying it in the camera software until the thermal image provides the same temperature for the tape and sample ROIs. Figure 4.8 shows the temporal evolution of the maximum, average and minimum temperature signals detected in the tape ROI with $\varepsilon_{tape} = 0.95$, and the maximum, average and minimum temperature signals exported from an exemplary ROI on the organ pipe with $\varepsilon = 0.93$. Compatible maximum, minimum and average temperature values are retrieved over the two (tape and sample) regions of interest when a constant sample emissivity $\varepsilon = 0.93$ is adopted. In other words, adopting a constant emissivity value $\varepsilon = 0.93$ for all the $420\,\mu m$ camera pixels enclosed in the imaged sample region produces minimum-to-maximum temperature fluctuations that resemble, and do not exceed, those registered on the tape ROI due to the thermal camera sensitivity.

It is worth remarking that, beside providing the necessary absolute value of the emissivity, the black-tape method allows excluding variability of the organ-pipe emissivity over the spatial scale ranging from $\sim 0.2\,mm^2$ to $\sim 1\,cm^2$ (the chosen tape and sample ROIs are $\sim 1\,cm^2$ in size, each ROI being sampled with $\sim 0.2\,mm^2$ pixels). Heterogeneity of the emissivity over a spatial scale smaller than the $420\,\mu m$ camera pixel size cannot in principle be excluded. I recall however that, while perfectly polished metal surfaces can display emissivities as low as 0.02, the emissivity is typically much larger - reaching values above 0.8 - if the surfaces are roughened and/or modified by oxidation/corrosion (as expected for the imaged organ pipe fragment) [1]. Based on the 0.8-0.9 emissivity values reported in the literature for oxidized metals [1], I expect a maximum variability in the emissivity of the organ pipe fragment of about 10%. This would translate in turn into a maximum estimated 15% uncertainty on recovered $\tau\overline{\Delta T}_{max}$ values.

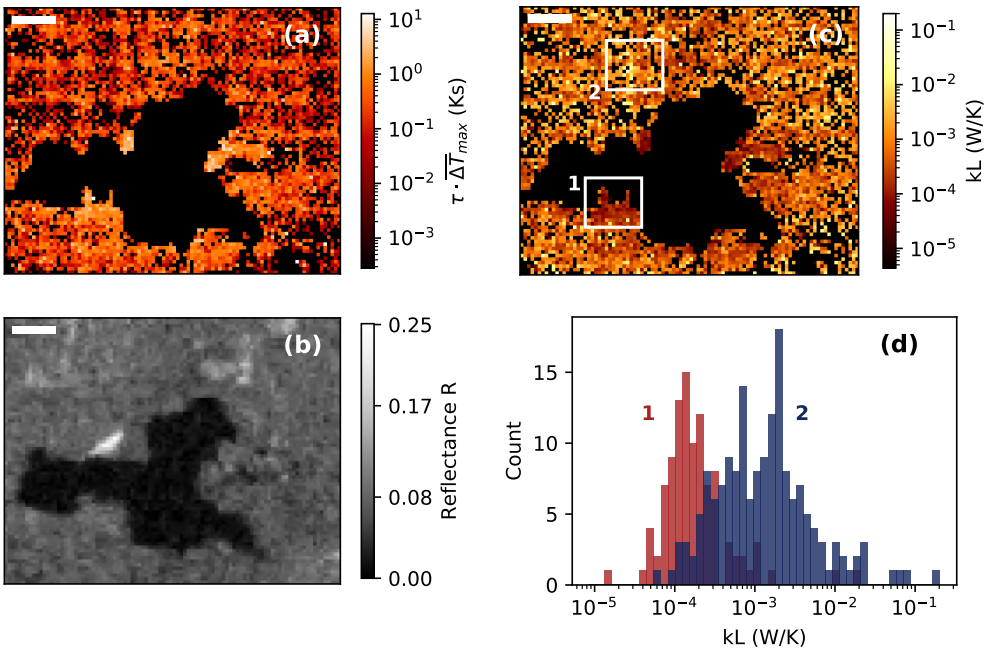

Figure 4.9: kL super-resolution imaging. **(a)**, **(b)** $\tau\overline{\Delta T}_{max}$ image and reflectance image, respectively, of a ROI of the tin organ pipe fragment. The black central region corresponds to a hole in the sample due to oxidation-related deterioration. **(c)** kL image of the same ROI of panels (a), (b) provided by inversion of eq. 4.2.5. **(d)** kL histograms extracted from the white ROIs in (c). Acquisition parameters: 633-nm He-Ne beam, $P = (11.6 \pm 0.1)$ mW, pixel size $\delta x = 40.5\,\mu m$, $\tau_{on} = 0.2$. Scale bar: 500 µm everywhere.

Following the emissivity characterization, a $\tau\overline{\Delta T}_{max}$ image and a reflectance map have been acquired on a first evidently damaged Region Of Interest of the pipe (ROI 1 in fig. 4.7). The reconstructed $\tau\overline{\Delta T}_{max}$ image (fig. 4.9a) highlights spatial heterogeneities in the broad range 10^{-3}-10 Ks. The reflectance image (fig. 4.9b) quantifies R in the range 0.04-0.25, compatibly with the reflectance reported for tin oxides in the literature [154]. Provided the reflectance map is re-binned to achieve the same pixel size of the $\tau\overline{\Delta T}_{max}$ image, the overlay of fig. 4.9a,b and the pixel-wise inversion of eq. 4.2.5 allow reconstructing the sub-diffraction image of kL, with kL values spanning multiple decades (fig. 4.9c,d).

Two relevant conclusions can be drawn. The division of the kL map by a single constant k value never returns a physically reasonable thickness (~ 10-600 µm

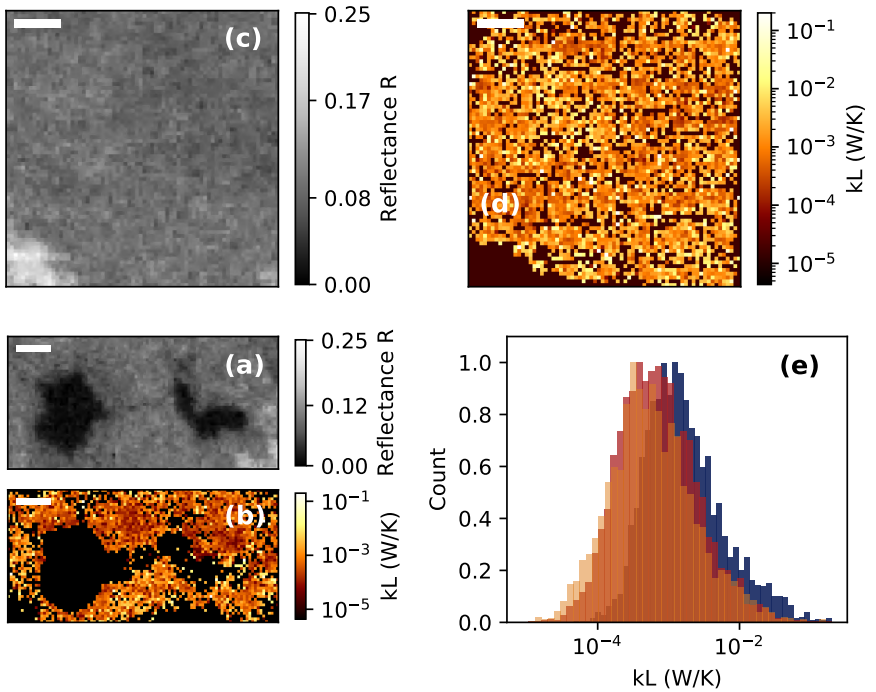

Figure 4.10: kL super-resolution imaging. **(a)**, **(c)** Reflection images of additional ROIs on the pipe fragment. **(b)**, **(d)** kL images of the same ROIs of panels (a) and (c), respectively. Acquisition parameters: 633-nm He-Ne beam, $P = (11.6 \pm 0.1)$ mW, pixel size $\delta x = 40.5\,\mu m$, $\tau_{on} = 0.2$ in (b); 514-nm Ar beam, $P = (28.8 \pm 0.1)$ mW, $\delta x = 40.5\,\mu m$, $\tau_{on} = 0.2$ in (d). Scale bar: 500 µm everywhere. **(e)** kL histograms recovered in (b) and (d) and in the whole fig.4.9c (orange, blue and red respectively).

expected range) across the whole ROI, indicating that both k and L are changing across the sample. The smallest kL values are primarily retrieved close to the hole borders, but also appear in patches hundreds of µm away. It is reasonable to ascribe small kL values to the result of the sample oxidation, that produces a reduction of both the sample thickness and the thermal conductivity relatively to less-oxidized phases (k values as low as $\sim 1\,\frac{W}{mK}$ have been reported for SnO [155], to be compared with $65\,\frac{W}{mK}$ for polycrystalline tin). This is confirmed by the comparison of the kL images acquired on variably damaged areas of the pipe fragment (ROIs 2 and 3 in fig. 4.7). Results similar to those of fig. 4.9a-c have been recovered nearby eroded regions (fig. 4.10a-b), whereas systematically higher kL values have been

retrieved in more uniform areas further away from the damage (fig. 4.10c-e). It is also noteworthy that the high-reflectance areas in fig. 4.10c produce $\tau\overline{\Delta T}_{max}$ values below the thermal camera sensitivity: correspondingly high kL values appear as undetected in fig. 4.10d but should be indicative of very low or absent sample damage.

These results point out that the product kL is in itself a useful parameter for the non-invasive characterization of the sample conservation state, with higher kL values being associated to least damaged areas. The acquisition of kL images could find potential application in archeometallurgical studies of cultural heritage artifacts for the early-stage diagnosis of sample deterioration, with the benefits of non-destructiveness and of imaging capability over extended fields of view. I finally remark that kL images could in principle be converted into thermal conductivity images provided a pixel-wise measurement of the sample thickness. This could be obtained by coupling simultaneous front- and rear-face thermal acquisitions. The front-face data set would provide access to kL, whereas the back-face data set would provide L through the thickness-dependent time delay in the appearance of laser-primed temperature increments. Profilometry could be exploited as well, even though the unevenness of both surfaces of the organ pipe fragment demands for sophisticated implementations capable of rendering the full 3D topological structure.

4.6 Results discussion

In summary, in this chapter I have laid the theoretical foundations and provided the experimental demonstration of a novel procedure for the quantification of absolute thermal conductivities over three decades on both bulks and thermally thin specimens by non-contact infrared photo-thermal imaging.

The importance of the results is twofold. From the theoretical point of view, I have shown that the thermal response of a photo-activated sample is completely determined by the product of thickness and thermal conductivity, kL, or by the thermal conductivity alone for thin and thick slabs, respectively. A universal scaling law has been identified on the $\tau\overline{\Delta T}_{max}$-vs-$kL$ plot across more than five decades in kL, thereby providing access to the measurement of thermal conductivities in the broad range ~ 0.1-$100\ \frac{W}{mK}$. The upper limit is set by the $\sim 0.1\ K$ sensitivity of our commercial thermal camera (the higher k, the lower the amplitude of laser-primed temperature variations) at our typical tens-of-mW laser power. The lower limit

is mainly set by the accuracy in the estimate of τ. Lower k values are associated to longer characteristic rise times, that might be better captured by fitting $\overline{T}(t)$ over a timescale longer than our typical $0.2\,s$ time window. At the expense of the experiment duration, this would reduce the uncertainty on k with respect to the $0.03\,\frac{W}{mK}$ standard error I have reported from the validation experiments on polyester, nylon and polyoxymethylene samples.

The proposed approach does not require the knowledge of the sample heat capacity and density, but it requires the characterization of the slab absorption at the illumination wavelength by means of integrating spheres on opaque samples, as done here. Finally, I remark that space-resolved k- or kL- sub-diffraction imaging is enabled over wide (mm^2 to cm^2) fields of view on samples whose size is often challenging for temperature and heat flow measurements by other current state-of-the-art techniques [122]. Due to the possibility of a non-contact measurement and to a simple and inexpensive benchtop (possibly portable) setup, k and kL imaging can be applied in the context of cultural heritage conservation, electronics, material sciences and in heat transfer studies on biomaterials and bio-inspired soft materials, where the measurement of thermal properties would be beneficial, e.g., for disease diagnosis [156] or the development of photo-thermal platforms for cell stimulation and tissue engineering [157].

Appendix A

Collateral project: laser fabrication of photo-activatable biomaterials

Throughout this thesis I presented the main results that I have obtained in the field of super-resolution photo-thermal imaging. This project has strongly characterized my research activity during the 3 years of the whole PhD. However, a side project based on the fabrication of 3D proteinaceous microstructures with photothermal functionality and tunable elasticity has had a great relevance both in terms of profuse efforts and obtained results [157–159]. For this reason, I would like to briefly summarize in the present appendix the ideas behind this collateral project.

A.1 Motivation

The advances in the fabrication of 3D functional micro-structures [160–162] is fostering applications in many fields [163]. Developments related to medicine, such as physical stimulation of cells and tissue regeneration in general [164], are particularly promising. Direct Laser Writing (DLW) of proteinaceous micro-structures [165–170] offers many advantages for biomedical applications, since it exploits photo-crosslinking [171] that occurs at low temperature and limits the damage to the chemical structure of the protein [172]. Two-photon excitation (TPE) [173, 174] coupled to DLW allows to fabricate biocompatible nano-structures [9,15,19-24] down to a resolution of few tens of nanometers [25] in a single ink deposition. At the same time, the use of Near InfraRed (NIR) wavelengths (800-1200 nm) for TPE

further reduces the possible damage to the biological components in the ink [175].

Functional micro-structures can be obtained by post-writing coating with specific cellular receptors [176] or by dispersing functional compounds, such as nanoparticles, in the DLW ink before printing [177]. Gold nanoparticles have limited toxicity [178] and feature Localized Surface Plasmon Resonances (LSPRs) [179] whose energy depends on size, shape and the surface dielectric constant [180]; the LSPRs fall in the Visible-NIR range and give rise to a pronounced photo-thermal effect. These features have triggered a demand for gold-based polymer nanocomposites [162, 181] to be applied as biosensors [179], as flexible electronics [182], in antibacterial treatment [183] or in artificial implants. The pronounced photo-thermal activity [184] can also be exploited for electrical or thermal stimulation of cells [185].

The aim of this part of my research activity consists in the development of protein-based micro-structures with photo-thermal functionality in the NIR spectral region arising from dispersed gold nanoparticles. The spatially confined heat loads could then be used, for example, for micro-pumps in microfluidics [186] or to induce highly localized responses in cells, for which biocompatible micro-devices are needed [187]. In this direction, proteinaceous photo-thermal microstructures can be used to physically induce the differentiation of neuron cells, as recently proposed [185], with no application of chemical stimuli. Indeed, a systematic study which is currently ongoing in our laboratory is revealing a clear effect of thermal stimulation on the differentiation and activity of neuron cells on a macroscopic scale.

A.2 Results

Fabrication of three-dimensional biocompatible proteinaceous microstructures ($\sim$ 1-50 μm in lateral size) with tunable elasticity and photo-thermal activity in the near-infrared has been obtained by two-photon laser writing. Structure printing relies on the photo-crosslinking of the protein bovine serum albumin (BSA, 50 $\frac{\text{mg}}{\text{ml}}$) initiated by the Rose Bengal dye (RB, 2 mM concentration), whereas photo-thermal functionality is achieved by the dispersion of non-spherically symmetric metallic nanoparticles into the ink. Structures with arbitrarily complex shape and custom size can be fabricated at will starting from a Stereo-Lithography interface format (STL) file which is directly fed to the laser-writing setup and interface that I specifically designed (figure A.1). The DLW setup includes a Ti:Sa femtosecond

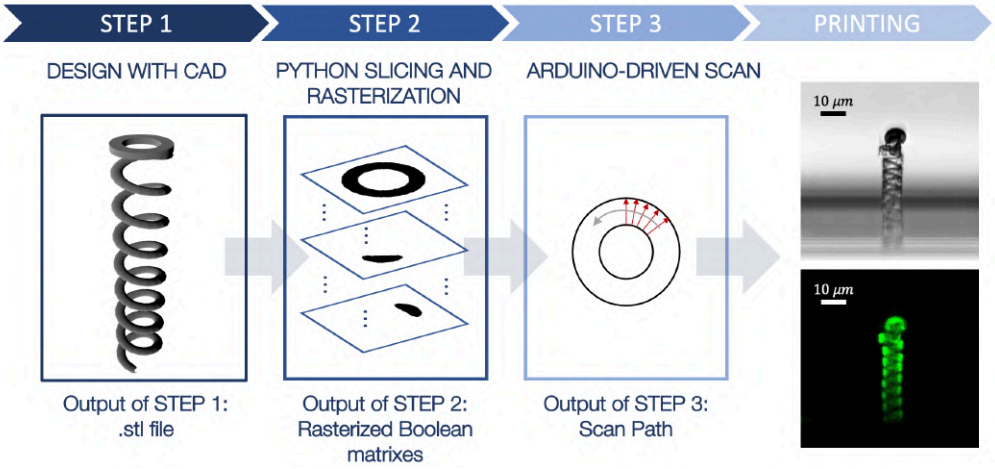

Figure A.1: Cartoon of the printing procedure. The printing pipeline consists in a sequence of integrated steps. Step 1: a CAD software is exploited to design the structure shape and size; the first-step output is an STL (STereo-Lithography interface format) file containing the mesh of the object. Step 2: the STL file is fed to a custom-written Python code, which slices the object in z-planes with adjustable z-step; for each plane, the code provides a rasterized Boolean matrix identifying the pixels (shown here in black) where polymerization should take place. The number of pixels involved in the rasterization of the matrix can be adjusted in the code. Step 3: the stack of rasterized matrices, provided as output of step 2, is fed to an Arduino board. The board has been modified to house an SD slot, so that matrices are saved in an SD card as ascii file. By means of three DAC (Digital to Analog Converter) modules, the Arduino board drives the sample piezo stage along the x-, y- and z- axes according to the desired printing path. Step 3: photo-polymerization occurs along a polar scan, where the coordinates of the pixels identified in step 2 are identified by the corresponding radial and angular coordinates. When compared with a conventional raster scan path, the polar scan allows printing structures with cylindrical symmetry. The final pipeline output is the printed microstructure, as exemplified here with a transmitted-light image and a confocal fluorescence image of a RB/BSA helicoidal microstructure.

laser source (Tsunami, Spectra-Physics, CA, repetition rate $f_R = 80\,MHz$; pulse width $\tau_P \cong 250\,fs$ on the sample plane) focused by a microscope-objective (Nikon dry objective 60X, $WD = 0.3\,mm$, $NA = 0.85$). The sample is moved by a 3-axis piezo-driven stage (Hera P733 coupled to a Pifoc-P725, Physik Instrument, D) mounted on an inverted (Nikon TE300) microscope.

I have investigated the DLW wavelength range 740-850 nm and swept the power from 10 mW to 150 mW , building microstructures of increasing thickness (1 μm to 50 μm). Stable micro-structuring conditions could be obtained at writing speeds up to 10 $\mu m/s$, only in a narrow power range (100mW-150mW). Below 100 mW, the microstructures suffered from discontinuities. Above 150 mW and at low scanning rates, microbubbles prevented writing, and at scanning rates $\cong 10\,\frac{\mu m}{s}$ no stable microstructures could be written even though microbubbles were not forming. The quality of the written microstructures has been assessed by fluorescence confocal imaging of the Rose Bengal dye in the microstructures and by SEM and AFM imaging. The high finesse of the microstructures has been confirmed by both SEM and AFM images, with an estimated writing spatial resolution of 520-560 nm. All these results indicate a limited influence of the localized heat load on the BSA/RB ink while writing.

Aiming at a subsequent application of the fabricated microstructures as platforms for cell growth and stimulation, I have carried out a thorough characterization of their mechanical and photo-thermal properties, which remarkably depend on the ink composition and the structure shape. Preliminary data obtained by AFM indentation on DLW rectangular parallelepipeds have quantified the structures Young modulus in the broad 100-1000 kPa range depending on the BSA concentration. This value agrees with that of soft biological tissues [188] and biomimetic materials [189] and suggest that these structures could be used as a substrate for cell growing. Indeed, 4T1 cells (human breast cancer) grew for at least 24 hours on the proteinaceous microstructures with no evidence of cytotoxicity. A thorough investigation of the cytotoxicity of the fabricated microstructures is currently under way.

The structures stiffness has been further characterized by subjecting elongated cylindrical microstructures to steady flow in a microfluidic device: real-time observation of their bending dynamics by a conventional transmitted light microscope has allowed deriving the elastic bending constant, that has been in turn related to the Young modulus under the rod-like shape approximation. I am not giving here the details of this analysis that is the subject of a manuscript in preparation. The results have demonstrated the tunability of the elasto-mechanical properties of the

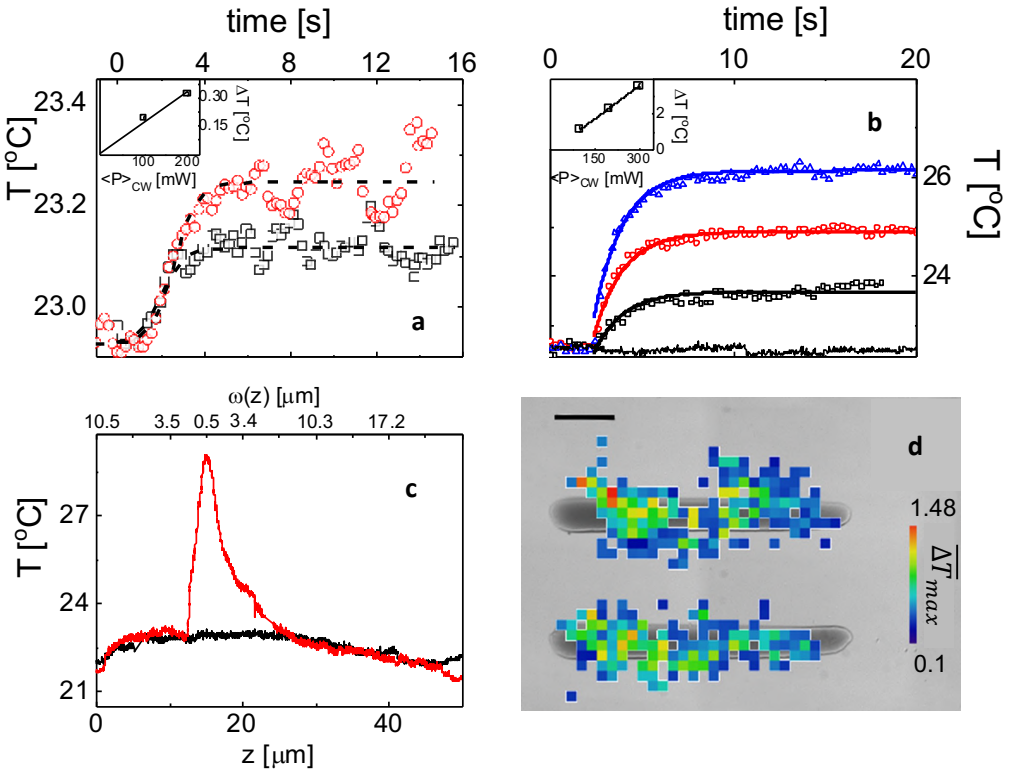

Figure A.2: Thermal characterization of proteinaceous micro-structures. **(a)** Time and power (inset) dependence of the temperature induced on the RB/BSA/GNS micro-structures by CW laser irradiation at 800 nm and $\langle P \rangle_{CW} = 100\,mW$ (black squares), $\langle P \rangle_{CW} = 200\,mW$ (red circles). The slope of the plateau temperature on the irradiation power (inset) is $1.7 \pm 0.2\,^{\circ}CW^{-1}$. **(b)** Time and power (inset) dependence of the temperature induced on the RB/BSA/GNS meso-structures ($1 \times 3 \times 0.1$ mm) by CW irradiation at 800 nm for $\langle P \rangle_{CW} = 100\,mW$ (black squares), $\langle P \rangle_{CW} = 200\,mW$ (red circles), $\langle P \rangle_{CW} = 300\,mW$ (blue triangles). The continuous thin line is the background measured on a structure not leaded with nanoparticles. The solid lines are the best fit to an exponential growth. The slope of the plateau temperature on the irradiation power (inset) is $12.2 \pm 0.4\,^{\circ}CW^{-1}$. **(c)** Photothermal effect measured in RB/BSA/GNS micro-structures (a filled square 50 μm in side, irradiation wavelength: 800 nm, $\langle P \rangle_{CW} = 300\,mW$) as a function of the laser mode (CW, black; pulsed, red) and of the beam size (upper x-axis) on the micro-structured sample during a z-scan along the optical axis (lower x-axis). **(d)** High-resolution photo-thermal image of the structures studied in (b), superimposed to their transmission image. Scale bar: 200 μm, $\lambda = 633$ nm, $\langle P \rangle_{CW} = 35\,mW$.

printed microstructures, and pave the way to their application to the physically induced stimulation and differentiation of cells in a spatially controlled manner.

In parallel, I have focused on the optimization of the photo-thermal activity of the structures. Anisotropic gold nanoparticles, dispersed in the ink, get trapped into the structure during the photo-crosslinking process and lead to localized heat release upon excitation in the near-infrared spectral region. The temperature increment is rapidly (~ 1 s) reached and maintained under continuous wave laser irradiation at 800 nm with a photo-thermal efficiency of $\frac{\partial \Delta T}{\partial P_{CW}} = 12.2 \pm 0.4 \, \frac{^\circ C}{W}$ (figure A.2). The amplitude of the temperature variation has been quantified as a function of the incident laser power by means of infrared thermography, and has been correlated to both the structure thickness and the nanoparticles concentration.

The resulting spatially confined heat loads, in combination with the tunability of the elasto-mechanical properties of the printed micro-structures, will be exploited in the near future to induce the aforementioned physically induced stimulation and differentiation of cells in a spatially controlled manner.

Conclusions

Temperature and externally induced temperature variations provide a powerful imaging contrast agent. A number of well-established techniques indeed rely on temperature for the quantitative investigation of the morphology and functional state of biological and inorganic samples. Temperature is typically probed indirectly, either through the response of optical properties - such as reflectance and index of refraction - to a modulated change in the sample temperature, or by the quantification of the sample thermal radiation in the infrared spectral band. The latter approach is at the basis of infrared thermography, and enables a conceptually straightforward retrieval of absolute temperature values: a microbolometer-based thermal camera senses the sample infrared radiance, which is subsequently converted into a temperature value by Stefan-Boltzmann's law under the grey-body approximation.

Infrared thermography offers the advantages of quantitative and non-invasive (non-contact) temperature measurements over variably extended ($> \mathrm{mm}^2$ sized) sample areas. However, resolution is intrinsically limited by the combined effect of light diffraction at the thermal-camera collecting lens (i.e., the well-known Abbe's law) and of heat diffusion across the sample: the spatial resolution is effectively limited to the mm range, thereby hampering the successful exploitation of conventional infrared thermography for microscale imaging applications. Furthermore, the impact of the technique is reduced by the difficulty to obtain space-resolved measurements of any thermal property other than temperature: current implementations of infrared thermography do not easily convert temperature maps into images of the sample thermal properties (e.g., the thermal conductivity), which would be beneficial instead for a variety of applications ranging from the optimization of thermoelectric and optoelectronic components to the development of heat transfer models for biological soft materials for disease diagnosis and hyperthermia-based therapeutics.

Both the major flaws of state-of-the-art infrared imaging have been tackled in this doctoral work. At first, I have focused on the spatial resolution. I have developed, implemented and experimentally validated a novel super-resolution photo-thermal image acquisition approach, capable of overcoming the diffraction barrier and of producing a nearly twenty-time enhancement relatively to the μm spatial resolution of the thermal camera in its conventional operation. To this aim the method, which has been extensively described in chapter 2, exploits the automated sub-diffraction centroid localization of sparse temperature increments primed by modulated raster-scanned focused laser light.

Following the design, construction and optimization of the experimental setup, custom-designed reference ink samples have been exploited to perform the first proof-of-principle super-resolution imaging experiments. By the comparison with the results of transmitted-light microscopy I have demonstrated accurate imaging capability, and I have confirmed the tunability of the achieved spatial resolution depending on the signal-to-noise ratio of the thermal-camera frames and the excitation laser spot size. With detected pixel-averaged temperature increments of few degrees, a sub-diffraction 10-50 μm resolution can now be routinely achieved over mm^2- to cm^2- sized fields of view.

The achieved spatial resolution has allowed reconstructing the spatial distribution of photo-thermal 30-nm nanocubes inside murine skin biopsies in a first exemplary application of the proposed imaging approach to biological samples. Then, biological application of super-resolved thermography has been fully demonstrated on B16 murine melanoma biopsies, where melanin pigments have been quantified and spatially mapped at 40-μm resolution across entire tissue sections.

The endogenous photo-thermal effect primed by melanin absorption of visible laser light has allowed to image melanin with no need for labeling, and the specificity of photo-thermal imaging in the identification of melanin has been confirmed by complementary hematoxylin-eosin staining of the same excised tissue sections. Importantly, by the combination of finite-element simulations with the analytical/numerical solution of the 3D heat equation, I have provided the necessary theoretical framework and proposed the data-analysis protocol to convert temperature-based images into quantitative super-resolution maps of the absolute molar concentration of melanin pigments. Molar concentrations in the $\sim$ 0.001-0.05 M range have been recovered, with a 5×10^{-4} M lower limit of detection: such a concentration threshold, which is assigned by the adopted 30-mW laser power and by the 0.1-K thermo-camera sensitivity, proves sufficient to investigate the typical melanin concentrations reported in the literature for human melanoma.

With the extraction of absolute concentration values from the amplitudes of laser-primed temperature increments sensed by the thermal camera, the results presented in chapter 3 highlight that super-resolution thermography is not limited to morphological imaging: structural information on the sample can be retrieved as well. Along the same research line, efforts have been devoted in chapter 4 to the quantification and spatial mapping of thermal conductivity values. A novel procedure has been outlined to quantify and image absolute thermal conductivities over the three decades 0.1-100 W/mK on both thermally thick and thermally thin solid slabs by photo-activated thermal imaging. The importance of the results is at least twofold. On the one hand, I have shown that the product of the amplitude and characteristic exponential rise time of the temperature variations primed by focused laser-light illumination obeys an inverse proportionality on the sample thermal conductivity, irrespective of density and specific heat capacity. I have provided theoretical justification for such a universal dependence based on Fourier's heat transfer law, and I have validated it by both the approximated analytical solution of the 3D heat equation and finite-element numerical simulations in the presence of convective and radiative losses. On the other hand, results bear experimental relevance since they allow a direct procedure for the retrieval of thermal conductivity values, once the sample thickness is known.

The feasibility of space-resolved measurements has been validated on historical tin-rich organ pipe fragments, where the product of the sample thickness and thermal conductivity, imaged at 40-μm resolution, has been pointed out as a relevant parameter for the non-destructive characterization of the sample conservation state. The results I have obtained on historical organ pipes suggest potential impact in the context of archeometallurgical studies aimed at the nondestructive characterization of the morphology and thermal properties of cultural heritage artifacts.

Near-future efforts will be directed towards a reduction of the imaging time, which currently represents in my opinion the main limitation of super-resolution thermography. Similarly to the case of the fluorescence-based super-resolution techniques (e.g., PALM and STORM) that rely on a stochastic molecular switching and readout, a long data acquisition time is imposed by the necessity of laser-scanning the sample to induce sequences of isolated temperature increments. A 4x2-mm^2 area can be scanned with 40-μm pixel size in about 90 minutes, and this time reduces to 20 minutes with 75-μm pixel size: overall, the total data acquisition time requires a compromise between the size of the imaged region, the scan pixel size and the amplitude of temperature signals at the given illumination time τ_{on} (i.e., the required spatial resolution). I reason that the current imaging time can

be shortened by multi-spot illumination (via a Spatial Light Modulator) and/or by relaxing the constraint on the observation of individual, isolated temperature peaks. Algorithms based on deep-learning, sequential fitting, sparsity, or maximum-likelihood estimation allow handling multiple and overlapping signal peaks, and could be adopted to speed up the imaging process. In principle, the imaging time could also be reduced by the exploitation of high-speed infrared thermal cameras capable of reaching 1 kHz frame rate and of properly sampling shorter temperature kinetics: provided higher laser powers are employed, the laser activation time τ_{on} could be reduced, resulting in an overall shorter total data acquisition time.

Along with the reduction of the imaging time, I reason that a natural extension of the super-resolution imaging method that I have presented here consists in the extraction of light-induced temperature depth profiles in the sample. Numerical methods, which have been extended from the field of photo-acoustic imaging to photo-thermal tomography, rely on the solution of the inverse problem of heat diffusion and could allow reconstructing the laser-primed temperature field in three dimensions [119]. Even in the presence of scattering biological tissues, a tomographic image of light-absorbing entities in the sample could in principle be derived starting from the surface signal collected by the thermal camera.

I finally remark that, by taking advantage of externally-induced temperature variations, the proposed super-resolution image acquisition necessarily requires an excitation laser wavelength lying within the sample absorption band, and a pronounced sample efficiency of heat release upon laser-light absorption. Such a requirement can be fulfilled either by exogenous photo-thermal contrast agents (e.g., photo-thermal nanoparticles as in chapter 2 of the present work), or by taking advantage of the endogenous sample photo-thermal signal in a label-free configuration: plenty of examples have been reported here, with ink-printed polyester samples in chapter 2, melanin pigments in murine melanoma biopsies in chapter 3 and tin-rich organ pipe fragments in chapter 4. Broad application of the proposed approach can therefore be envisioned in the non-invasive testing of materials in all branches of the applied physical and life sciences.

Publications and Collaborations

Portions of this Ph.D. thesis have been published in:

1. Bouzin, M.*, **Marini, M.***, Zeynali, A., Borzenkov, M., Sironi, L., D'Alfonso, L., Mingozzi, F., Granucci, F., Pallavicini, P., Chirico, G., Collini, M. *Photo-Activated Raster Scanning Thermal Imaging at Sub-Diffraction Resolution*, Nat. commun. 10:5523 (2019)
   * co-first authors

2. Zeynali, A., **Marini, M.**, Bouzin, M., Borzenkov, M., Sironi, L., D'Alfonso, L., Pallavicini, P., Cassina, V., Mantegazza, F., Granucci, F., Marongiu, L., Polli, D., De La Cadena Perez, A., Collini, M., Chirico, G. *Multiphoton Fabrication of Proteinaceous Nanocomposite Microstructures with Photothermal Activity in the Infrared*, Adv. Optical Mater. 2000584 (2020)

3. **Marini, M.**, Bouzin, M., Sironi, L., D'Alfonso, L., Colombo, R., Di Martino, D., Gorini, G., Collini, M., Chirico, G. *A novel method for spatially-resolved thermal conductivity measurement by super-resolution photo-activated infrared imaging*, Mater. Today Phys. 18, 100375 (2021)

4. Zeynali, A., **Marini, M.**, Collini, M., Bouzin, M., Sironi, L., D'Alfonso, L., Pallavicini, P., Chirico, G. *Multiphoton Fabrication of flexible photo-thermally active proteinaceous microstructures*, Chem. Eng. Trans. 84, 235-240 (2021)

5. Bouzin, M., Zeynali, A., **Marini, M.**, Sironi, L., Scodellaro, R., D'Alfonso, L., Collini, M., Chirico, G. *Multiphoton Laser Fabrication of Hybrid Photo-Activable Biomaterials*, Sensors, 21, 5891 (2021)

6. Bouzin, M.*, **Marini, M.***, Chirico, G., Granucci, F., Mingozzi, F., Colombo, R., D'Alfonso, L., Sironi, L., Collini, M. *Melanin Concentration Maps by Label-free*

Super-resolution Photo-thermal Imaging on Melanoma Biopsies, Under Revision (2021)
* co-first authors

Closely related conference contributions include:

1. Bouzin, M.; **Marini, M.**; Zeynali, A.; Sironi, L.; D'Alfonso, L.; Mingozzi, F.; Granucci, F.; Chirico, G.; Collini, M. *Photo-Activated Thermal Imaging at Sub-Diffraction Resolution*, SPIE Optical Metrology Conference (June 2019, Munich, Germany)

2. **Marini, M.**; Bouzin, M.; Zeynali, A.; Sironi, L.; D'Alfonso, L.; Chirico, G.; Collini, M. *Measurement of space-dependent thermal diffusivities by photo-activated thermography*, 20th International Conference on Photoacoustic and Photothermal Phenomena (July 2019, Moscow, Russia)

3. Bouzin, M.; **Marini, M.**; Zeynali, A.; Sironi, L.; D'Alfonso, L.; Mingozzi, F.; Granucci, F.; Pallavicini, P.; Chirico, G.; Collini, M. *Super-Resolution Imaging by Sub-Diffraction Localization of Laser-Primed Temperature Variations*, 20th International Conference on Photoacoustic and Photothermal Phenomena (July 2019, Moscow, Russia)

4. **Marini, M.**; Bouzin, M.; Zeynali, A.; Sironi, L.; D'Alfonso, L.; Mingozzi, F.; Granucci, F.; Pallavicini, P.; Chirico, G.; Collini, M. *Super-Resolution Photo-Activated Thermography*, 12th EBSA/10th ICBP-IUPAB Congress (July 2019, Madrid, Spain)

5. Bouzin, M.; **Marini, M.**; Zeynali, A.; Sironi, L.; D'Alfonso, L.; Mingozzi, F.; Granucci, F.; Pallavicini, P.; Chirico, G.; Collini, M. *Thermal Imaging by Sub-Diffraction Localization of Photo-Activated Absorbers*, 20th FisMat 2019 (October 2019, Catania, Italy)

6. Bouzin, M.; **Marini, M.**; Zeynali, A.; Borzenkov, M.; Sironi, L.; D'Alfonso, L.; Mingozzi, F.; Granucci, F.; Pallavicini, P.; Chirico, G.; Collini, M. *Nanoparticles Localization in Tissues at Sub-Diffraction Level by Infrared Thermal Imaging*, Nano-Day IV (December 2019, Milano, Italy)

7. Bouzin, M.; **Marini, M.**; Zeynali, A.; Borzenkov, M.; Sironi, L.; D'Alfonso, L.; Mingozzi, F.; Granucci, F.; Chirico, G.; Collini, M. *Photo-Activated Thermal Imaging at Sub-Diffraction Resolution*, 64th Biophysical Society Annual Meeting (February 2020, San Diego, California, USA)

8. **Marini, M.**; Bouzin, M.; Zeynali, A.; Sironi, L.; D'Alfonso, L.; Mingozzi, F.; Granucci, F.; Chirico, G.; Collini, M. *Label-Free Super-Resolution Photo-Thermal Imaging on Melanoma Biopsies*, 65th Biophysical Society Annual Meeting (February 2021, Boston, USA)

9. Zeynali, A.; **Marini, M.**; Bouzin, M.; Collini, M.; Chirico, G. *Direct Laser Writing of Photothermally Active Proteinaceous Microarchitectures*, Design and Function of Responsive Nanocomposites (May 2021, Dublin, Ireland)

10. Zeynali, A.; **Marini, M.**;Bouzin, M.; Pallavicini, P.; Collini, M.; Chirico, G. *Laser-Assisted Structuration of Photothermally Responsive Proteinaceous Microarchitectures*, Research and Nanomedicine Workshop (June 2021, Pavia, Italy)

11. **Marini, M.**; Zeynali, A.; Bouzin, M.; Sironi, L.; D'Alfonso, L.; Pallavicini, P.; Collini, M.; Chirico, G. *Development and Characterization of Proteinaceous Multiphoton-Fabricated Microstructures with Photo-Thermal Functionality*, SPIE Optical Metrology Conference (June 2021, Munich, Germany)

12. **Marini, M.**; *Photo-Activated Raster Scanning Thermal Imaging at Sub-Diffraction Resolution*, XXV SIBPA National Congress (June-July 2021, Parma, Italy)

13. Chirico, G.; Conci, C.; Sironi, L.; Raimondi, M.; Jacchetti, E.; Cerullo, G.; Osellame, R.; **Marini, M.**; Zeynali, A.; D'Alfonso, L.; Bouzin, M.; Collini, M. *Laser fabrication of active micro-structures for cellular biology*, European Optical Society Annual Meeting (EOSAM) 2021 (September 2021, Roma, Italy)

14. Bouzin, M.; **Marini, M.**; Sironi, L.; D'Alfonso, L.; Colombo, R.; Di Martino, D.; Gorini, G.; Chirico, G.; Collini, M. *Thermal Conductivity Imaging on Cultural Heritage Artifacts by Super-Resolution Thermography*, International School of Quantum Electronics, 64th Course: Progress in Photoacoustic & Photothermal Phenomena (October 2021, Erice, Italy)

15. **Marini, M.**; Bouzin, M.; Sironi, L.; D'Alfonso, L.; Colombo, R.; Mingozzi, F.; Granucci, F.; Collini, M.; Chirico, G. *Label-Free Super-Resolution Thermography as a Tool to Image Melanin in Melanoma Biopsies*, International School of Quantum Electronics, 64th Course: Progress in Photoacoustic & Photothermal Phenomena (October 2021, Erice, Italy)

I finally acknowledge the precious help of the research groups actively collaborating with the Biophotonics and Biophysics group of Università degli Studi di Milano-Bicocca. I especially thank Prof. Francesca Granucci and Dr. Francesca Mingozzi (Biotechnology and Biosciences Department, Università degli Studi di Milano-Bicocca) for providing access to the murine skin and melanoma biopsies, and Prof. Roberto Colombo for giving me access to the FLIR T650sc thermal camera. I am also particularly grateful to Prof. Piersandro Pallavicini (General Chemistry Department, Università degli Studi di Pavia) for the synthesis of Prussian Blue nanoparticles, to Prof. G. Crosta and Dr. S. Basiricò (Department of Earth and Environmental Sciences, Università degli Studi di Milano-Bicocca) for kindly providing nylon and poly-oxymethylene samples and for performing transient-line-source thermal conductivity measurements. A special thank to Prof. Giuseppe Gorini and Dr. Daniela Di Martino (Physics Department, Università degli Studi di Milano-Bicocca) for introducing me to the field of cultural heritage conservation and to Claudio Bonizzi and Curzio Merlo for the loan of the organ pipe fragment. Finally, a personal thank to Andrea Passerini and Alessandro Baù for the precious help with the electronic components of the photo-thermal imaging setup.

Bibliography

1. Vollmer, M. & Möllmann, K. P. *Infrared thermal imaging: Fundamentals, research and applications* (Wiley-Vch, 2017).
2. Planck, M. Zur Theorie des Gesetzes der Energieverteilung im Normalspektrum. *Verhandl. Dtsch. Phys. Ges.* **2,** 237–245 (1900).
3. Vollmer, M. Newton's law of cooling revisited. *Eur. J. Phys.* **30,** 1063–1084 (2009).
4. Ogi, H. *et al.* Thermal Mode Spectroscopy for Thermal Diffusivity of Millimeter-Size Solids. *Phys. Rev. Lett.* **117,** 195901 (2016).
5. Philipp, A. *et al.* Direct measurement of the in-plane thermal diffusivity of semitransparent thin films by lock-in thermography: An extension of the slopes method. *Anal. Chem.* **91,** 8476–8483 (2019).
6. Incropera, F. P., DeWitt, D. P., Bergman, T. L. & Lavine, A. S. *Fundamentals of Heat and Mass Transfer* (Wiley-Vch, 2011).
7. Gao, Y. & Tian, G. Y. Emissivity correction using spectrum correlation of infrared and visible images. *Sens. Actuators, A* **270,** 8–17 (2018).
8. Gaussorgues, G. *Infrared Thermography* (Springer, 1994).
9. Flir. *User's manual: FLIR Exx series* (2010).
10. Budzier, H. & Gerlach, G. *Thermal Infrared Sensors: Theory, Optimisation and Practice* (Wiley-Vch, 2011).
11. Maldague, X. *Theory and practice of infrared technology for nondestructive testing* (Wiley-Vch, 2001).
12. Sakagami, T. & Kubo, S. Applications of pulse heating thermography and lock-in thermography to quantitative nondestructive evaluations. *Infrared Phys. Technol.* **43,** 211–218 (2002).

13. Meola, C., Carlomagno, G. M., Squillace, A. & Vitiello, A. Non-destructive evaluation of aerospace materials with lock-in thermography. *Eng. Fail. Anal.* **13,** 380–388 (2006).
14. Muzika, L., Švantner, M. & Kučera, M. Lock-in and pulsed thermography for solar cell testing. *Appl. Opt.* **57,** 90–97 (2018).
15. Benítez, H. D. *et al.* Definition of a new thermal contrast and pulse correction for defect quantification in pulsed thermography. *Infrared Phys. Technol.* **51,** 160–167 (2008).
16. Weiser, M., Röllig, M., Arndt, R. & Erdmann, B. Development and test of a numerical model for pulse thermography in civil engineering. *Heat Mass Transf.* **46,** 1419–1428 (2010).
17. Bäuerle, D. *Laser Processing and Chemistry* (Springer, 2011).
18. Goodman, J. W. *Introduction to Fourier optics* (W.H. Freeman, 2017).
19. Hecht, E. *Optics* (Addison-Wesley, 2001).
20. Mertz, J. *Introduction to Optical Microscopy* (Cambridge University Press, 2019).
21. Okabe, T. *et al.* First-in-human clinical study of novel technique to diagnose malignant melanoma via thermal conductivity measurements. *Sci. Rep.* **9,** 3853 (2019).
22. Herman, C. The role of dynamic infrared imaging in melanoma diagnosis. *Expert Rev. Dermatol.* **8,** 177–184 (2013).
23. Lapierre-Landry, M., Gordon, A. Y., Penn, J. S. & Skala, M. C. In vivo photothermal optical coherence tomography of endogenous and exogenous contrast agents in the eye. *Sci. Rep.* **7,** 9228 (2017).
24. He, J. *et al.* Noninvasive, label-free, three-dimensional imaging of melanoma with confocal photothermal microscopy: Differentiate malignant melanoma from benign tumor tissue. *Sci. Rep.* **6,** 30209 (2016).
25. Kobayashi, T., Nakata, K., Yajima, I., Kato, M. & Tsurui, H. Label-free imaging of melanoma with confocal photothermal microscopy: Differentiation between malignant and benign tissue. *Bioengineering* **5,** 67 (2018).
26. Christofferson, J. *et al.* Microscale and nanoscale thermal characterization techniques. *J. Electron. Packag.* **130,** 0411011 (2008).
27. Farzaneh, M. *et al.* CCD-based thermoreflectance microscopy: Principles and applications. *J. Phys. D. Appl. Phys.* **42,** 143001 (2009).

28. Ciampa, F., Mahmoodi, P., Pinto, F. & Meo, M. Recent advances in active infrared thermography for non-destructive testing of aerospace components. *Sensors* **18,** 609 (2018).

29. Maldague, X. P. V. *Nondestructive Evaluation of Materials by Infrared Thermography* (Springer, 1993).

30. Okabe, K. *et al.* Intracellular temperature mapping with a fluorescent polymeric thermometer and fluorescence lifetime imaging microscopy. *Nat. Commun.* **3,** 705 (2012).

31. Donner, J. S., Thompson, S. A., Kreuzer, M. P., Baffou, G. & Quidant, R. Mapping intracellular temperature using green fluorescent protein. *Nano Lett.* **12,** 2107–2111 (2012).

32. Freddi, S. *et al.* A molecular thermometer for nanoparticles for optical hyperthermia. *Nano Lett.* **13,** 2004–2010 (2013).

33. Löw, P., Kim, B., Takama, N. & Bergaud, C. High-spatial-resolution surface-temperature mapping using fluorescent thermometry. *Small* **4,** 908–914 (2008).

34. Williams, C. C. & Wickramasinghe, H. K. Scanning thermal profiler. *Appl. Phys. Lett.* **49,** 1587–1589 (1986).

35. Majumdar, A. Scanning thermal microscopy. *Annu. Rev. Mater. Sci.* **29,** 505–585 (1999).

36. Nakabeppu, O. & Suzuki, T. Microscale temperature measurement by scanning thermal microscopy. *J. Therm. Anal. Calorim.* **69,** 727–737 (2002).

37. Desiatov, B., Goykhman, I. & Levy, U. Direct temperature mapping of nanoscale plasmonic devices. *Nano Lett.* **14,** 648–652 (2014).

38. Pollock, H. M. & Hammiche, A. Micro-thermal analysis: Techniques and applications. *J. Phys. D. Appl. Phys.* **34,** R23 (2001).

39. Rosencwaig, A., Opsal, J., Smith, W. L. & Willenborg, D. L. Detection of thermal waves through optical reflectance. *Appl. Phys. Lett.* **46,** 1013–1015 (1985).

40. Pottier, L. Micrometer scale visualization of thermal waves by photoreflectance microscopy. *Appl. Phys. Lett.* **64,** 1618–1619 (1994).

41. Kim, D. U., Park, K. S., Jeong, C. B., Kim, G. H. & Chang, K. S. Quantitative temperature measurement of multi-layered semiconductor devices using spectroscopic thermoreflectance microscopy. *Opt. Express* **24,** 13906 (2016).

42. Gaiduk, A., Ruijgrok, P. V., Yorulmaz, M. & Orrit, M. Detection limits in photothermal microscopy. *Chem. Sci.* **1,** 343–350 (2010).

43. Miyazaki, J. & Kobayahsi, T. Photothermal microscopy for high sensitivity and high resolution absorption contrast imaging of biological tissues. *Photonics* **4** (2017).

44. Berciaud, S., Lasne, D., Blab, G. A., Cognet, L. & Lounis, B. Photothermal heterodyne imaging of individual metallic nanoparticles: Theory versus experiment. *Phys. Rev. B* **73,** 045424 (2006).

45. Vermeulen, P., Cognet, L. & Lounis, B. Photothermal microscopy: Optical detection of small absorbers in scattering environments. *J. Microsc.* **254,** 115–121 (2014).

46. Pierścińska, D. Thermoreflectance spectroscopy - Analysis of thermal processes in semiconductor lasers. *J. Phys. D. Appl. Phys.* **51,** 013001 (2018).

47. Tomko, J. A. *et al.* Tunable thermal transport and reversible thermal conductivity switching in topologically networked bio-inspired materials. *Nat. Nanotechnol. 2018 1310* **13,** 959–964 (2018).

48. Foley, B. M. *et al.* Protein thermal conductivity measured in the solid state reveals anharmonic interactions of vibrations in a fractal structure. *J. Phys. Chem. Lett.* **5,** 1077–1082 (2014).

49. Yang, J., Maragliano, C. & Schmidt, A. J. Thermal property microscopy with frequency domain thermoreflectance. *Rev. Sci. Instrum.* **84,** 104904 (2013).

50. Usamentiaga, R. *et al.* Infrared thermography for temperature measurement and non-destructive testing. *Sensors* **14,** 12305–12348 (2014).

51. Ball, M. & Pinkerton, H. Factors affecting the accuracy of thermal imaging cameras in volcanology. *J. Geophys. Res.* **111,** 11203 (2006).

52. Lahiri, B. B., Bagavathiappan, S., Jayakumar, T. & Philip, J. Medical applications of infrared thermography: A review. *Infrared Phys. Technol.* **55,** 221–235 (2012).

53. Bagavathiappan, S., Lahiri, B. B., Saravanan, T., Philip, J. & Jayakumar, T. Infrared thermography for condition monitoring - A review. *Infrared Phys. Technol.* **60,** 35–55 (2013).

54. Gresil, M., Wang, Z., Poutrel, Q. A. & Soutis, C. Thermal Diffusivity Mapping of Graphene Based Polymer Nanocomposites. *Sci. Rep.* **7,** 5536 (2017).

55. Burgholzer, P., Berer, T., Gruber, J. & Mayr, G. Super-resolution thermographic imaging using blind structured illumination. *Appl. Phys. Lett.* **111,** 031908 (2017).

56. Ruthardt, N., Lamb, D. C. & Bräuchle, C. Single-particle tracking as a quantitative microscopy-based approach to unravel cell entry mechanisms of viruses and pharmaceutical nanoparticles. *Mol. Ther.* **19,** 1199–1211 (2011).

57. Yildiz, A. *et al.* Myosin V walks hand-over-hand: Single fluorophore imaging with 1.5-nm localization. *Science (80-.).* **300,** 2061–2065 (2003).

58. Betzig, E. *et al.* Imaging intracellular fluorescent proteins at nanometer resolution. *Science (80-.).* **313,** 1642–1645 (2006).

59. Rust, M. J., Bates, M. & Zhuang, X. Sub-diffraction-limit imaging by stochastic optical reconstruction microscopy (STORM). *Nat. Methods* **3,** 793–795 (2006).

60. Bouzin, M. *et al.* Photo-activated raster scanning thermal imaging at sub-diffraction resolution. *Nat. Commun.* **10,** 1–9 (2019).

61. Dacarro, G. *et al.* Self-assembled monolayers of Prussian blue nanoparticles with photothermal effect. *Supramol. Chem.* **29,** 823–833 (2017).

62. Dacarro, G., Taglietti, A. & Pallavicini, P. Prussian blue nanoparticles as a versatile photothermal tool. *Molecules* **23** (2018).

63. Thompson, R. E., Larson, D. R. & Webb, W. W. Precise nanometer localization analysis for individual fluorescent probes. *Biophys. J.* **82,** 2775–2783 (2002).

64. Stelzer, E. H. Contrast, resolution, pixelation, dynamic range and signal-to-noise ratio: Fundamental limits to resolution in fluorescence light microscopy. *J. Microsc.* **189,** 15–24 (1998).

65. Mortola, J. P. Thermographic analysis of body surface temperature of mammals. *Zoolog. Sci.* **30,** 118–124 (2013).

66. Polymeropoulos, E. T., Oelkrug, R. & Jastroch, M. The evolution of endothermy - from patterns to mechanisms. *Front. Physiol.* **9,** 891 (2018).

67. Zhuang, X. Nano-imaging with STORM. *Nat. Photonics* **3,** 365–367 (2009).

68. Ouyang, W., Aristov, A., Lelek, M., Hao, X. & Zimmer, C. Deep learning massively accelerates super-resolution localization microscopy. *Nat. Biotechnol.* **36,** 460–468 (2018).

69. Huang, F., Schwartz, S. L., Byars, J. M. & Lidke, K. A. Simultaneous multiple-emitter fitting for single molecule super-resolution imaging. *Biomed. Opt. Express* **2,** 1377 (2011).

70. Nehme, E., Weiss, L. E., Michaeli, T. & Shechtman, Y. Deep-STORM: super-resolution single-molecule microscopy by deep learning. *Optica* **5,** 458 (2018).

71. He, Y. *et al.* Ghost imaging based on deep learning. *Sci. Rep.* **8,** 6469 (2018).

72. Shain, A. H. & Bastian, B. C. From melanocytes to melanomas. *Nat. Rev. Cancer* **16,** 345–358 (2016).

73. Sarna, M., Krzykawska-Serda, M., Jakubowska, M., Zadlo, A. & Urbanska, K. Melanin presence inhibits melanoma cell spread in mice in a unique mechanical fashion. *Sci. Rep.* **9,** 1–9 (2019).

74. Lin, J. Y. & Fisher, D. E. Melanocyte biology and skin pigmentation. *Nature* **445,** 843–850 (2007).

75. Wang, J. X., Fukunaga-Kalabis, M. & Herlyn, M. Crosstalk in skin: melanocytes, keratinocytes, stem cells, and melanoma. *J. Cell Commun. Signal.* **10,** 191–196 (2016).

76. Sung, H. *et al.* Global Cancer Statistics 2020: GLOBOCAN Estimates of Incidence and Mortality Worldwide for 36 Cancers in 185 Countries. *CA. Cancer J. Clin.* **71,** 209–249 (2021).

77. Kuzu, F., Nguyen, F. D., Noory, M. A. & Sharma, A. Current State of Animal (Mouse) Modeling in Melanoma Research. *Cancer Growth Metastasis* **8,** 81–94 (2015).

78. Forsea, A.-M. Melanoma Epidemiology and Early Detection in Europe: Diversity and Disparities. *Dermatol. Pract. Concept.* **10,** e2020033 (2020).

79. Chan, J. K. The wonderful colors of the hematoxylin-eosin stain in diagnostic surgical pathology. *Int. J. Surg. Pathol.* **22,** 12–32 (2014).

80. Matthews, T. E., Piletic, I. R., Selim, M. A., Simpson, M. J. & Warren, W. S. Pump-probe imaging differentiates melanoma from melanocytic nevi. *Sci. Transl. Med.* **3** (2011).

81. Guo, S. *et al.* Multimodal image analysis in tissue diagnostics for skin melanoma. *J. Chemom.* **32,** 1–17 (2018).

82. Scodellaro, R. *et al.* Whole-section tumor micro-architecture analysis by a two-dimensional phasor-based approach applied to polarization-dependent second harmonic imaging. *Front. Oncol.* **9,** 1–14 (2019).

83. Slominski, R. M., Zmijewski, M. A. & Slominski, A. T. The role of melanin pigment in melanoma. *Exp. Dermatol.* **24,** 258–259 (2015).

84. Grieco, C., Kohl, F. R., Hanes, A. T. & Kohler, B. Probing the heterogeneous structure of eumelanin using ultrafast vibrational fingerprinting. *Nat. Commun.* **11,** 1–9 (2020).

85. Fu, D., Ye, T., Matthews, T. E., Yurtsever, G. & Warren, W. S. Two-color, two-photon, and excited-state absorption microscopy. *J. Biomed. Opt.* **12,** 054004 (2007).

86. Brozyna, A. A., Jóźwicki, W., Carlson, J. A. & Slominski, A. T. Melanogenesis affects overall and disease-free survival in patients with stage III and IV melanoma. *Hum. Pathol.* **44,** 2071–2074 (2013).

87. Brozyna, A. A., Józwicki, W., Roszkowski, K., Filipiak, J. & Slominski, A. T. Melanin content in melanoma metastases affects the outcome of radiotherapy. *Oncotarget* **7,** 17844–17853 (2016).

88. Slominski, A. *et al.* The role of melanogenesis in regulation of melanoma behavior: Melanogenesis leads to stimulation of HIF-1α expression and HIF-dependent attendant pathways. *Arch. Biochem. Biophys.* **563,** 79–93 (2014).

89. Chung, S., Lim, G. J. & Lee, J. Y. Quantitative analysis of melanin content in a three-dimensional melanoma cell culture. *Sci. Rep.* **9,** 1–9 (2019).

90. Fernandes, B., Matamá, T., Guimarães, D., Gomes, A. & Cavaco-Paulo, A. Fluorescent quantification of melanin. *Pigment Cell Melanoma Res.* **29,** 707–712 (2016).

91. Ito, S. & Jimbow, K. Quantitative analysis of eumelanin and pheomelanin in hair and melanomas. *J. Invest. Dermatol.* **80,** 268–272 (1983).

92. Sun, C.-K. *et al.* Slide-free clinical imaging of melanin with absolute quantities using label-free third-harmonic-generation enhancement-ratio microscopy. *Biomed. Opt. Express* **11,** 3009 (2020).

93. Huang, Z. *et al.* Raman spectroscopy of in vivo cutaneous melanin. *J. Biomed. Opt.* **9,** 1198 (2004).

94. Godechal, Q., Ghanem, G. E., Cook, M. G. & Gallez, B. Electron paramagnetic resonance spectrometry and imaging in melanomas: Comparison between pigmented and nonpigmented human malignant melanomas. *Mol. Imaging* **12,** 218–223 (2013).

95. Dimitrow, E. *et al.* Spectral fluorescence lifetime detection and selective melanin imaging by multiphoton laser tomography for melanoma diagnosis. *Exp. Dermatol.* **18,** 509–515 (2009).

96. Guida, S. *et al.* Clinical Applications of In Vivo and Ex Vivo Confocal Microscopy. *Appl. Sci.* **11,** 1979 (2021).

97. Malvehy, J. *et al.* Ex vivo confocal microscopy: revolution in fast pathology in dermatology. *Br. J. Dermatol.* **183,** 1011–1025 (2020).

98. Fu, D. *et al.* Probing skin pigmentation changes with transient absorption imaging of eumelanin and pheomelanin. *J. Biomed. Opt.* **13,** 054036 (2008).

99. He, J., Miyazaki, J., Wang, N. & Kobayashi, T. Label-free imaging of melanoma with nonlinear photothermal microscopy. *Opt. Lett.* **40,** 1141–1144 (2015).

100. Han, X., Lui, H., McLean, D. I. & Zeng, H. Near-infrared autofluorescence imaging of cutaneous melanins and human skin in vivo. *J. Biomed. Opt.* **14,** 024017 (2009).

101. Kalia, S. *et al.* Melanin quantification by in vitro and in vivo analysis of near-infrared fluorescence. *Pigment Cell Melanoma Res.* **31,** 31–38 (2018).

102. Marini, M. *et al.* A novel method for spatially-resolved thermal conductivity measurement by super-resolution photo-activated infrared imaging. *Mater. Today Phys.* **18,** 100375 (2021).

103. Potez, M. *et al.* Characterization of a B16-F10 melanoma model locally implanted into the ear pinnae of C57BL/6 mice. *PLoS One* **13,** 1–19 (2018).

104. Smolle, J., Hofmann-Wellenhof, R., Soyer, H. P., Stettner, H. & Kerl, H. Nuclear size and shape parameters correlate with proliferative activity in cutaneous melanocytic tumors. *J. Invest. Dermatol.* **93,** 178–182 (1989).

105. Bernard, V., Staffa, E., Mornstein, V. & Bourek, A. Infrared camera assessment of skin surface temperature - Effect of emissivity. *Phys. Medica* **29,** 583–591 (2013).

106. Schindelin, J. *et al.* Fiji: An open-source platform for biological-image analysis. *Nat. Methods* **9,** 676–682 (2012).

107. Riesz, J., Gilmore, J. & Meredith, P. Quantitative scattering of melanin solutions. *Biophys. J.* **90,** 4137–4144 (2006).

108. Meredith, P. & Riesz, J. Radiative Relaxation Quantum Yields for Synthetic Eumelanin. *Photochem. Photobiol.* **79,** 211 (2004).

109. Ansari, M. A. & Mohajerani, E. Mechanisms of laser-tissue interaction: I. Optical properties of tissue. *J. Lasers Med. Sci.* **2,** 119–125 (2011).

110. Piletic, I. R., Matthews, T. E. & Warren, W. S. Estimation of molar absorptivities and pigment sizes for eumelanin and pheomelanin using femtosecond transient absorption spectroscopy. *J. Chem. Phys.* **131,** 1–4 (2009).

111. Shu, X., Li, H., Dong, B., Sun, C. & Zhang, H. F. Quantifying melanin concentration in retinal pigment epithelium using broadband photoacoustic microscopy. *Biomed. Opt. Express* **8,** 2851 (2017).

112. Fukuda, M. Lysosome-Related Organelles. *Encycl. Cell Biol.* **2,** 235–242 (2016).

113. Liu, Y. *et al.* Comparisons of the Structural and Chemical Properties of Melanosomes Isolated from Retinal Pigment Epithelium, Iris and Choroid of Newborn and Mature Bovine Eyes. *Photochem. Photobiol.* **81,** 510 (2005).

114. Carriel, V. S. *et al.* A novel histochemical method for a simultaneous staining of melanin and collagen fibers. *J. Histochem. Cytochem.* **59,** 270–277 (2011).

115. Hult, J. *et al.* Comparison of photoacoustic imaging and histopathological examination in determining the dimensions of 52 human melanomas and nevi ex vivo. *Biomed. Opt. Express* **12,** 4097 (2021).

116. Meglinski, I. V. & Matcher, S. J. Quantitative assessment of skin layers absorption and skin reflectance spectra simulation in the visible and near-infrared spectral regions. *Physiol. Meas.* **23,** 741–753 (2002).

117. Ring, E. F. & Ammer, K. Infrared thermal imaging in medicine. *Physiol. Meas.* **33,** 33–46 (2012).

118. Santa Cruz, G. A. *et al.* Dynamic infrared imaging of cutaneous melanoma and normal skin in patients treated with BNCT. *Appl. Radiat. Isot.* **67,** 54–58 (2009).

119. Telenkov, S. A., Tanenbaum, B. S., Goodman, D. M., Nelson, J. S. & Milner, T. E. In vivo infrared tomographic imaging of laser-heated blood vessels. *IEEE J. Sel. Top. Quantum Electron.* **5,** 1193–1199 (1999).

120. Toberer, E. S., Baranowski, L. L. & Dames, C. Advances in thermal conductivity. *Annu. Rev. Mater. Res.* **42,** 179–209 (2012).

121. Webb, R. C. *et al.* Ultrathin conformal devices for precise and continuous thermal characterization of human skin. *Nat. Mater.* **12,** 938–944 (2013).

122. Wang, H., Chu, W. & Chen, G. A Brief Review on Measuring Methods of Thermal Conductivity of Organic and Hybrid Thermoelectric Materials. *Adv. Electron. Mater.* **5** (2019).

123. Zhu, T., Olson, D. H., Hopkins, P. E. & Zebarjadi, M. Heat diffusion imaging: In-plane thermal conductivity measurement of thin films in a broad temperature range. *Rev. Sci. Instrum.* **91** (2020).

124. Olson, D. H., Braun, J. L. & Hopkins, P. E. Spatially resolved thermoreflectance techniques for thermal conductivity measurements from the nanoscale to the mesoscale. *J. Appl. Phys.* **126** (2019).

125. Jiang, P., Qian, X. & Yang, R. Tutorial: Time-domain thermoreflectance (TDTR) for thermal property characterization of bulk and thin film materials. *J. Appl. Phys.* **124** (2018).

126. Stoib, B. *et al.* Spatially resolved determination of thermal conductivity by Raman spectroscopy. *Semicond. Sci. Technol.* **29** (2014).

127. Laraoui, A. *et al.* Imaging thermal conductivity with nanoscale resolution using a scanning spin probe. *Nat. Commun.* **6** (2015).

128. Yue, S. *et al.* Photoluminescence mapping and time-domain thermo photoluminescence for rapid imaging and measurement of thermal conductivity of boron arsenide. *Mater. Today Phys.* **13** (2020).

129. Cahill, D. G. Thermal conductivity measurement from 30 to 750 K: The 3ω method. *Rev. Sci. Instrum.* **61,** 802–808 (1990).

130. Haeger, T., Wilmes, M., Heiderhoff, R. & Riedl, T. Simultaneous Mapping of Thermal Conductivity, Thermal Diffusivity, and Volumetric Heat Capacity of Halide Perovskite Thin Films: A Novel Nanoscopic Thermal Measurement Technique. *J. Phys. Chem. Lett.* **10,** 3019–3023 (2019).

131. Sood, A. *et al.* Direct Visualization of Thermal Conductivity Suppression Due to Enhanced Phonon Scattering Near Individual Grain Boundaries. *Nano Lett.* **18,** 3466–3472 (2018).

132. Sood, A. *et al.* An electrochemical thermal transistor. *Nat. Commun.* **9** (2018).

133. Olson, D. H. *et al.* Anisotropic thermal conductivity tensor of β-Y2Si2O7 for orientational control of heat flow on micrometer scales. *Acta Mater.* **189,** 299–305 (2020).

134. Olson, D. H. *et al.* Local thermal conductivity measurements to determine the fraction of alpha-cristobalite in thermally grown oxides for aerospace applications. *Scr. Mater.* **177,** 214–217 (2020).

135. Huxtable, S., Cahill, D. G., Fauconnier, V., White, J. O. & Zhao, J. C. Thermal conductivity imaging at micrometre-scale resolution for combinatorial studies of materials. *Nat. Mater.* **3,** 298–301 (2004).

136. Holland, S. D. & Reusser, R. S. Material Evaluation by Infrared Thermography. *Annu. Rev. Mater. Res.* **46,** 287–303 (2016).

137. Ahmadi, S., Burgholzer, P., Jung, P., Caire, G. & Ziegler, M. Super resolution laser line scanning thermography. *Opt. Lasers Eng.* **134** (2020).

138. Ahmadi, S. *et al.* Photothermal super resolution imaging: A comparison of different thermographic reconstruction techniques. *NDT E Int.* **111** (2020).

139. Graciani, G. & Amblard, F. Super-resolution provided by the arbitrarily strong superlinearity of the blackbody radiation. *Nat. Commun.* **10** (2019).

140. Parker, W. J., Jenkins, R. J., Butler, C. P. & Abbott, G. L. Flash method of determining thermal diffusivity, heat capacity, and thermal conductivity. *J. Appl. Phys.* **32,** 1679–1684 (1961).

141. Bisson, J. F., Fournier, D., Poulain, M., Lavigne, O. & Mévrel, R. Thermal conductivity of yttria-zirconia single crystals, determined with spatially resolved infrared thermography. *J. Am. Ceram. Soc.* **83,** 1993–1998 (2000).

142. Cernuschi, F., Russo, A., Lorenzoni, L. & Figari, A. In-plane thermal diffusivity evaluation by infrared thermography. *Rev. Sci. Instrum.* **72,** 3988–3995 (2001).

143. Pech-May, N. W., Mendioroz, A. & Salazar, A. Simultaneous measurement of the in-plane and in-depth thermal diffusivity of solids using pulsed infrared thermography with focused illumination. *NDT E Int.* **77,** 28–34 (2016).

144. COMSOL Multiphysics, www.comsol.com. COMSOL AB, Stockholm, Sweden.

145. International Commission on Illumination. *CIE 15: Colorimetry, 3rd edition* tech. rep. (2004).

146. Hunter, J. D. Matplotlib: A 2D graphics environment. *Comput. Sci. Eng.* **9,** 90–95 (2007).

147. Van der Vegt, A. *Vraagstukken polymeren, behorend by Polymeren, van keten tot kunststof* (Delft University Press, 1999).

148. Mark, J. E. *Physical Properties of Polymers Handbook* (Springer, 2007).

149. Pech-May, N. W. *et al.* Study of the thermal properties of polyester composites loaded with oriented carbon nanofibers using the front-face flash method. *Polym. Test.* **50,** 255–261 (2016).

150. Di Martino, D. *et al.* A multidisciplinary non-destructive study of historical pipe organ fragments. *Mater. Charact.* **148,** 317–322 (2019).

151. Bovelacci, A., Ciliberto, E., Greco, E. & Viscuso, E. Surface and Bulk Investigations of Organ Metal Pipe Degradation. *Procedia Chem.* **8,** 130–138 (2013).

152. Chiavari, C., Martini, C., Poli, G. & Prandstraller, D. Deterioration of tin-rich organ pipes. *J. Mater. Sci.* **41,** 1819–1826 (2006).

153. Nogita, K. *et al.* XRD study of the kinetics of beta to alpha transformations in tin. *Philos. Mag.* **93,** 3627–3647 (2013).

154. Craig, J. R. & Vaughan, D. J. *Ore microscopy and ore petrography* 434 (Wiley, 1994).

155. Miller, S. A. *et al.* SnO as a potential oxide thermoelectric candidate. *J. Mater. Chem. C* **5,** 8854–8861 (2017).

156. O'Brien, C. M. *et al.* Focal dynamic thermal imaging for label-free high-resolution characterization of materials and tissue heterogeneity. *Sci. Rep.* **10** (2020).

157. Zeynali, A. *et al.* Multiphoton Fabrication of Proteinaceous Nanocomposite Microstructures with Photothermal Activity in the Infrared. *Adv. Opt. Mater.* **8** (2020).

158. Zeynali, A. *et al.* Multiphoton fabrication of flexible photo-thermally active proteinaceous microstructures. *Chem. Eng. Trans.* **84,** 235–240 (2021).

159. Bouzin, M. *et al.* Multiphoton laser fabrication of hybrid photo-activable biomaterials. *Sensors* **21** (2021).

160. Nava, M. M. *et al.* Two-photon polymerized "nichoid" substrates maintain function of pluripotent stem cells when expanded under feeder-free conditions. *Stem Cell Res. Ther.* **7,** 1–12 (2016).

161. Zandrini, T. *et al.* Multi-foci laser microfabrication of 3D polymeric scaffolds for stem cell expansion in regenerative medicine. *Sci. Rep.* **9,** 1–9 (2019).

162. Sanchez, C., Belleville, P., Popall, M. & Nicole, L. Applications of advanced hybrid organic-inorganic nanomaterials: From laboratory to market. *Chem. Soc. Rev.* **40,** 696–753 (2011).

163. Aliofkhazraei, M. *Handbook of nanoparticles* 1–1426 (Springer International Publishing, 2015).

164. Wei, G. & Ma, P. X. Nanostructured biomaterials for regeneration. *Adv. Funct. Mater.* **18,** 3568–3582 (2008).

165. Yagci, Y., Jockusch, S. & Turro, N. J. Photoinitiated polymerization: Advances, challenges, and opportunities. *Macromolecules* **43,** 6245–6260 (2010).

166. Chen, M., Zhong, M. & Johnson, J. A. Light-Controlled Radical Polymerization: Mechanisms, Methods, and Applications. *Chem. Rev.* **116,** 10167–10211 (2016).

167. Maruo, S. & Fourkas, J. Recent progress in multiphoton microfabrication. *Laser Photon. Rev.* **2,** 100–111 (2008).

168. Maruo, S. & Kawata, S. Two-photon-absorbed near-infrared photopolymerization for three-dimensional microfabrication. *J. Microelectromechanical Syst.* **7,** 411–415 (1998).

169. Rocheva, V. V. *et al.* High-resolution 3D photopolymerization assisted by upconversion nanoparticles for rapid prototyping applications. *Sci. Rep.* **8** (2018).

170. Serbin, J. *et al.* Femtosecond laser-induced two-photon polymerization of inorganic-organic hybrid materials for applications in photonics. *Opt. Lett.* **28,** 301 (2003).

171. Serien, D., Kawano, H., Miyawaki, A., Midorikawa, K. & Sugioka, K. Femtosecond laser directwrite integration of multi-protein patterns and 3D microstructures into 3D glass microfluidic devices. *Appl. Sci.* **8,** 147 (2018).

172. Kaehr, B. & Shear, J. B. Multiphoton fabrication of chemically responsive protein hydrogels for microactuation. *Proc. Natl. Acad. Sci. U. S. A.* **105,** 8850–8854 (2008).

173. Kaiser, W. & Garrett, C. G. Two-photon excitation in CaF2: Eu2+. *Phys. Rev. Lett.* **7,** 229–231 (1961).

174. Pao, Y. H. & Rentzepis, P. M. Laser-induced production of free radicals in organic compounds. *Appl. Phys. Lett.* **6,** 93–95 (1965).

175. Helmchen, F. & Denk, W. Deep tissue two-photon microscopy. *Nat. Methods* **2,** 932–940 (2005).

176. Chen, L., Yan, C. & Zheng, Z. Functional polymer surfaces for controlling cell behaviors. *Mater. Today* **21,** 38–59 (2018).

177. Riahinasab, S. T. *et al.* Nanoparticle-based hollow microstructures formed by two-stage nematic nucleation and phase separation. *Nat. Commun.* **10,** 894–894 (2019).

178. Sironi, L. *et al.* Gold branched nanoparticles for cellular treatments. *J. Phys. Chem. C* **116,** 18407–18418 (2012).

179. A.B. Dahlin. *Plasmonic Biosensors : an Integrated View of Refractometric Detection.* (IOS Press, 2012).

180. Huang, X., Neretina, S. & El-Sayed, M. A. Gold Nanorods: From Synthesis and Properties to Biological and Biomedical Applications. *Adv. Mater.* **21,** 4880–4910 (2009).

181. Shukla, S. *et al.* Fabrication and characterization of gold-polymer nanocomposite plasmonic nanoarrays in a porous alumina template. *ACS Nano* **4,** 2249–2255 (2010).

182. Zhang, G. *et al.* Novel piezoelectric paper-based flexible nanogenerators composed of BaTiO3 nanoparticles and bacterial cellulose. *Adv. Sci.* **3** (2015).

183. Pallavicini, P. *et al.* Modular approach for bimodal antibacterial surfaces combining photo-switchable activity and sustained biocidal release. *Sci. Rep.* **7,** 1–10 (2017).

184. Pallavicini, P. *et al.* Triton X-100 for three-plasmon gold nanostars with two photothermally active NIR (near IR) and SWIR (short-wavelength IR) channels. *Chem. Commun.* **49,** 6265–6267 (2013).

185. Paviolo, C. & Stoddart, P. R. *Gold nanoparticles for modulating neuronal behavior* 2017.

186. Hayes, B. S., Govyadinov, A. N. & Kornilovitch, P. E. Microfluidic switchboards with integrated inertial pumps. *Microfluid. Nanofluidics* **22** (2018).

187. Seo, H. I. *et al.* Thermo-responsive polymeric nanoparticles for enhancing neuronal differentiation of human induced pluripotent stem cells. *Nanomedicine Nanotechnology, Biol. Med.* **11,** 1861–1869 (2015).

188. Akhtar, R., Sherratt, M. J., Cruickshank, J. K. & Derby, B. Characterizing the elastic properties of tissues. *Mater. Today* **14,** 96–105 (2011).

189. De Loubens, C. *et al.* Mechanical characterization of cross-linked serum albumin microcapsules. *Soft Matter* **10,** 4561–4568 (2014).